Calhoun: The NPS Institutional Archive
DSpace Repository

Theses and Dissertations | Thesis and Dissertation Collection

1986

Underwater acoustic scatter from a model of the Arctic ice canopy

Denny, Patrick L

http://hdl.handle.net/10945/22164

Downloaded from NPS Archive: Calhoun

Calhoun is a project of the Dudley Knox Library at NPS, furthering the precepts and goals of open government and government transparency. All information contained herein has been approved for release by the NPS Public Affairs Officer.

Dudley Knox Library / Naval Postgraduate School
411 Dyer Road / 1 University Circle
Monterey, California USA 93943

http://www.nps.edu/library

NAVAL POSTGRADUATE SCHOOL
Monterey, California

THESIS

UNDERWATER ACOUSTIC SCATTER FROM
A MODEL OF THE ARCTIC ICE CANOPY

by

Patrick L. Denny

and

Kevin R. Johnson

December 1986

Thesis Advisor: H. Medwin

Approved for public release; distribution unlimited

T230329

SECURITY CLASSIFICATION OF THIS PAGE

REPORT DOCUMENTATION PAGE

1a REPORT SECURITY CLASSIFICATION UNCLASSIFIED	1b RESTRICTIVE MARKINGS
2a SECURITY CLASSIFICATION AUTHORITY	3 DISTRIBUTION/AVAILABILITY OF REPORT Approved for public release; distribution inlimited
2b DECLASSIFICATION/DOWNGRADING SCHEDULE	
4 PERFORMING ORGANIZATION REPORT NUMBER(S)	5 MONITORING ORGANIZATION REPORT NUMBER(S)
6a NAME OF PERFORMING ORGANIZATION Naval Postgraduate School 6b OFFICE SYMBOL (If applicable) 61	7a NAME OF MONITORING ORGANIZATION Naval Postgraduate School
6c ADDRESS (City, State, and ZIP Code) Monterey, California 93943-5000	7b ADDRESS (City, State, and ZIP Code) Monterey, California 93943-5000
8a NAME OF FUNDING/SPONSORING ORGANIZATION 8b OFFICE SYMBOL (If applicable)	9 PROCUREMENT INSTRUMENT IDENTIFICATION NUMBER
8c ADDRESS (City, State, and ZIP Code)	10 SOURCE OF FUNDING NUMBERS PROGRAM ELEMENT NO / PROJECT NO / TASK NO / WORK UNIT ACCESSION NO

11 TITLE (Include Security Classification)
UNDERWATER ACOUSTIC SCATTER FROM A MODEL OF THE ARCTIC ICE CANOPY

12 PERSONAL AUTHOR(S)
Denny, Patrick L., and Johnson, Kevin R.

13a TYPE OF REPORT	13b TIME COVERED	14 DATE OF REPORT (Year, Month, Day)	15 PAGE COUNT
Masters Thesis	FROM ____ TO ____	1986 December	131

16 SUPPLEMENTARY NOTATION

17 COSATI CODES			18 SUBJECT TERMS (Continue on reverse if necessary and identify by block number)
FIELD	GROUP	SUB-GROUP	Underwater Acoustics, Scatter, Backscatter, Arctic Ice, Reflection Coefficient, Flexural Waves

19 ABSTRACT (Continue on reverse if necessary and identify by block number)

When low frequency underwater sound interacts with the Arctic ice cover, not only will it be reflected from the plane and scattered in all directions from roughness elements, but it will also be diffracted at leads and reradiated from flexural waves in the ice. These phenomena have been studied in an anechoic tank by pulse transmission from an underwater point source to a series of large floating acrylic plate models, each representing a different type of ice cover. The flexural wave speed, the plate and lead dimensions and the acoustic roughness are accurately scaled, and the specific acoustic impedance contrast is approximately modeled by the selection of the acrylic material. The physical contributors to the gross reflection coefficient and backscattering strength are identified and compared for models of

20 DISTRIBUTION/AVAILABILITY OF ABSTRACT ☒ UNCLASSIFIED/UNLIMITED ☐ SAME AS RPT ☐ DTIC USERS	21 ABSTRACT SECURITY CLASSIFICATION UNCLASSIFIED
22a NAME OF RESPONSIBLE INDIVIDUAL Herman Medwin	22b TELEPHONE (Include Area Code) 408-646-2385 22c OFFICE SYMBOL 61Md

DD FORM 1473, 84 MAR 83 APR edition may be used until exhausted
All other editions are obsolete

SECURITY CLASSIFICATION OF THIS PAGE

Item #19 - Cont'd

a plane ice layer, an Arctic ice pressure ridge, edges of leads, and a rubble field of ice.

Approved for public release; distribution unlimited

Underwater Acoustic Scatter from a Model of the Arctic Ice Canopy

by

Patrick Leo Denny
Lieutenant Commander, United States Navy
B.S., United States Naval Academy, 1973

and

Kevin Robert Johnson
Lieutenant, United States Navy
B.S., University of California, Riverside, 1976

Submitted in partial fulfillment of the
requirements for the degree of

MASTER OF SCIENCE IN ENGINEERING ACOUSTICS

ABSTRACT

When low frequency underwater sound interacts with the Arctic ice cover, not only will it be reflected from the plane and scattered in all directions from roughness elements, but it will also be diffracted at leads and reradiated from flexural waves in the ice. These phenomena have been studied in an anechoic tank by pulse transmission from an underwater point source to a series of large floating acrylic plate models, each representing a different type of ice cover. The flexural wave speed, the plate and lead dimensions and the acoustic roughness are accurately scaled, and the specific acoustic impedance contrast is approximately modeled by the selection of the acrylic material. The physical contributors to the gross reflection coefficient and backscattering strength are identified and compared for models of a plane ice layer, an Arctic ice pressure ridge, edges of leads, and a rubble field of ice.

TABLE OF CONTENTS

I. INTRODUCTION 12

A. PROPAGATION OF SOUND IN THE ARCTIC 12

B. DESCRIPTION OF THE ARCTIC ICE COVER 12

II. RESEARCH FACILITIES AND EQUIPMENT 19

A. OCEAN PHYSICS LABORATORY AND ANECHOIC TANK 19

B. TRANSMIT AND RECEIVE SYSTEMS 21

C. SIGNAL PROCESSING EQUIPMENT 22

III. DESCRIPTION OF PHYSICAL MODELS 26

A. MODELS OF SMOOTH ICE AND ARCTIC OPEN LEADS 31

B. MODEL OF A PRESSURE RIDGE 33

C. MODEL OF A RUBBLE FIELD 33

IV. THEORY 39

A. DIFFRACTION 39

B. ROUGH SURFACE FORWARD SCATTER FROM A RUBBLE FIELD 46

C. REFLECTION FROM A SMOOTH PLATE 49

D. FLEXURAL WAVES IN SMOOTH PLATES 50

V. SPECULAR SCATTER 58

A. EXPERIMENTAL PROCEDURE 58

B. RESULTS AND DISCUSSION 61

VI. BACKSCATTER 80

A. PROCEDURE 80

B. RESULTS OF BACKSCATTER MEASUREMENTS 82

C. SUMMARY 113

VII. SMOOTH PLATE FLEXURAL WAVES 116

A. PROCEDURE FOR THE MEASUREMENT OF THE SMOOTH PLATE FLEXURAL WAVE 116

B. FLEXURAL WAVE MEASUREMENT RESULTS 119

VIII. CONCLUSIONS 125

LIST OF REFERENCES 127

INITIAL DISTRIBUTION LIST 130

LIST OF TABLES

I EQUIPMENT LIST 24

II COMPARISON OF THE PHYSICAL PROPERTIES OF ARCTIC ICE TO THE ACRYLIC MODEL LABORATORY CONDITIONS 27

III SMOOTH PLATE REFLECTION COEFFICIENT 63

IV PRESSURE RATIOS 70

V WEDGE FORWARD SCATTER DATA 74

VI BACKSCATTER FROM THE ACRYLIC RUBBLE FIELD 108

LIST OF FIGURES

1.1 A typical sound velocity profile and associated ray diagram for underwater sound propagation in the Arctic (Diachok, 1974) 13

1.2 Scattering of low frequency sound from the Arctic ice canopy 14

2.1 Schematic diagram of the signal processing flow path 20

2.2 Time domain voltage response to an input sinusoidal pulse, driven at 7.07 volts RMS. Sinusoid frequency is 56 kHz 25

3.1 Cross section of the pressure ridge model used to measure forward and back scatter from a ridge keel 34

3.2 Bottom roughness profile of the acrylic "rubble" model 37

3.3 Height histogram of the bottom surface of the roughened acrylic plate that was manufactured to model an Arctic rubble field 38

3.4 Slope histogram of the bottom surface of a roughened acrylic plate used to model an Arctic rubble field 38

4.1 (a) Wedge geometry for Equations 4-1 thru 4-3. (b) Unfolded geometry 41

4.2 (a) Diagram showing the three Biot-Tolstoy wedges that make up the model of the ridge keel. (b) Time domain impulse response calculated using Biot-Tolstoy theory and superposition 43

4.3 Theoretical flexural wave phase and group speeds as a function of frequency 53

5.1 Smooth acrylic plate reflection coefficient, 30.3 kHz 64

5.2 Smooth acrylic plate reflection coefficient, 50.8 kHz 65

5.3 Smooth acrylic plate reflection coefficient, 74.2 kHz. 66

5.4 Specular scatter at model of water-rubble ice bottom interface. 69

5.5 Temporal and spectral forward scatter from the laboratory wedge. Grazing angle is 33 degrees. 75

5.6 Temporal and spectral forward scatter from the laboratory wedge. Grazing angle is 45 degrees. 76

5.7 Temporal and spectral forward scatter from the laboratory wedge. Grazing angle is 63 degrees. 77

6.1 Location of source and receiver with rspect to the acrylic plate and scattering surface for the backscatter measurements. 81

6.2 Time domain signal response for backscattering off the lagging edge of an acrylic plate. 83

6.3 Geometry used in determining geometric divergence from a linear scattering element. 85

6.4 Results of the measurements using the geometry shown in Figure 6.3, where the range is r. 87

6.5 Temporal and spectral backscatter from the leading edge of the acrylic plate. Grazing angle is 30°. 89

6.6 Temporal and spectral backscatter from the leading edge of the acrylic plate. Grazing angle is 45°. 90

6.7 Temporal and spectral backscatter from the leading edge of the acrylic plate. Grazing angle is 60°. 91

6.8 Temporal and spectral backscatter from a lagging edge of the acrylic plate. 94

6.9 Temporal and spectral backscatter from an open lead with width 2 cm (12 m in the arctic). Grazing angle is 15°. 96

6.10 Spectral backscatter from an open lead with width 1 cm (6 m in the Arctic). Grazing angle is 15°. . 97

6.11 Spectral backscatter from an open lead with width 3 cm (18 m in the Arctic). Grazing angle is 15° 98

6.12 Temporal and spectral backscatter from an open lead with width 2 cm (12 m in the Arctic). Grazing angle is 41° 99

6.13 Spectral backscatter from an open lead with width 1 cm (6 m in the Arctic). Grazing angle is 41° 100

6.14 Spectral backscatter from an open lead with width 3 cm (18 m in the Arctic). Grazing angle is 41° 101

6.15 Temporal and spectral backscatter from the model of the ridge keel. The grazing angle is 15° 103

6.16 Temporal and spectral backscatter from the model of the ridge keel. The grazing angle is 29° 104

6.17 Temporal and spectral backscatter from the model of the ridge keel. The grazing angle is 47° 105

6.18 Temporal and spectral backscatter from the model of the ridge keel. The grazing angle is 63° 106

6.19 Comparison of the measured BSS from the acrylic models of the open lead and ridge keel at shallow and moderate grazing angles 110

6.20 Backscattering strength as a function of grazing angle for the acrylic model of a rubble field compared with actual Arctic backscatter from rough ice 112

6.21 Composite BSS computed for the acrylic model of the Arctic ice scaled to Arctic frequencies plotted along with Arctic measurements of BSS 114

7.1 Flexural wave phase speed as a function of frequency for a 3 mm thick smooth acrylic plate 120

7.2 Theoretical flexural phase speed for an infinite flat plate of 1.5 m thickness 122

7.3 Measured boundary wave pressure of the direct water wave plotted as a function of the ratio of the depth of the receiver below the plate to the wavelength of the waterborne compressional wave 123

ACKNOWLEDGEMENT

The writers wish to express their appreciation to Professor Herman Medwin of the Physics Department, U. S. Naval Postgraduate School for his guidance and encouragement during the preparation of this thesis; to Professor Robert H. Bourke, Dr. Steven Ackley, and Dr. John Walsh for sharing their knowledge of the Arctic; to Ken Reitzel and Lt. Michael Browne for their assistance in the laboratory; and to our wives Linda and Mary for their love and understanding.

The financial support provided this research by the Office of Naval Research is acknowledged.

I. INTRODUCTION

A. PROPAGATION OF SOUND IN THE ARCTIC

In Arctic waters the existence of a positive sound speed gradient in the water column which includes a strongly positive near-surface portion which causes a shallow sound duct to be formed, forces sound energy to be repeatedly refracted upwards to the ice surface. Figure 1.1 illustrates a typical ray diagram for sound transmission in the Arctic. Long-range propagation measurements in the Arctic Ocean show that the low-frequency attenuation and backscattering strengths are more than an order of magnitude greater than in the open ocean (Mellen, 1986). In order to predict the range at which a noise source may be detected in the ice-covered Arctic, it is first necessary to understand what happens to the incident sound when it interacts with the highly variable ice cover. To do this requires a basic understanding of the acoustical characteristics of the ice cover.

B. DESCRIPTION OF THE ARCTIC ICE COVER

In general, the Arctic ice surface is variable in thickness, density, elastic constants and shape. As illustrated in Figure 1.2, the sea ice can be partitioned into the following acoustically significant categories: level ice (70 %), pressure ridges and

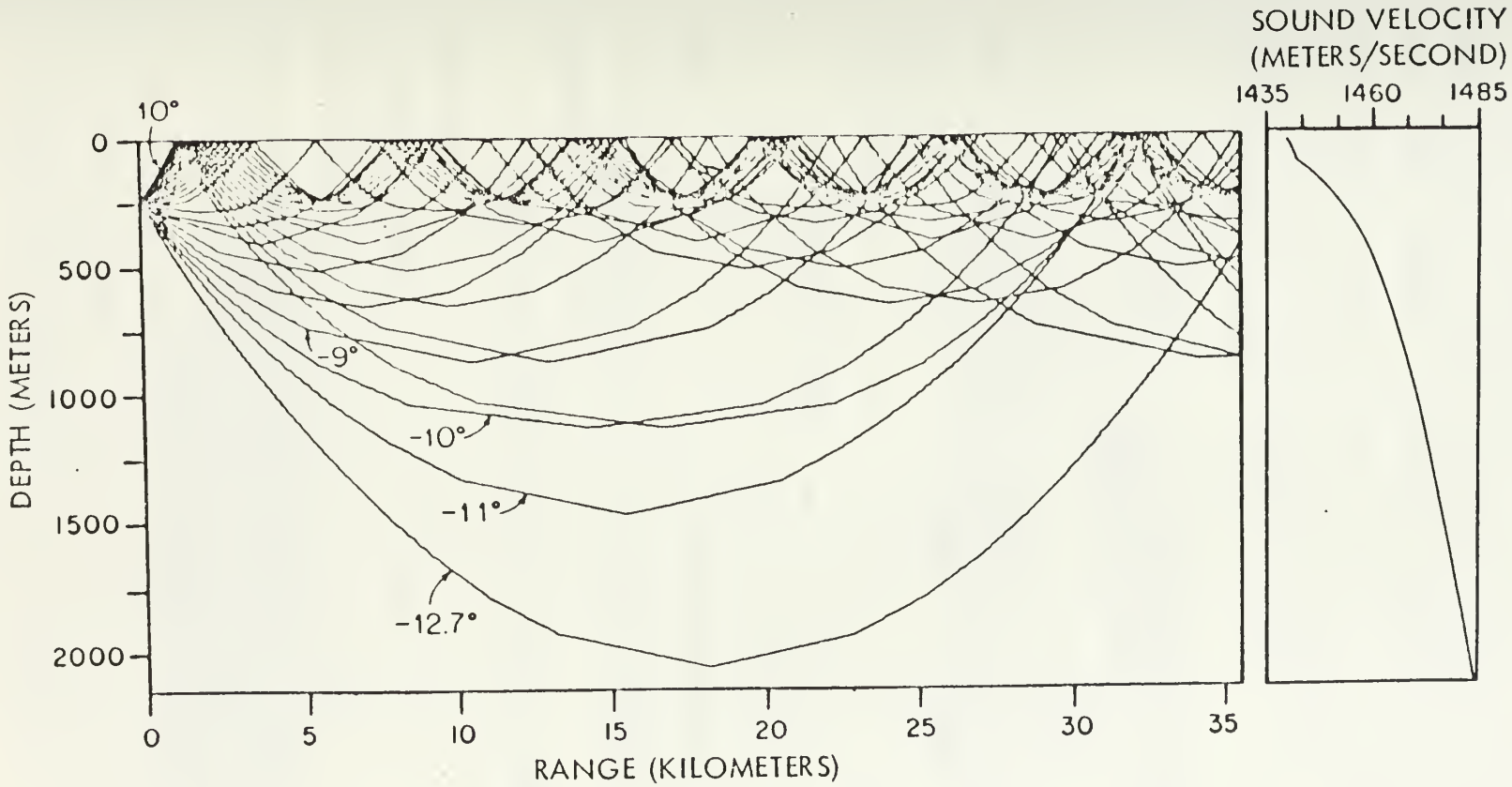

Figure 1.1. A typical sound velocity profile and associated ray diagram for underwater sound propagation in the Arctic (Diachok, 1974).

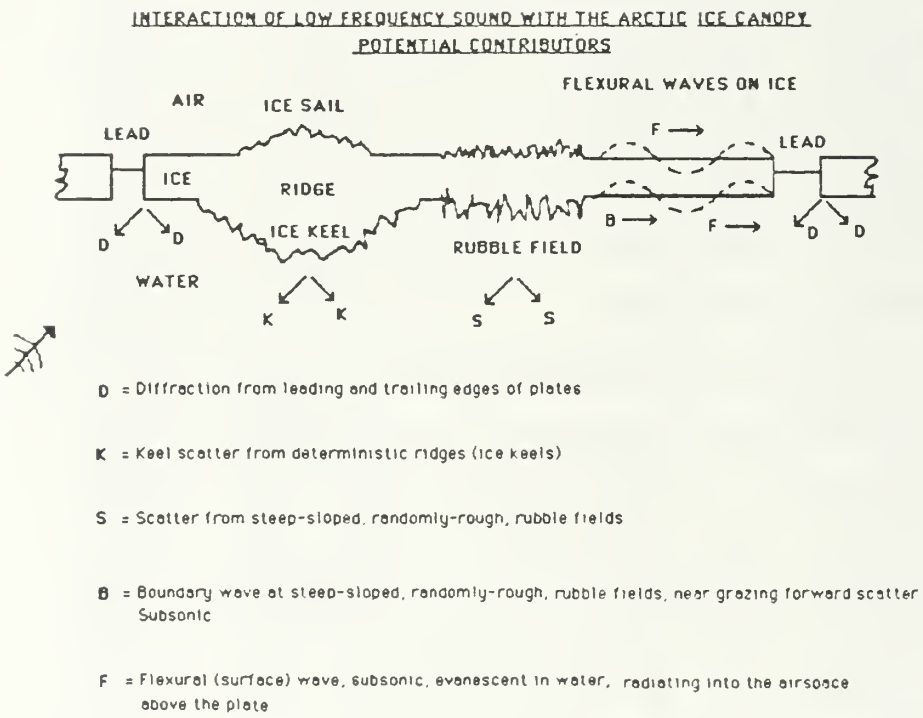

Figure 1.2. Scattering of low frequency sound from the Arctic ice canopy. Acoustically significant features of the ice canopy include level ice, pressure ridge keels, hummock fields and edges of leads and polynyas.

rubble fields (25 %), and leads (5 %). The number in parentheses is the approximate percentage of the Arctic ice cover each category represents (Weeks et al, 1971). This experiment is concerned only with $kh < 1$, where h is the ice thickness and k is the horizontal wavenumber. Each of these ice categories is briefly described below.

1. Level Ice

Sea ice is termed level if its surface changes less than 1 part in 40 (Wadhams et al, 1985, p.1072). The thickness of level ice depends on the age of the ice, with first year ice generally less that 2 m thick and multi-year ice having a mean ice thickness of 2.5 to 3 m (Ackley et al., 1976, p. 9).

2. Pressure Ridges

Ridges are formed by the interaction of adjacent ice floes. The type and size of a ridge is a function of the thickness of the interacting ice and the degree of compressive or shear forces being exerted on the ice floes.

Hibler et al (1972) compiled above-ice data from visual and laser profilometry and underice data from submarine underice profiles to develop statistical models of pressure ridge keel depths and the spacings between ridges. To insure that only pressure ridges are dealt with in the above ice and underice profiles, a cutoff height (or depth) was used, i.e., ridge height and keel depth distribution data are reported from a set that includes all ridges greater than a given cutoff. The average pressure ridge keel depth reported by Hibler et al

(1972) from the set of all ridges greater than 6.1 m, was 9.6 m in the Central Arctic and 11.4 m in the Canadian Archipeligo. They further report that the ratio of sail height to keel depth is on the order of 1:5. They report the average spatial distribution of pressure ridges as 4.3 ridges/km in the Central Arctic and 9.6 ridges/km in the Canadian Archipeligo.

Hibler et al (1974) reported that ridging intensity is seasonally dependent. They determined that the spatial distribution of ridges in the Beaufort and Chukchi Sea regions was 1.83 ± 0.6 ridges/km in March, and 0.99 ± 0.61 ridges/km in October and November. Furthermore, they observed that all the ridges investigated had similar slope angles, such that the ratio of the base width to the ridge height was approximately four.

A specific multi-year pressure ridge was the object of investigation by Kovacs et al (1973). This particular ridge had a sail height of 4 m and a keel depth of 13 m. The multi-year pressure ridge differs from the first year pressure ridge in that the latter is poorly bonded and contains many spaces between the blocks of ice that comprise the ridge. In a multi-year ridge these voids eventually are filled with ice due to the seasonal melting and re-freezing of the ice.

Wright et al (1978) report values for the keel depth to sail height ratio and keel width to keel depth ratios slightly different from those above, i.e., 3.2:1 for keel to sail ratio and 3.3:1 for the width to keel depth ratio. They also report that

keel depth statistics show little or no seasonal variability probably due to the fact that the underice surface does not feel the effects of the ablation of the ice surface during the warming months.

In the present model the ice ridge is assumed to be a triangular cross sectional (prismatic) wedge below the plate and a similar smaller prism above the plate. The fine structure is omitted in this low frequency model.

3. Hummock Fields

In areas of severe shear forces ridges can be pushed together to form a series of adjacent ridges which would appear from above like a farmer's plowed field (Hibler and Ackley, 1975). This type of non-random rubble field occurs where the forces acting on the ice are directional such as in a narrow strait or butted against a land mass. In another situation where the forces are less constrictive, such as in the Central Arctic Basin the ridges could be pushed together to form a nearly random field of jumbled blocks interspersed with large, nearly vertical ridge segments. It is this latter description which was modelled for this experiment.

4. Leads and Polynas

An open lead or polynya in the ice cover is an area where there is no ice. A covered lead exists where the thickness of the ice is much less than the that of the surrounding ice floes, i.e., below 1 m thickness (Wadhams and Horne,1980). Leads are generally considered to

be cracks in the ice where the length of the crack is much greater than the width. Polynyas on the other hand are large open areas up to several kilometers wide. For this experiment, open leads of 6, 12 and 18 m width have been modeled. A single edge of an open polynya has been modeled by using a single plate edge. Chapter III describes these models in greater detail.

II. RESEARCH FACILITIES AND EQUIPMENT

A. OCEAN PHYSICS LABORATORY AND ANECHOIC TANK

The anechoic tank provided a low noise environment sufficient to conduct this experiment. The dimensions of the anechoic tank are: length - 7.3 m, width - 1.8 m, depth - 2.2 m. Aluminum-impregnated rubber conical sound absorbers line each wall. Pulsed signals were transmitted and the signal return was identified, isolated and analyzed utilizing a judicious choice of a sampling window at the signal processing end. Figure 2.1 illustrates the equipment set-up utilized throughout the experiment. An equipment list is provided in Table I. All equipment used is available on the commercial market with one exception - the Random Surface Measuring Device (RSM). This device, which was designed by a former NPS student LT. S. Kasputis (1984), allows the accumulation of a large data base for statistics on a given surface. It can determine heights on slopes of less than 70 degrees with a precision of 20 μm. Additional equipments which merit a more detailed description are discussed below.

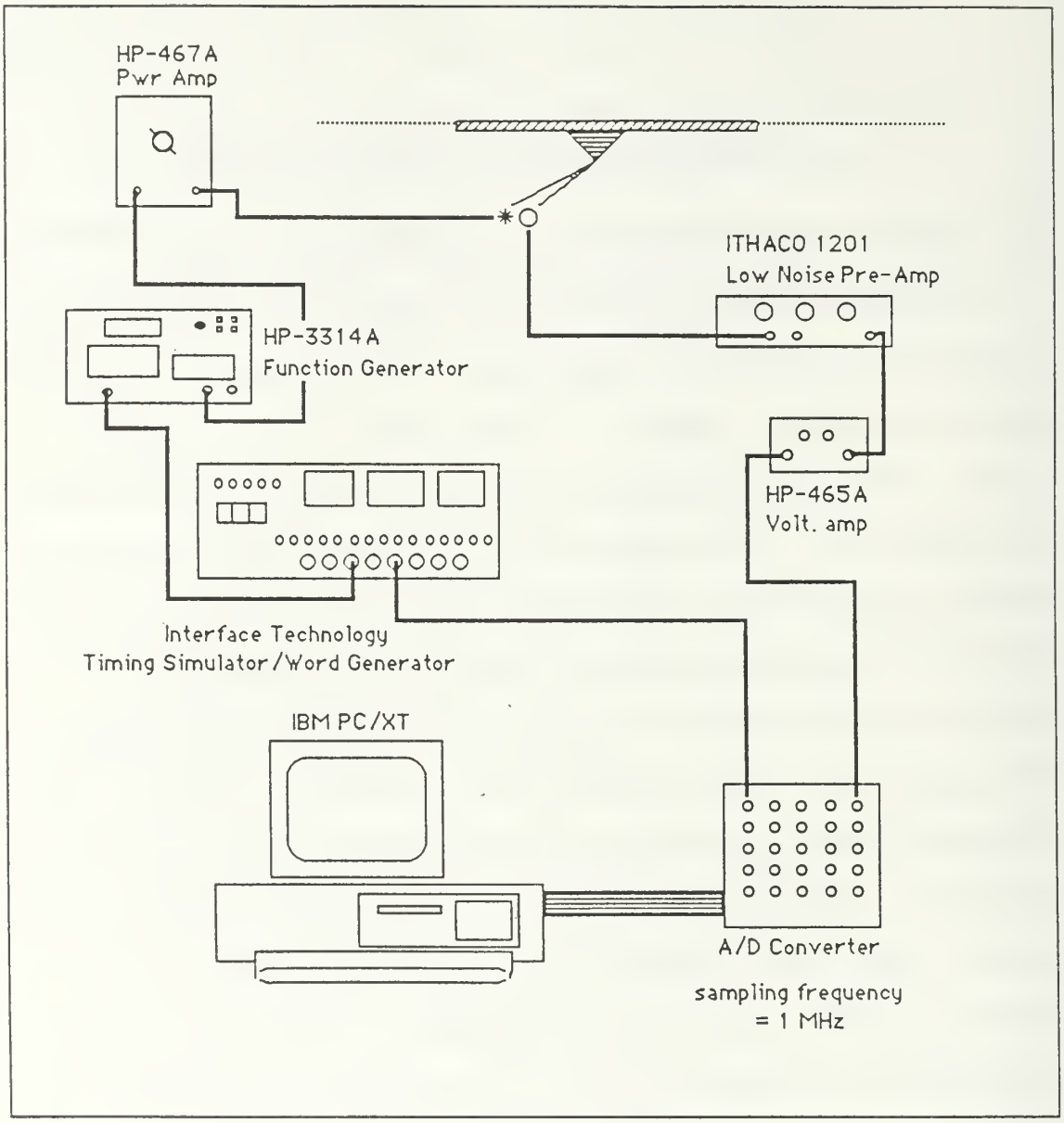

Figure 2.1: Schematic diagram of the signal processing flow path.

B. TRANSMIT AND RECEIVE SYSTEMS

1. Hewlett Packard Function Generator, Model 3314A

The 3314A Function Generator is a digital, multi-mode, programmable function generator which features preset Sine, Triangle and Squarewave functions and programmable arbitrary waveforms from 1mHz to 19.999MHz and a maximum output voltage of 10 volts peak-to-peak. The function generator was utilized in the N CYCLE MODE which outputs a burst of N complete cycles, starting when an internal or external trigger edge is received. The excellent stability of the function generator permitted repeated data runs in minimal time.

2. Nicolet FFT Wave Analyzer , Model 660B

The Nicolet wave analyzer is programmable and performs its own analog to digital conversion. The sampling rate is limited to 250,000 samples per second. It has a built-in CRT screen that allows real time observation of either the received time signal or its frequency spectrum. This equipment was utilized in parallel to the signal processing equipment to permit initial detection of the signal of interest.

3. Interface Technology Timing Simulator, Model RS-648

The timing simulator was used to trigger the function generator, the Nicolet and the signal processing equipment. It has a 50 nanosecond timing resolution.

4. Celesco LC-10 Hydrophone

LC-10 hydrophones were used as both transmitter and receiver. The specifications for the experiment required a point source (ka « 1, where 'k' is the wave number and 'a' is the linear dimension of the transducer) and receiver with rise and decay times sufficiently short to permit the reception of undistorted pulsed signals in an environment where the time window was critical. The time duration of the pulse is important since all of the desired signal must be sampled in a time window free of the unwanted arrivals from the tank or plate reflections and diffractions from the edges of the model. Additional requirements were a relatively high and flat free-field voltage sensitivity and an omnidirectional directivity pattern in the frequency range of 30 kHz to 100 kHz. The LC-10's directivity pattern was omni-directional to within ± 2 dB. The greatest disadvantage of the LC-10 as a source is its low output power, however, the combination of short ranges (less that 2 m) and the low ambient noise level in the anechoic tank permitted its use with excellent results.

C. SIGNAL PROCESSING EQUIPMENT

Signal processing was accomplished using an IBM PC/XT personal computer fitted with a Computerscope Model ISC-16 Signal Processing system. The Computerscope ISC-16 system is a fully integrated hardware and software package designed to permit the IBM to perform as a data acquisition and analysis

laboratory instrument. The ISC-16 package consists of a 16-channel analog to digital converter board, an external Instrument Interface and Scope Driver software. The package is capable of receiving 16 channels of data input at an aggregate sampling rate of up to 1MHz. Digital conversion is achieved with 12 bit accuracy over an input range of -10 to +10 volts. The Scope Driver software permits the IBM CRT to emulate a digital storage oscilloscope with numerous waveform manipulation and display modes, and to output high resolution graphics to a dot matrix printer or X/Y plotter. Figure 2.2 is a graphic produced by the Computerscope system and illustrates the systems excellent signal processing capabilities. The package is capable of directly accessing 640K of RAM.

TABLE I

EQUIPMENT LIST

Abbreviation	Nomenclature
Timing Simulator	Interface Technology Timing Simulator/Word Generator, Model RS-648
Function Generator	Hewlett Packard Function Generator, Model HP-3314A
Power Amplifier	Hewlett Packard Power Amplifier, Model HP-467A
Source or Receiver	Celesco LC-10 Hydrophone
Pre-Amplifier	Ithaco Low Noise Pre-Ampifier, Model 1201
Nicolet	Nicolet Dual Channel FFT Analyzer, Model 660B
Voltage Amplifier	Hewlett Packard Voltage Amplifier, Model HP-465A
Signal Processor	IBM PC/XT with Computerscope ISC-16 Data Acquisition and Analysis Package
Scope	Kikusui Oscilloscope, Model COS 5060

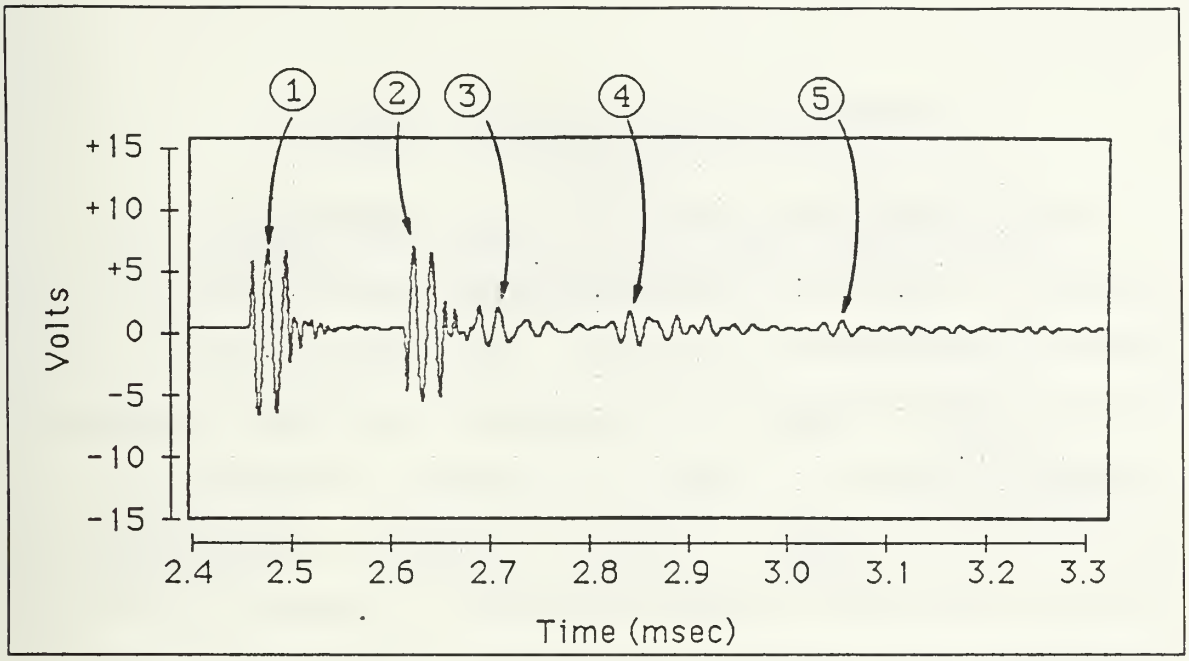

Figure 2.2:
Time domain voltage response to an input sinusoidal pulse, driven at 7.07 volts RMS. Sinusoid frequency is 56 kHz.

Input pulse: $y(t) = A \sin(2\pi f t)\,[1(t) - 1(t-2/f)]$

Peak Identification:

1 - Direct signal
2 - Surface reflected signal
3 - Specular scatter from sides of tank
4 - Diffraction from corner of water-air interface and side of tank
5 - Specular scatter from the bottom of tank.

III. DESCRIPTION OF PHYSICAL MODELS

Before construction of the "ice" models could begin, it was necessary to select the material which best approximated the physical characteristics of Arctic ice. The internal structure of sea ice, such as its saline content and the distribution of melt inclusions, is beyond the scope of our interest; furthermore for the low frequency regime which is our interest, average values provide a satisfactory acoustical description. Therefore, for this experiment it was necessary to emulate the bulk properties of the ice cover. Acrylic plate was chosen because it has several important physical properties that parallel closely those of Arctic sea ice. Specifically, the longitudinal wave speed and flexural wave speed (for scaled thicknesses), Poisson Ratio, and the characteristic impedance (ρc) for acrylic plates all fall well within the measured range for Arctic sea ice. The density of the acrylic plate is about 25% too high and the shear and compressional attenuations of the plates are somewhat higher as well. Table II summarizes the comparison between Arctic ice conditions and our laboratory acrylic "ice sheet" floating in a fresh water tank.

TABLE II
COMPARISON OF THE PHYSICAL PROPERTIES OF ARCTIC ICE TO THE ACRYLIC MODEL LABORATORY CONDITIONS

PROPERTIES	ARCTIC		LAB	MODEL/ICE RATIO
CHARACTERISTIC	RANGE	TYPICAL	MODEL	
1. YOUNG'S MOD E, (Pa x 10^9)	1.7-9.0 (1)	4.1 (2)	4.1 (3)	0.46-2.41
2. DENSITY ρ_2 (kg/m^3)	760-960 (4)	930 (4)	1148 (3)	1.20-1.51
3. POISSON'S RATIO	0.30-0.36 (5)	0.33 (5)	0.316 (3)	0.88-1.05
4. BULK COMPRES-SIONAL WAVE SPEED (m/s)	2800-3500 (6)	3150 (6)	2240 (3)	0.50 - 1.45
5. COMP. WAVE ATTENUATION (a) (dB /m), F(kHz)	0.3F-0.05F (20)	0.06F (20)	0.424F (3)	1.41 - 8.48
6. BULK SHEAR WAVE SPEED (m/s)	1500-1860 (6)	1700 (6)	1373 (3)	0.74 - 0.92
7. SHEAR WAVE ATTENUATION (σ) (dB/m), F(kHz)	1.8F-0.30F (20)	0.36F (20)	0.853F (3)	0.47 - 2.37

TABLE II (CONT'D)
COMPARISON OF THE PHYSICAL PROPERTIES OF ARCTIC ICE TO THE ACRYLIC MODEL LABORATORY CONDITIONS

8. BULK CHAR. IMP. $\rho_2 c_2$, $(kg/m^2\text{-}s) \times 10^6$	1.06-3.54 (8)	2.07 (9)	2.57 (10)	0.73-2.42
9. FLEXURAL WAVE SPEED (m/s)	252-2357 (11)	898-1270 (12)	700-1150 (3)	0.49-2.78
10. FLEXURAL WAVE ATTENUATION (dB/m), F(kHz)	Data not available		1.5F (3)	
11. PLATE THICKNESS h (m)	0.5-6.0 (4,7)	2.0 (7)	0.00318 (3)	1:600
12. THICK/WAVELENGTH h/λ	0.007-0.1 (14)	0.09 (15)	0.04-0.11 (16)	0.4-1.2
13. VEL. RATIO c_2/c_1 (ICE/WATER)	0.97-2.48 (17)	1.54 (18)	1.51 (19)	0.61-1.56

TABLE II (CONT'D)
COMPARISON OF THE PHYSICAL PROPERTIES OF
ARCTIC ICE TO THE ACRYLIC MODEL LABORATORY
CONDITIONS

WATER CHARACTERISTICS

14. TEMPERATURE T, °C	(-1.6) to (-1.8) (1)		20 (3)	
15. SOUND SPEED C_1, (m/s)	1440-1485 (22)	1440 (22)	1481 (3)	1.00-1.03
16. DENSITY ρ_1, (kg/m^3)	1000-1040 (21)	1026 (21)	1000 (3)	0.96-1.00
FREQUENCY RANGE OF INTEREST F, (KHz)	0.05-0.14		30-80	600:1

LIST OF REFERENCES FOR TABLE II (the complete reference for all of the below references is in the LIST OF REFERENCES).

1. Weeks, 1976.
2. Typical value.
3. Measured laboratory value. .
4. Ackley et al, CRREL Report 76-18, 1976.
5. Schwartz and Weeks, 1977.
6. Hunkins, 1960.
7. Wadhams et al, 1985.

TABLE II (CONT'D)
COMPARISON OF THE PHYSICAL PROPERTIES OF ARCTIC ICE TO THE ACRYLIC MODEL LABORATORY CONDITIONS

8. Calculated using: ρ_2 = 760 to 960 kg/m^3, and c_2 = 1395 to 3688 m/s.
9. Calculated using: ρ_2 = 930 kg/m^3 and c_2 = 2224 m/s.
10. Calculated using: ρ_2 = 1148 kg/m^3 and c_2 = 2240 m/s.
11. Calculated using: $v = (2\pi fh)^{1/2} B$ (m/s), where:
    h_{min} = 0.5 m, h_{max} = 6.0 m
    f_{min} = 50 Hz, f_{max} = 140 Hz
    B_{min} = 20.17, B_{max} = 32.44 where B is the flexural wave constant $(m/s)^{1/2}$.
12. Calculated using h = 2.0 m and B = 25.34 $(m/s)^{1/2}$.
13. Calculated using h = 3.18e-3 m and B = 23.98 $(m/s)^{1/2}$.
14. Calculated using h = 2.0 m and f = 50 to 140 Hz.
15. Calculated using h = 2.0 m and f = 95 Hz.
16. Calculated using h = 3.18e-3 m and f = 30 to 80 kHz.
17. Calculated using c_{min} = 1395, c_{max} = 3688 (m/s)
    c_{min} = 1440, c_{max} = 1485 (m/s).
18. Calculated using c = 1440, c = 2224 (m/s).
19. Calculated using c = 1481, c = 2240 (m/s).
20. McCammon and McDaniel, 1985.
21. Myers et al, 1969.
22. NAVOCEANO TECHNOTE, 1974.

A. MODELS OF SMOOTH ICE AND ARCTIC OPEN LEADS

Scaling of the parameters to be measured such as diffraction strength, coherent forward scattering and flexural wave propagation for a particular frequency and ice thickness range in the Arctic can be adequately achieved. This requires that the physical properties of the model be similar to those same properties in the Arctic. Once this is accomplished, what is required is that the scaling of the ratio of model length to laboratory wavelength be the same as Arctic conditions. As previously stated, the acoustically significant physical properties of Arctic ice are well matched in acrylic. Therefore, modeling of the arctic for several of the phenomena studied here requires that the ratio of the acoustic wave length (λ), and the ice thickness (h), be the same for the two situations. Medwin et al. (1984) successfully demonstrated the accuracy of this modelling technique. The frequency range of interest for sound propagation in the Arctic for this experiment is 50 to 150 Hz.

$$\lambda = \text{speed of sound} \Big/ \text{frequency}$$

$$[h/\lambda]_{ice} = [h/\lambda]_{acrylic}$$

$$f_{acrylic} = [h]_{acrylic} \Big/ [h/\lambda]_{ice}$$

Assuming a typical Arctic level ice thickness of about 2 m, then 1/8 in acrylic (3.125 mm) corresponds to a model scale of about 600:1.

Therefore,

when f_{ice} = 50 Hz, $f_{acrylic}$ = 30 kHz, and

when f_{ice} = 150 Hz, $f_{acrylic}$ = 90 kHz.

Since the density of acrylic is slightly greater than water it was necessary to devise some means of "floating" the plate in the tank without suppressing the generation of flexural modes in the plate. The solution to this problem was actually quite simple. A 1.27 cm high bead of silicon sealer laid around each edge of the plate effectively turned the plate into a flat-bottomed boat which floated freely on the water. The dimensions of the plate were 2.4 m by 1.5 m. These large dimensions helped to ensure that extraneous edge diffractions would not interfere with the signal of interest. To further minimize unwanted edge diffraction three of the four edges were tapered. On the fourth edge (along the width) was glued a 10 mm high by 3 mm thick acrylic bar. It was this edge, when separated from a similar edge on a second plate by the desired distance, which was utilized to simulate an open lead.

B. MODEL OF A PRESSURE RIDGE

A cross sectional view of the single pressure ridge model showing the significant dimensions and scaling is given in Figure 3.1. The scaled dimensions of the sail and keel were designed to fit those of a typical multi-year pressure ridge as given in Section I.B. The keel was manufactured by glueing together two flat strips of 3/8 in acrylic and machining to the specified dimensions and shape. The sail was machined from a single 3/8 in thick acrylic strip. Both the sail and the keel were then glued using an acrylic solvent (K-Lux® solvent cement for acrylic) to a smooth acrylic sheet. Because the Arctic frequency range of interest (50 - 150 Hz) has wavelengths greater than 10 m, which is much greater than the Arctic sea ice thickness, it was not necessary to introduce micro-roughness elements on the laboratory model of the ridge.

C. MODEL OF A RUBBLE FIELD

The construction of the rubble field was the most difficult to achieve of the three models. Statistics of a rubble field, per se, were not available. However, a study of available literature on pressure ridges indicated that a typical mean ice plate thickness of 4.0 m with an underwater depth standard deviation of 1.0 m are representative values for pressure ridges (Wadhams et al, 1985). A rubble field can be described as a field of pressure ridges which are randomly oriented with close (several

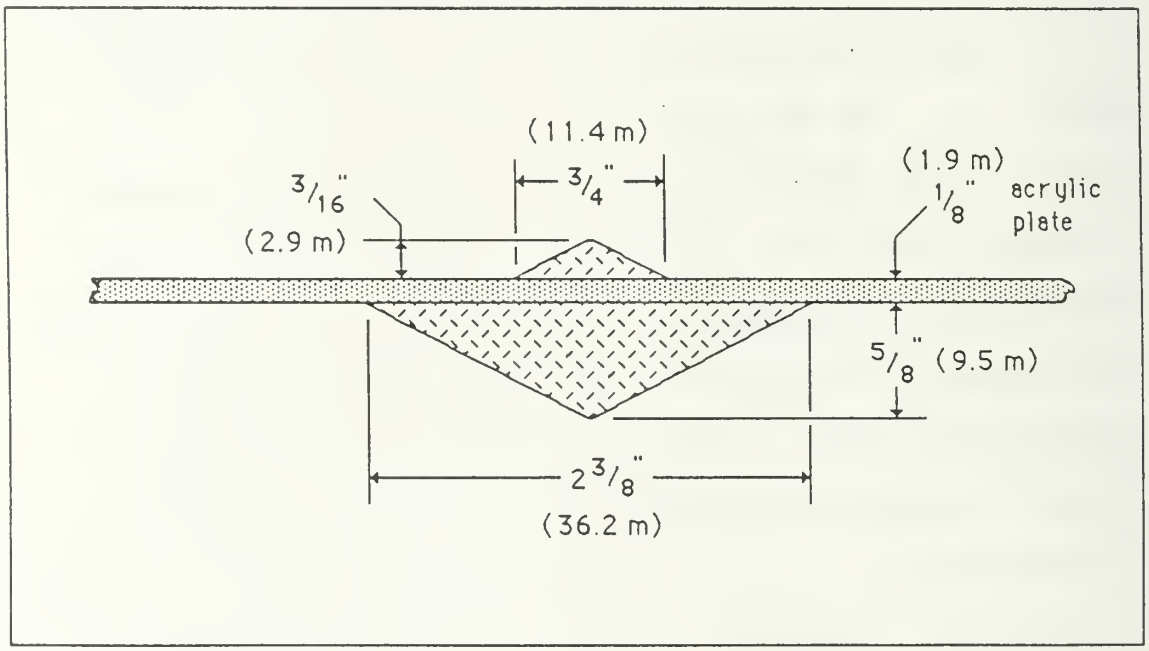

Figure 3.1: Cross section of the pressure ridge model used to measure forward and back scatter from a ridge keel. Dimensions in parenthesis are scaled to the Arctic model. All materials are acrylic.

meters) but variable spacing (Bourke, 1986). Thus, the dimensions as stated above were used as guidelines for the construction of the rubble field. Using the scale 600:1 this corresponds to lab dimensions of 6.7 mm mean thickness and 1.7 mm standard deviation.

The rubble field was constructed from acrylic plates of 3 mm and 9.5 mm thickness which were cut into strips ranging in width between 3 mm and 9 mm. The majority of these strips were then cut again along the width in 3 to 9 mm size strips to form randomly sized blocks of acrylic, and the remaining strips were broken into jagged pieces by chiselling with a sharp-edged hammer. Enough pieces of acrylic were made this way to cover a 3 m^2 surface. The dimensions of the rubble field were 0.6 m by 1.6 m, which when scaled to the Arctic would represent a 360 by 960 m surface area. The pieces were fastened to the top and bottom of the plate using cyanoacrylate adhesive. The rubble was applied so that it would match as closely as possible the dimensions of 6.7 mm mean thickness and the 1.7 mm ice bottom roughness standard deviation stated above.

The statistics for the plate underside roughness were determined using the Random Surface Measuring device (RSM). Six 18 cm long traverses of the plate were completed and a total of 3200 data points were collected at an incremental

distance of 0.332 mm and with a height resolution of 20 μm. A typical profile of the surface is shown in Figure 3.2.

The surface data were processed to determine the mean height and standard deviation with respect to the mean height of the plate underside roughness. The probability density functions of the surface heights and slopes were obtained and are illustrated in Figures 3.3 and 3.4, respectively. The best fit for both of these curves is indeterminate, but it is not gaussian. The acrylic smooth plate thickness is 3.1 mm. The mean thickness of the bottom roughness glued onto the plate is 3.8 mm. The standard deviation of the bottom roughness is 2.76 mm. A plate topside roughness of approximately one-half the thickness of the bottom roughness was also glued onto the plate for purposes of mass loading but its dimensions were not measured. These dimensions represent an Arctic rubble field mean ice thickness of approximately 5 m and an ice bottom roughness standard deviation of 1.65 m.

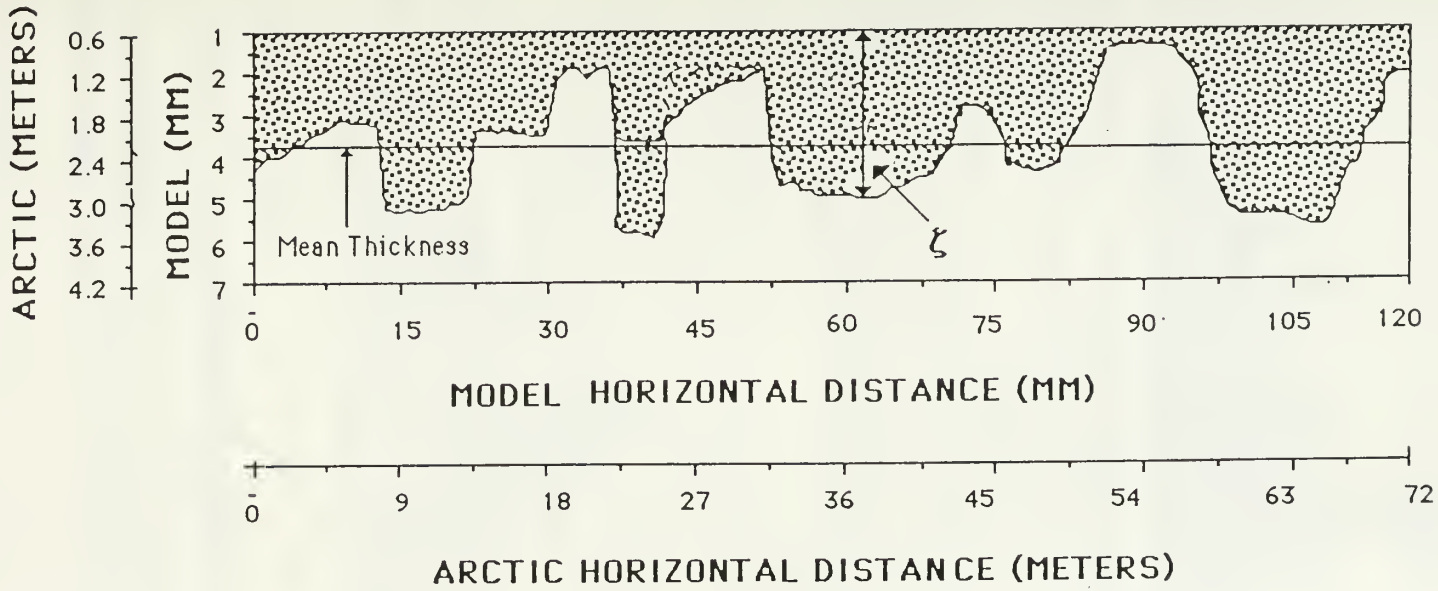

Figure 3.2. Bottom roughness profile of the acrylic "rubble" model. The mean thickness is 3.8 mm. The roughness standard deviation is 2.76 mm. Values of were used for the numerical intetration of Equation 4.8

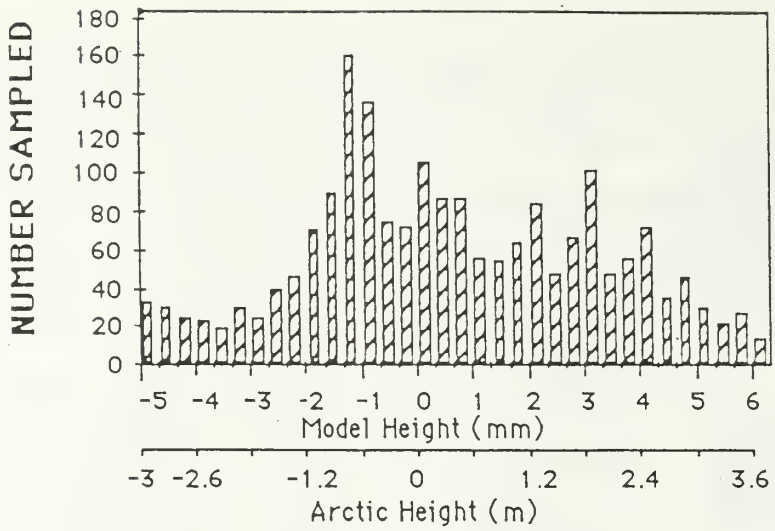

Figure 3.3. Height histogram of the bottom surface of the roughened acrylic plate that was manufactured to model an Arctic rubble field. The height dimensions are presented in actual model dimensions (mm) and in scaled (600:1) Arctic dimensions (m).

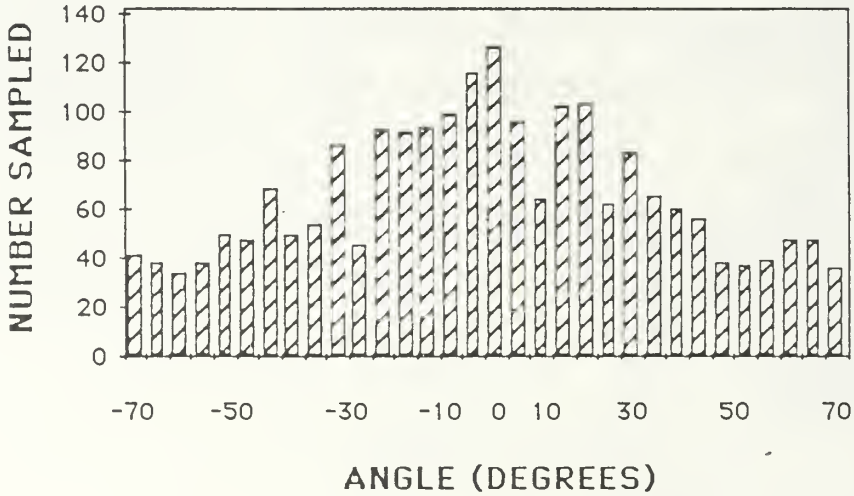

Figure 3.4. Slope histogram of the bottom surface of a roughened acrylic plated used to model an Arctic rubble field.

IV. THEORY

Scattering is defined as the re-radiation of incident acoustic energy by discontinuities in the physical properties of the medium (Urick, 1983). These discontinuities can be manifested in water as air bubbles, a rough air-water interface, or the rough undersurface of the Arctic ice cover. For the purpose of this work scattering from the Arctic ice cover will be composed of the following acoustically significant effects (see Figure 1.2):

1. Pressure waves diffracting from edges and propagating in all directions.
2. Scattering in the specular direction, i.e., the angle of reflection is equal to the angle of incidence.
3. Conversion of the incident acoustic energy to shear and flexural modes, and formation of compressional modes by refraction, in the plate. This energy can be re-radiated back into the water below, or the airspace above, the plate.

The theoretical aspects of each of these effects will be discussed at length in this section.

A. DIFFRACTION

Diffraction can best be visualized using Huygens' principle. When an acoustic wave encounters an obstruction such as the edge of a plate, every point on that edge will be the site of an expanding spherical Huygen's wavelet. The acoustic energy re-radiated in all directions from the edge in these spherical wavelets is called diffraction.

Biot and Tolstoy (1957), in applying the use of normal modes as generalized coordinates in Hilbert Space to mechanical media, developed an exact, closed form, expression for the diffracted pressure wave from a rigid wedge or corner. Medwin (1981) modified the source function used by Biot and Tolstoy to a delta function source that is turned on at time t = 0, and simplified the equation for the diffracted pressure. Figure 4.1 shows a wedge to illustrate the typical cylindrical coordinates used in the diffracted pressure wave equation given below:

$$p(t) = \begin{cases} \dfrac{(-S\rho c/4\pi\theta_w)\{\beta\}\exp(-\pi y/\theta_w)}{[rr_o \sinh y]} & , \quad t \geqslant \tau_o \\ 0 & , \quad t < \tau_o \end{cases} \tag{4-1}$$

Where,

$$\beta = \frac{\sin[(\pi/\theta_w)(\pi \pm \theta \pm \theta_o)]}{1 - 2\exp(-\pi y/\theta_w)\cos[(\pi/\theta_w)(\pi \pm \theta \pm \theta_o)] + \exp(-2\pi y/\theta_w)} \tag{4-2}$$

$$y = \text{arc cosh}\ \frac{c^2 t^2 - (r^2 + r_o^2 + Z^2)}{2rr_o} \tag{4-3}$$

where p(t) is the diffracted pressure at time t, ρ is the density of the medium, S is the source strength, and c is the sound speed in the medium. The source coordinates are $(r_o, \theta_o, 0)$ and the receiver coordinates are (r, θ, z). θ_w is the angle of the wedge measured in the fluid region. The term $(\pi \pm \theta \pm \theta_o)$ is

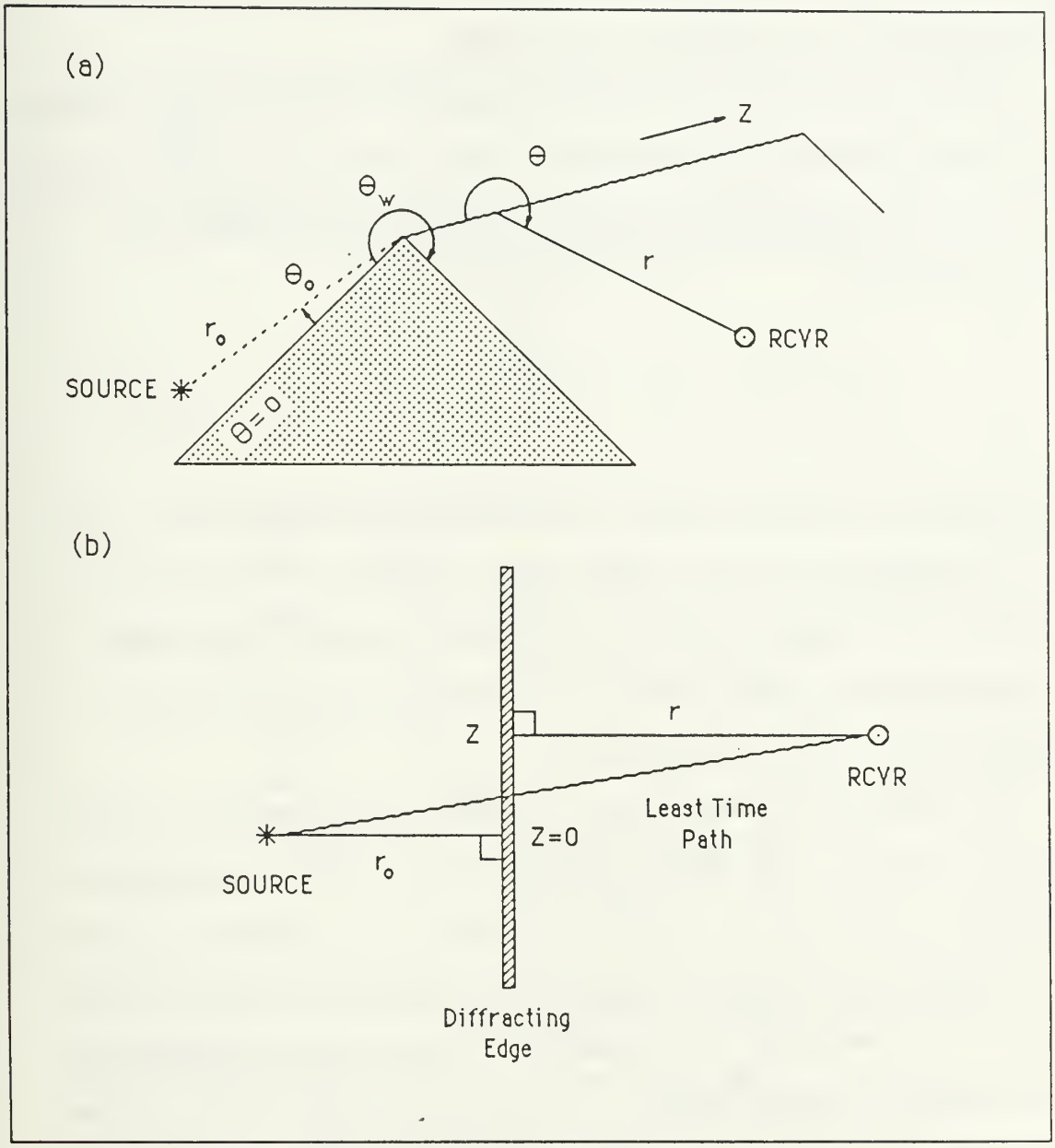

Figure 4.1: (a) Wedge geometry for equations 4-1 thru 4-3. (b) Unfolded geometry.

written for simplicity; the curly bracket in Equation 4-1 consists of the sum of the four terms obtained by using the four possible combinations of the angles, $\pm\theta$ and $\pm\theta_0$.

Physically, the sound energy emanating from the point source diverges spherically, intersects the ridge, and is diffracted to the receiver with the earliest arrival occurring at the least time, (τ_0), given by:

$$\tau_0 = [(r + r_0)^2 + z^2]^{1/2}/c. \qquad (4\text{-}4)$$

Subsequent arrivals are due to diffraction of the spherical wave as it propagates over the wedge from elements of the wedge on either side of where the least time path intersects the wedge. The maximum pressure occurs at the least time and falls off exponentially with increasing time.

The diffracted pressure field from the acrylic model, or the Arctic ice cover, can be determined by the linear superposition (Novarini and Medwin, 1985) of Equation 4-1 applied to a series of wedges that compose a specific feature on the model, or ice cover. For example, the model of the ridge keel is composed of three distinct wedges labeled 1, 2, and 3 in Figure 4.2a. Figure 4.2b shows the result of applying Equation 4-1 to each of the wedges, with $r = r_0$ and $\theta = \theta_0$, and summing.

Consider the ridge keel as a linear system whose output is the diffracted pressure, then the system diagram is

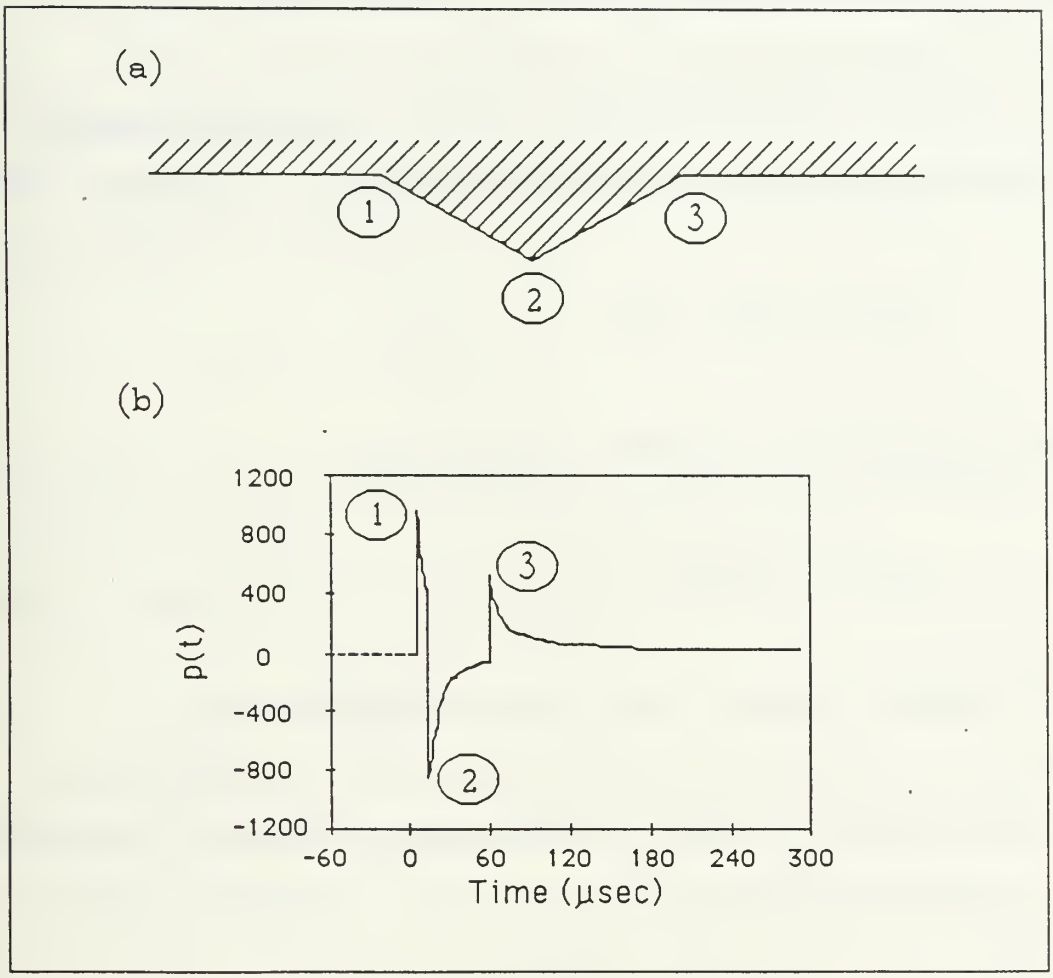

Figure 4.2: (a) Diagram showing the three Biot-Tolstoy wedges that make up the model of the ridge keel.
(b) Time domain impulse response calculated using Biot-Tolstoy theory and superposition. Relative times of arrival for a backscattering geometry.

$$\delta(t) \rightarrow \boxed{H(f)} \rightarrow h(t)$$

where $h(t)$ is the impulse response of the filter and $H(f)$ is the Fourier transform of $h(t)$ and is called the transfer function. The diffracted pressure response, $p_s(t)$, for the pulsed sinusoid, $y(t)$ (see Figure 2-2), is the convolution of $y(t)$ with $h(t)$;

$$p_s(t) = y(t) * h(t).$$

Using the convolution theorem, this becomes,

$$P_s(f) = Y(f)H(f)$$

in the frequency domain. The pressure response in the frequency domain relative to direct free-field transmission at a reference range R_o is simply the filter transfer function multiplied by the reference range:

$$P_{rel}(f) = \frac{P_s(f)}{Y(f)/R_o} = \frac{Y(f)H(f)}{Y(f)/R_o} = H(f)R_o$$

In this treatment, the diffracted pressure from Equation 4-1 is given by:

$$p(t) = (\rho S/4\pi)\delta(t)*h(t),$$

in the time domain, such that,

$$P(f) = (\rho S/4\pi)H(f)$$

in the frequency domain. Now the relative frequency domain pressure response for any given source can be calculated from the Fourier transform of Equation 4-1 by:

$$P_{rel}(f) = \frac{4\pi R_o}{\rho S} P(f)$$

Although there is no complete analytical transform for Equation 4-1, the transformation can be performed using digital techniques. Equation 4-4 then becomes:

$$P_{rel}(f) = \frac{4\pi R_o \Delta t}{\rho S} P(f) \qquad (4\text{-}5)$$

where Δt is the sampling interval and is equal to the reciprocal of the sampling frequency used in the digitization of Equation 4-1 (Brigham, 1974). Medwin et al (1982), using a discrete Huygens interpretation, obtained a finite value for $p(t=\tau_0)$ and showed that this was related to $p(t=\tau_0+\Delta t)$ by

$$p(t=\tau_0)/p(t=\tau_0+\Delta t) = 1.366. \qquad (4\text{-}6)$$

Biot and Tolstoy develped their theory using infinite dimensions for the wedge, and rigid boundary conditions. The

wedges that make up the ridge keel and leads in the laboratory models (and in the Arctic) have finite dimensions and real, impedance boundaries. Novarini and Medwin (1985) report that the Biot-Tolstoy theory with discrete Fourier transformation can be applied to finite wedges as long as the wedge separations are greater than one-quarter wavelength. Experimental verification can be found in Medwin et al (1982) and excellent agreement between theory and experiment for a rigid wedge is given in Medwin (1981). To date the effect of non-rigid boundary conditions on the Biot-Tolstoy diffraction theory has not been investigated, but it is expected that a non-rigid wedge will give less diffraction than a rigid wedge, due to the conversion and refraction of incident acoustic energy to acoustic energy in the medium of the wedge.

B. ROUGH SURFACE FORWARD SCATTER FROM A RUBBLE FIELD

The use of the Helmholtz theorem with the Kirchhoff plane wave approximation was first applied by Eckart (1953) to calculate the acoustic field scattered by a Gaussian rough plane surface. It has been shown that the coherent component of the scattered signal can be obtained by averaging the signal over the probability density function (PDF) of the rough surface (Clay and Medwin, 1977). For specular scatter, when $\theta_{scattered} = \theta_{incident}$, in addition to the coherent component, $\langle p \rangle$, due to the statistically weighted <u>height-dependent</u> phase shift, there is an incoherent component due to the <u>spatially</u> dependent phase shifts

as determined by the spatial correlation of the heights. That is,

$$<p^2> = <p>^2 + \mathrm{Var}(p) \qquad (4\text{-}7)$$

where $<p^2>$ is the total scattered intensity and $<p>^2$ is the coherent component. For a low roughness surface, $k\sigma\cos\theta_i < 1$, the coherent component dominates and the coherent scattered intensity is approximately equal to the total scattered energy, i.e., $<p>^2 \simeq <p^2>$. Here $k = 2\pi/\lambda$, σ = root mean square (rms) height of the roughness elements, and θ_i = angle of incidence measured from the normal.

The received signal from sound specularly scattered from a rough surface is the sum of the scattered signals from all of the scattering elements of various heights ensonified by the incident plane wave, and arriving at the receiver in the selected time window. The probability of occurrence of a specific height of a scattering element between ζ and $\zeta + d\zeta$ is $\omega_a(\zeta)\,d(\zeta)$, where ζ is the height above the mean level and $\omega_a(\zeta)$ is the PDF of the rough surface. The effect of ζ on the signal is to alter the phase by $-2k\zeta\cos\theta_i$. Equation 4-8 derives the mean value of the coherent reflection coefficient ,$<R_r>$, by multiplying the effect of $\exp(-2ik\zeta\cos\theta_i)$ by $\omega_a(\zeta)$ and integrating over all values of ζ. (Clay and Medwin, 1977)

$$\langle R_r \rangle = R_s \int_{-\infty}^{\infty} \exp(-2ik\zeta\cos\theta_1)\omega_a(\zeta)d\zeta \qquad (4\text{-}8)$$

where R_s is the plane wave smooth surface pressure reflection coefficient.

Assume the rough surface has a Gaussian PDF, Equation 4-9. Then, substitution of Equation 4-9 into Equation 4-8 and evaluation of the infinite integral results in Equation 4-10 which describes the magnitude of the coherent component of the specular scatter due to the roughness elements

$$\omega_g(\zeta) = \sigma^{-1}(2\pi)^{-1/2}\exp(-\zeta^2/[2\sigma^2]) \qquad (4\text{-}9)$$

$$\langle R_r \rangle / R_s = \exp(-2k^2\sigma^2\cos\theta^2) = \exp(-g\ /2) \qquad (4\text{-}10)$$

where g is defined as a roughness parameter dependent on frequency ($k = 2\pi f/c$), incident angle (θ), and rms height of the roughness elements (σ).

This theory assumes several conditions which are not met in the Arctic or in this experiment, namely: incident plane waves, low roughness, i.e., $g < 1$, and no steep-sloped roughness elements. Spherical waves will diverge as 1/range while propagating; this factor will be corrected later (Equation 5-3). The fact that $g > 1$ in some of our experiments will result in $\langle R_r^2 \rangle$ greater than $\langle R_r \rangle^2$; that is Equations 4-8 and 4-10 do

not measure the total scattered energy. Finally Equation 4-8 is derived for gently sloped roughness elements, i.e., less than 10° slopes, whereas the Arctic, and our model, has roughness elements with slopes as great as 90°. Therefore, for a roughness parameter greater than 1 there will be additional energy at the receiver due to the increasing significance of the incoherent signal component. Hence, we would expect a received signal $<p^2>$ larger than theory predicts for $<p>^2$.

C. REFLECTION FROM A SMOOTH PLATE

The calculation of the plane-wave smooth surface reflection coefficient, R_s, for a lossy, multilayered medium such as Arctic ice is a complicated problem due to its complex and anisotropic nature. The lossy, multilayered smooth ice plane-wave reflection coefficient was recently studied by McCammon and McDaniel (1985). They extended the Thompson-Haskell matrix method to treat a layered viscoelastic medium, i.e., ice bounded by two fluid half spaces, water and air. In their computer model they incorporated the density, the bulk compressional speed and attenuation, and the bulk shear speed and attenuation constants of ice. They reported that ice thickness and shear attenuation were the critically important paramenters in determining R_s. They were kind enough to provide us with a copy of this program in order to derive theoretical predictions for the smooth acrylic plate reflection coefficient.

C. FLEXURAL WAVES IN SMOOTH PLATES

Flexural waves in plates arise as a result of transverse vibrations at frequencies $kh < 1$, where k is the horizontal wavenumber and h is the plate thickness. There is a displacement perpendicular to the plane of the plate that propagates in a direction that is parallel to the plane of the plate.

An excellent review of the derivation of the flexural wave equation for both uniform beams and plates is contained in Ross (1976). In his treatment he uses a non-dimensional shear parameter (Γ_p)

$$\Gamma_p = Y/[K_p G(1-\sigma^2)] \qquad (4\text{-}11)$$

for the plate, which relates Young's Modulus (Y) to the shear modulus (G). The factor, $K_p(1-\sigma^2)$, is included to account for warping in the plate cross section resulting in a non-constant shear force. For a plate,

$$K_p \simeq 0.76(1 + 2\sigma/5). \qquad (4\text{-}12)$$

where σ is Poisson's ratio.

Assuming that the spatial derivitive of thickness is negligible, the homogeneous bending equation for a plate is given by

$$\frac{\partial^2 y}{\partial t^2} + \frac{c_p^2 h^2}{12} \nabla^4 y - \frac{(\Gamma_p + 1)h^2}{12} \nabla^2 \frac{\partial^2 y}{\partial t^2} + \frac{\Gamma_p h^2}{12 c_p^2} \frac{\partial^4 y}{\partial t^4} = 0 \qquad (4\text{-}13)$$

where y is the displacement perpendicular to the plane of the plate, c_p is compressional wave speed in the plate, and h is plate thickness. Two of the solutions to this equation are real, and two are imaginary. The general solution can be expressed as (Ross, 1976; Kinsler et al., 1982):

$$y = [Ae^{-ikx} + Be^{ikx} + Ce^{-\gamma x} + De^{\gamma x}]e^{i\omega t}, \qquad (4\text{-}14)$$

where $\omega = 2\pi f$, k is the flexural wavenumber = ω/v_f, v_f is the flexural wave phase speed, $\gamma = ik$, where $i = (-1)^{1/2}$, and **A**, **B**, **C**, and **D** are complex coefficients determined by the boundary conditions.

1. <u>Flexural Phase Speed</u>

Flexural waves travelling in a plate propagate at a phase speed given by ω/k. Substituting the harmonic solution from Equation 4-14 back into Equation 4-13 gives:

$$\omega^2 - c_p^2 \frac{h^2}{12} k^4 + (\Gamma_p + 1)\frac{h^2}{12}\omega^2 k^2 - \frac{\Gamma_p}{c_p^2}\frac{h^2}{12}\omega^4 = 0 \qquad (4\text{-}15)$$

which can be solved for the flexural wave phase speed, v_f, by substituting ω/v_f for k, and solving the resulting quadratic equation. This gives

$$v_f^2 = \frac{\sqrt{B^2 - 4AC} - B}{2A}$$

$$A = \frac{1}{\omega^2} - \frac{\Gamma_p h^2}{c_p^2 12}$$

$$B = (\Gamma_p + 1)\frac{h^2}{12} \qquad (4\text{-}16)$$

$$C = -c_p^2 \frac{h^2}{12}$$

Note, that at low frequencies, A is dominated by $1/\omega^2$, therefore 4AC dominates B^2 and $(4AC)^{1/2}$ dominates B resulting in the familiar equation for flexural wave speed given by Kinsler et al. (1982):

$$v_f = \sqrt{\frac{\omega c_p h}{\sqrt{12}}} \qquad (4\text{-}17)$$

At low frequency the flexural wave phase speed is proportional to the square root of the frequency (see Figure 4.3).

At very high frequencies, $A \rightarrow -(\Gamma_p h^2)/(c_p{}^2 12)$, and the flexural wave phase speed becomes a constant, i.e., as $f \rightarrow \infty$,

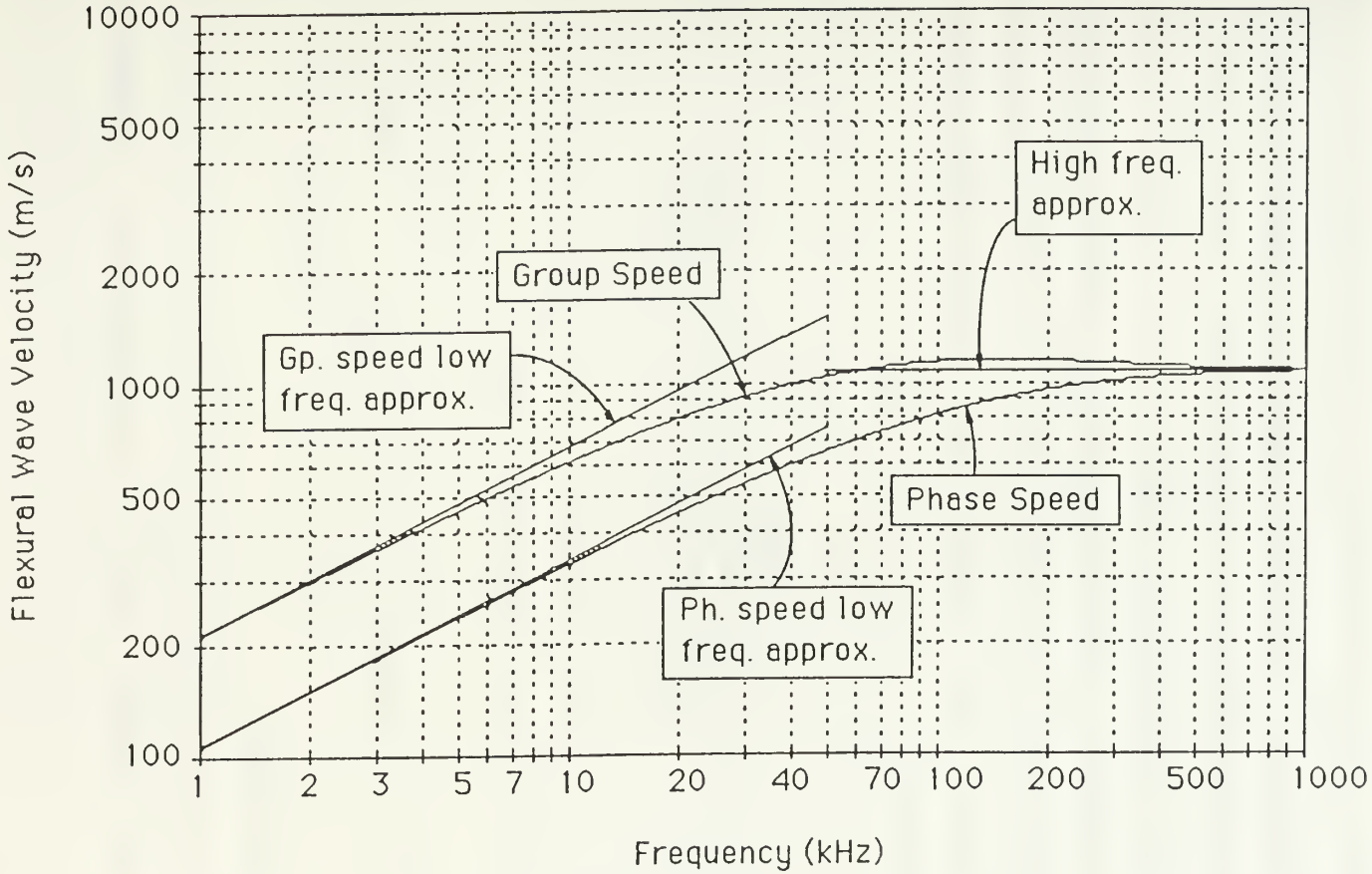

Figure 4.3: Theoretical flexural wave phase and group speeds as a function of frequency. Also plotted are the high and low frequency approximations for phase and group speed as derived in the text.

$$v_f^2 = c_p^2/\Gamma_p. \tag{4-18}$$

Therefore the flexural wave phase speed is dispersive with $(f)^{1/2}$ at low frequencies, and non-dispersive at high frequencies. It is the proportionality for low frequency speed, $v_f \sim (\omega h)^{1/2} \sim (h/\lambda)^{1/2}$, that permits scale modeling to be feasible for flexural waves.

2. Flexural Wave Group Speed

Group speed v_g is given by $d\omega/dk$. This can be obtained by solving Equation 4-15 for ω^2, then solving for the derivative of ω with respect to the wavenumber k. This results in the following expression:

$$v_g = \frac{kc_p^2}{2\omega\Gamma_p}\left[(\Gamma_p + 1) - \frac{k^2\frac{h^2}{12}(\Gamma_p - 1)^2 + \Gamma_p + 1}{\sqrt{(\Gamma_p - 1)^2(k^2\frac{h^2}{12})^2 + 2(\Gamma_p + 1)k^2\frac{h^2}{12} + 1}}\right] \tag{4-19}$$

It can be shown that as ω gets very small,

$$v_g = d\omega/dk \rightarrow 2[\omega c_p h/\sqrt{12}]^{1/2} = 2v_f|_{\omega\ \mathrm{small}}. \tag{4-20}$$

As ω gets very large,

$$v_g = d\omega/dk \rightarrow c_p^2/\Gamma_p = v_f|_{\omega\ \mathrm{large}}. \tag{4-21}$$

That is, at low frequencies the group speed is twice the phase speed and at very high frequencies the group and phase speeds are the same. A plot of the flexural wave phase and group speeds as a function of frequency for a 3 mm thick acrylic plate in air is given in Figure 4.3.

3. <u>The Effect of Entrained Mass on Flexural Wave Speeds</u>

The medium in which the plate is situated will affect the net radiation impedance seen by the vibrating plate. The reactance term of the radiation impedance can be viewed as the effect of the entrained mass of the medium directly surrounding the vibrating plate (Kinsler et al., Chap 8, 1982). If the medium is air, then the effect of the entrained mass in the above equations will be negligable. However, if the medium is water, the entrained mass will be significant and a correction to the equations for phase and group speeds will have to be used.

Letting ϵ be the ratio of entrained mass to the plate mass, the terms in Equation 4-13 become modified as follows:

$$\Gamma_p \rightarrow \Gamma_p(1-\epsilon), \quad \text{and}$$

$$h^2 \rightarrow h^2/(1-\epsilon).$$

The flexural wave phase speed can then be determined in the same manner as described above, with the resulting low frequency approximation given by:

$$v_f^2 = \omega c_p h/[12(1+\epsilon)]^{1/2} \quad , \; kh < 1 \qquad (4\text{-}22)$$

At high frequencies, the radiation reactance goes to zero, therefore the effect of the entrained mass disappears and the high frequency approximation is the same as Equation 4-18.

Entrained mass will reduce the flexural wave phase and group speed at low frequencies, but as frequency increases the effect of the entrained mass becomes less and becomes zero as frequency approaches infinity.

4. Boundary Layer Formation due to Flexural Waves.

The condition necessary to achieve efficient mode conversion between compressional waves in the water and flexural waves in the plate is to match the horizontal component of the compressional wavenumber (κ) in the water with the flexural wavenumber (k_f) in the plate. The condition of matching horizontal wavenumbers is known as coincidence. Both in the laboratory model and in the Arctic, the speed of flexural waves is less than the compressional wave speed in the water underlying the plate for all frequencies. Therefore, the condition for efficient mode conversion is never satisfied due to the subsonic nature of the flexural wave compared to waterborne waves, i.e., k_f is always greater than κ.

Any modes re-radiated into the water from a subsonic flexural wave in a plate will be evanescent, that is, the energy will decay exponentially with distance from the plate instead of propagating as a harmonic wave. In a recent paper Tolstoy

(1986) showed that this should form an acoustic boundary layer below the plate and developed expressions for the pressure field in this boundary layer for smooth and rough plates. For a point source located in the water at a depth z_0 below a smooth plate and a receiver at a depth z, the magnitude of the pressure in the boundary layer (neglecting attenuation) relative to freespace acoustic pressure is given by:

$$\frac{P_B}{P_D} = \sqrt{2\pi r}\,\frac{g}{g^2 + k_f^2}\,\frac{(kc)^2}{v_f\, v_g \sqrt{k_f}}\,\exp[-g(z+z_0)] \qquad (4\text{-}23)$$

where r is the horizontal distance between source and receiver, P_D is twice the freespace acoustic pressure at r, k and c are the compressional wavenumber and wave speed in water, respectively, k_f is the flexural wavenumber for the plate, and $g = (k_f^2 - k^2)^{1/2}$. If attenuation in the plate is significant, this equation should be multiplied by $\exp(-\alpha r)$ where α is the flexural wave attenuation coefficient in Np/m for the plate.

V. SPECULAR SCATTER

A. EXPERIMENTAL PROCEDURE

1. Data Collection

Laboratory measurements of the smooth plane wave pressure reflection coefficient ($\mathbf{R_s}$), the rough surface coherent pressure reflection coefficient ($\mathbf{R_r}$), and the wedge forward specularly scattered pressure were made at specular angles in the water-filled tank described in Chapter II. Both the source and receiver were mounted on angled stainless steel rods of 3 mm diameter and were lowered into the tank between the edge of the model plate and side of the tank. Using clamps and a lead weight anchor located next to the tank, the hydrophones could be positioned anywhere in the tank.

Mounted to the source with the same size steel rod was an additional LC-10 acting as a receiver. With these two hydrophones colocated, the position of the source at the desired range and angle was accurately determined by measuring the travel time of the vertically propagating surface reflected signal and the travel time for the case of the rough surface or wedge. The receiver was positioned at the same depth as the source by measurement with a meter stick and the range was adjusted by measurement of the direct path travel time between source and receiver. A second hydrophone attached to the receiver would have allowed a more precise receiver depth

measurement, however, due to the probability of unwanted scattering, this method was not utilized. The positioning method utilized insured that the signal received was the specular scattered signal, i.e., the angle of incidence equalled the angle of scatter. Once positioned, the source and receiver remained fixed throughout the data run. A set of reference data was then collected by reflection off the smooth water surface (reflection coefficient = −1).

For the rough surface measurements, two additional data sets were required. First, to determine the plane surface acrylic plate reflection coefficient, the smooth plate section of the acrylic sheet was centered on the water surface between the source and receiver and reflected amplitudes in the specular (mirror) direction were recorded for a range of frequencies. Second, to determine the rough surface reflection coefficient, the rubble surface of the model was centered by measuring the backscatter slant range as described above and the forward specularly scattered pressure amplitudes were recorded.

For measurements of the forward scattering from a single wedge fastened to the underside of a smooth acrylic plate, only one additional data set was required – that of the forward specularly scattered pressure off the wedge. The positioning of the wedge equidistant from source and receiver and at the desired grazing angle was accomplished as described above.

2. Signal Processing

For the effective frequency range of 30 - 90 kHz, a frequency resolution, Δf, of at least 5 kHz was required in order to discern the peaks and troughs of the plotted data. The FFT algorithm used for processing the time domain pressure response required 'power of 2' sample points. For the minimum frequency resolution of 5 kHz, the number of points used for the FFT was 256. Therefore, the actual frequency resolution, computed using Equation 5-1 was 3906.25 Hz. The transmitted signals were sinusoidal and were multiples of 3906.25 Hz.

$$\Delta f = \frac{\text{sampling frequency}}{\text{number of samples}} = \frac{1,000,000}{256} = 3906.25 \text{ Hz} \qquad (5\text{-}1)$$

Due to a typical interference-free time window of less than 100 usec, it was possible to collect only 64 time domain pressure sample points. Therefore, it was necessary to zero-pad the remaining 192 bins used for the FFT.

The received signal was amplified 2000 times and filtered from 2 kHz to 300 kHz by the Ithaco Low Noise Preamplifier, then amplified another 20 dB and sent to the analog to digital converter and signal processor. Conversion to the frequency domain for analysis was performed on the signal average of 300 time domain measurements.

B. RESULTS AND DISCUSSION

1. Results of Reflection from a Level Ice Model

The plane wave reflection coefficient for a smooth surface is defined as $R = p / p_{in}$ where p is the reflected pressure from the smooth acrylic plate and p_{in} is the incident pressure. The term p_{in} can be determined by the perfectly reflected pressure from the water-air interface.

For spherically diverging waves we use

$$R_s = \frac{p\ (R_1 + R_2)}{p_o R_o} \qquad (5\text{-}2)$$

In the above equation,

R_1 = Slant range from source to specularly reflecting point on the plate

R_2 = Slant range from plate to receiver

p = Reflected pressure. The pressure of the received signal reflected from the water-smooth plate interface as measured at range R_2.

p_o = Reference pressure. The pressure of the received signal reflected from the water - air interface.

R_o = Range at which reference pressure is measured.

As described in the procedure above, for each grazing angle, $R1 = R2 = 0.5R_0$. Therefore, the range dependence drops out and the reflection coefficient becomes the ratio of the scattered received pressure divided by the reference reflected pressure. The reference pressure for both cases is the reflected pressure from a smooth water surface.

Measurements of the smooth plate reflection coefficient were made at five different grazing angles between 30 to 70 degrees. For each angle, pressure measurements were collected at frequencies of 30.3, 50.8 and 74.2 kHz and are tabulated in Table III. The reflection coefficients computed using Equation 5-2 are plotted as dark squares for the above frequencies in Figures 5.1, 5.2 and 5.3, respectively. The solid line is each plot is the predicted pressure reflection coefficient from McCammon and McDaniel's computer model of reflection from arctic plates using as inputs the parameters of the bulk physical constants of the laboratory acrylic plate. Those parameters had previously been measured in our laboratory samples of acrylic material. The computer model predicts a single reflection null which is independent of frequency at 47° angle of incidence. The measured reflection minima range from 44° to 56° grazing angle. Since acrylic is a homogeneous viscoelastic material, the magnitude of the reflection coefficient at the null will decrease with increasing frequency. There is some evidence of this.

TABLE III

SMOOTH PLATE REFLECTION COEFFICIENT

	REFLECTION COEFFICIENT		
Frequency (kHz)	30.3	50.8	74.2
Grazing Angle (degrees)			
39	0.99	1.0	1.0
44	0.73	0.93	0.95
49	0.96	0.92	0.80
56	1.0	0.68	1.0
63	1.0	0.95	0.94

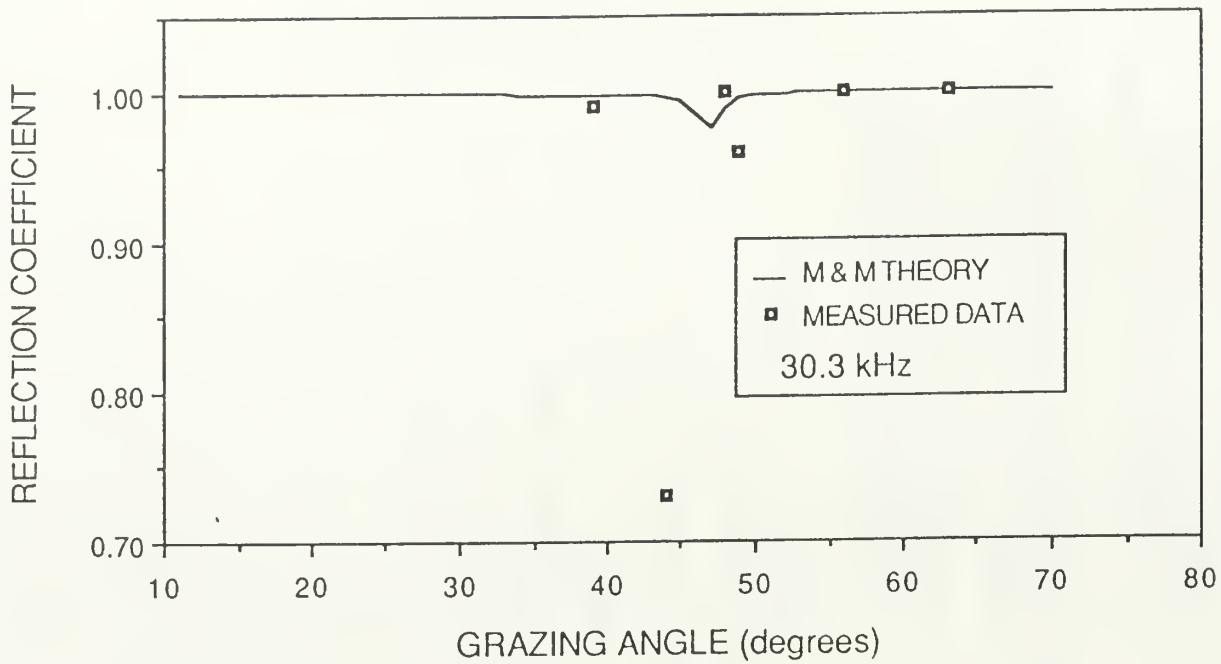

Figure 5.1. Smooth acrylic plate reflection coefficient.

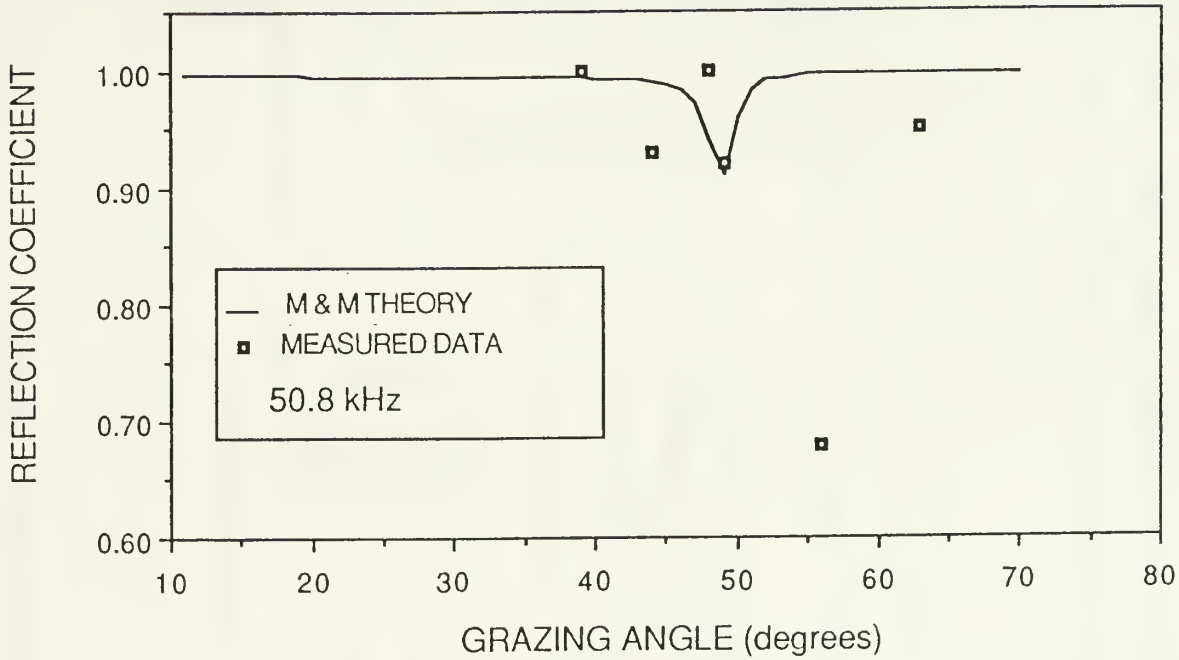

Figure 5.2. Smooth acrylic plate reflection coefficient.

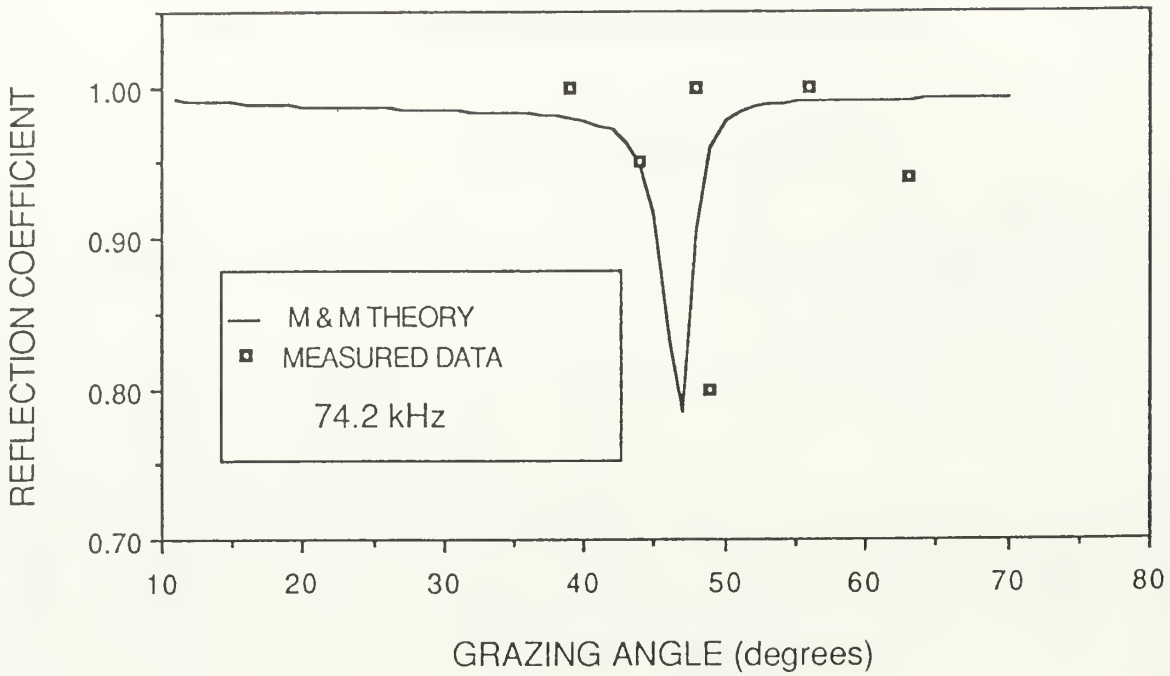

Figure 5.3. Smooth acrylic plate reflection coefficient.

On the whole, the laboratory results using a point source compare well with the computer model predictions for plane waves. Better agreement between theory and experiment could have been achieved by adjustments of our input speeds and attenuations. For example, a smaller compressional attenuation would yield deeper troughs in the computer calculations. We preferred not to make these adjustments. Although it was not our intent to verify the accuracy of McCammon and McDaniel's computer model, our results do show good agreement with their model predictions.

2. Results of Coherent Specular Scatter from a Model of a Rubble Field

The plane wave coherent reflection coefficient for a randomly rough surface is defined as $R_r = \langle p \rangle / p_{in}$ where $\langle p \rangle$ is the average pressure of the forward scattered received signal measured for many realizations of the statistically rough surface. This concept is a generalization of the smooth plane surface reflection coefficient, R_s, which is the reflection coefficient derived from p, the pressure of the received signal reflected from a water - smooth acrylic plate interface. Equation 5-3 defines R_r for spherically diverging waves.

$$R_r = \langle p \rangle \frac{(R_1 + R_2)}{p_o R_o} \qquad (5\text{-}3)$$

R_1, R_2, p_o and R_o are as defined for Equation 5-2. Figure 5.4 is a plot of the mean of the square of the ratio of the specularly-scattered pressure relative to smooth plate reflected pressure, i.e., $<(R_r/R_s)^2>$, for different frequencies and angles of incidence. The abscissa of the plot is the surface roughness parameter, g, for specular scatter. This parameter is a dimensionless quantity which incorporates the rms surface height, sound frequency and incidence angle, θ_i. Instead of scattering from different surfaces in order to get the **average** reflection coefficient, averaging has been performed over a range of angles and frequencies for bands ± 0.25 g. The data, before averaging, are listed in Table IV.

The measured data is plotted in Figure 5.4 against two theoretical curves: the solid curve is a plot of Equation 4-10 for a Gaussian PDF of heights and assuming R_s is equal to 1. We have used the measured rms height deviation of the roughness elements for the assumed gaussian standard deviation. The dashed curve is a plot of the numerical integration of Equation 4-8, incorporating the measured pdf of the rough surface and assuming $R_s = 1$. There is little difference between these two predictions which suggests that the non-Gaussian PDF of the model (and of the Arctic) does not cause a large error in the predicted coherent specular scatter. Analysis of the plot indicates that the Helmholtz theory provides reasonably accurate predictions of the specularly scattered rms intensities for values of $g < 1$, i.e., low roughness. However at these grazing angles

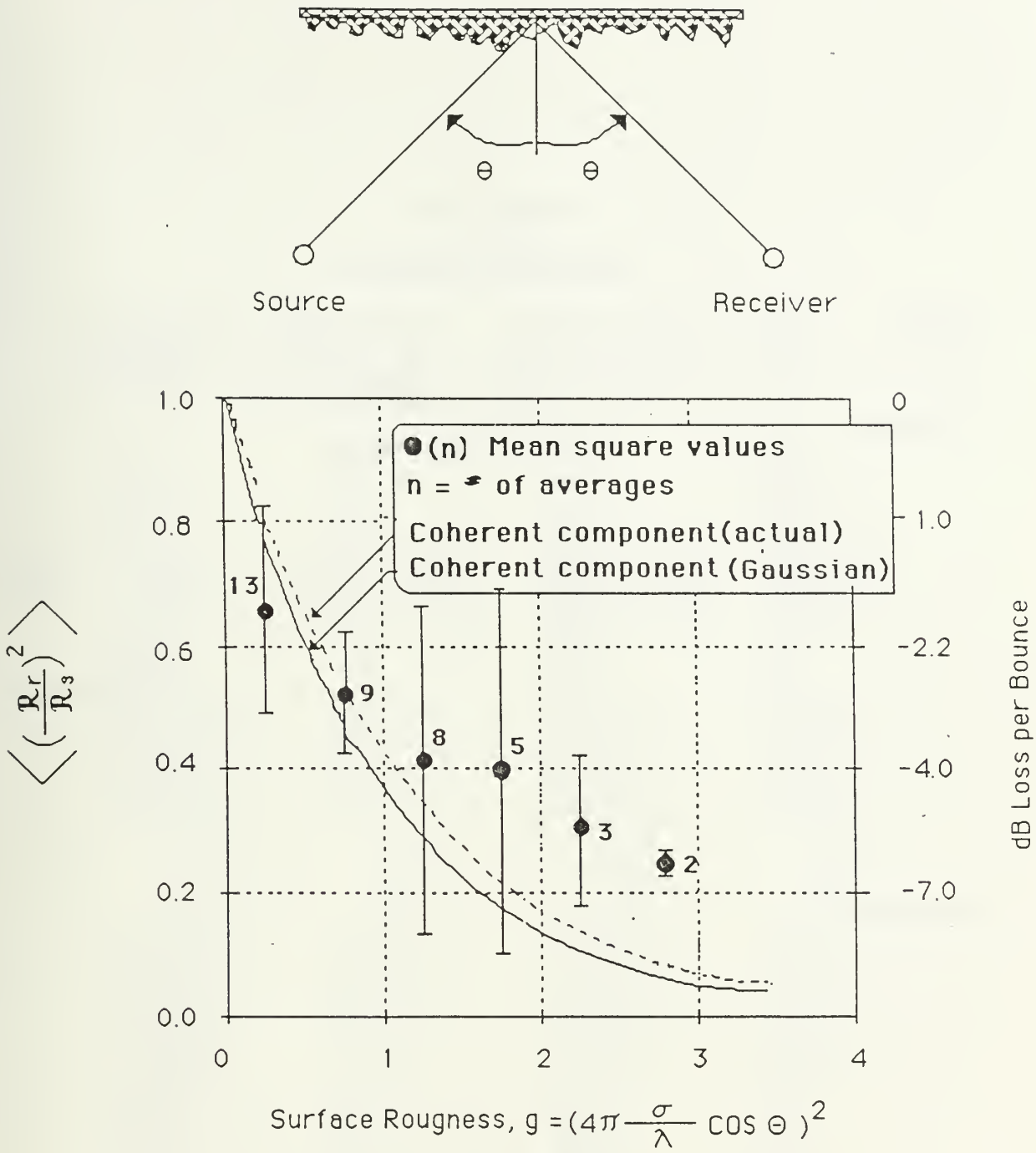

Fig. 5.4 Specular scatter at model of water-rubble ice bottom interface. Smooth curve represents the theoretical value for the coherent component of scatter from a Gaussian surface. Dashed curve represents the theoretical value for the coherent component of scatter from the measured statistical surface. In both theoretical cases, R_S is assumed 1. Dots represent mean of experimental results. Bars indicate standard deviation measured over several frequencies and angles. Boldface number indicates number of data points averaged.

TABLE IV

PRESSURE RATIOS

Grazing Angle	Freq (kHz)	Smooth Plate/ Air to Water Interface, <Rs>	Rough Plate/ Air to Water Interface, Rr	Roughness Parameter, (g)
39 degrees				
	31.3	0.98	0.80	0.213
	35.2	0.88	0.63	0.269
	39.1	0.94	0.44	0.332
	43.0	1.00	0.51	0.402
	46.9	1.00	0.69	0.478
	50.8	1.00	0.62	0.561
	54.7	1.00	0.57	0.650
	58.6	1.00	0.75	0.746
	62.5	1.00	0.77	0.848
	66.4	1.00	0.72	0.958
	70.3	1.00	0.60	1.073
	74.2	1.00	0.31	1.196
	78.1	1.00	0.12	1.325
	82.0	1.00	0.06	1.460
49 degrees				
	31.3	0.98	0.86	0.306
	35.2	0.97	0.86	0.387
	39.1	0.96	0.83	0.478
	43.0	0.95	0.75	0.578
	46.9	0.93	0.75	0.687
	50.8	0.92	0.70	0.806
	54.7	0.89	0.72	0.935
	58.6	0.89	0.72	1.073
	62.5	0.86	0.76	1.220
	66.4	0.76	0.87	1.377
	70.3	0.82	0.79	1.544
	74.2	0.80	0.76	1.720
	78.1	0.77	0.67	1.977
	82.0	0.73	0.48	2.100

TABLE IV (cont'd)

PRESSURE RATIOS

Grazing Angle	Freq (kHz)	Smooth Plate/ Air to Water Interface, <Rs>	Rough Plate/ Air to Water Interface, Rr	Roughness Parameter (g)
63 degrees				
	31.3	1.00	0.88	0.427
	35.2	0.90	0.89	0.539
	39.1	1.00	0.87	0.666
	43.0	0.91	0.85	0.805
	46.9	0.93	0.79	0.958
	50.8	0.95	0.70	1.124
	54.7	0.89	0.62	1.303
	58.6	0.97	0.52	1.495
	62.5	0.88	0.44	1.701
	66.4	0.95	0.40	1.920
	70.3	0.87	0.40	2.152
	74.2	0.94	0.44	2.397
	78.1	0.89	0.46	2.656
	82.0	0.89	0.40	2.928

for $g > 1$ there is a noticeable increase in the measured reflection coefficient relative to both theories for the coherent component alone. This trend is due to the increasing contribution of incoherent scattering from the steep-sloped roughness elements. The relatively large variance in the measurments for $1 < g < 2$ is due to the sensitive dependence on angle near the resonance.

3. Results of Forward Specular Diffraction from a Model of a Ridge Keel

Forward scatter from a single ridge keel mounted on a viscoelasctic smooth plate requires consideration of both the modified Biot-Tolstoy theory for forward diffraction from the ridge keel and the McCammon and McDaniel computer model predictions for reflection from a smooth viscoelastic plate. For a plate with a ridge mounted to its underside, one possible method to compute the energy reflection coefficient is defined by Equation 5-4. This method weighs the contribution of each theory's results by the percent of the total ensonified area which applies to the theory.

$$\text{Energy Reflection Coefficient} = \frac{(P^2_{wedge})(A_w) + (P^2_{plate\ out})(Ap)}{(P^2_{in})(A_t)} \qquad (5.4)$$

In Equation 5-4 it is assummed that:

1. A_t = total scattering area.

2. A_w = area of wedge ensonified.

3. A_p = area of smooth plate ensonified = $A_t - A_w$.

4. There is incoherent energy addition since:

   a. Wedge scatter is independent of plate scatter.

   b. The region of scatter is approximately at the 45th Fresnel Zone, at which region the zone width is about 0.5 cm.

The size of the ensonified elliptical area was determined by computing the semi-major and semi-minor axes based on the geometry of the experimental set-up and length of the time window.

In this experiment all three edges of the ridge keel are ensonified by the incident sound energy, therefore, each of the three edges of the ridge keel must be considered when computing the total forward diffraction. The forward diffraction measurements are reported in terms of loss per bounce, i.e., 20 log (received pressure amplitude of sound diffracting from the ridge keel / received pressure amplitude of sound reflecting off a smooth water surface). Table V contains the measured data used to generate the above three plots. Figures 5.5, 5.6 and 5.7 plot measured results and compare the results with the theoretical predictions for grazing angles of 27°, 45° and 57°, respectively. In the upper half of each figure is an insert showing a source emanating acoustic energy which is being diffracted by each of the three edges (discontinuities) of the finite ridge keel. Reflected diffractions have not been

TABLE V

WEDGE FORWARD SCATTER DATA

Frequency(kHz)	Loss per bounce (dB re perfect reflection)		
	Grazing Angle(degrees)		
	33	45	63
31.3	-1.83	-1.52	-4.22
35.2	-1.86	-2.73	-4.50
39.1	-2.65	-4.30	-5.64
43.0	-1.94	-4.27	-4.31
46.9	-2.50	-6.45	-5.06
50.8	-2.24	-6.10	-3.49
54.7	-2.08	-2.85	-2.93
58.6	-1.64	-5.50	-3.65
62.5	-1.13	-4.88	-2.12
66.4	-0.57	-3.81	-3.03
70.3	-0.71	-3.13	-3.36
74.2	0.00	-2.49	-4.38
78.1	-0.99	-2.94	-5.86
82.0	-1.90	-3.05	-6.13
Mean loss at each grazing angle	1.70 ±0.66	3.57 ±1.73	4.19 ±1.18

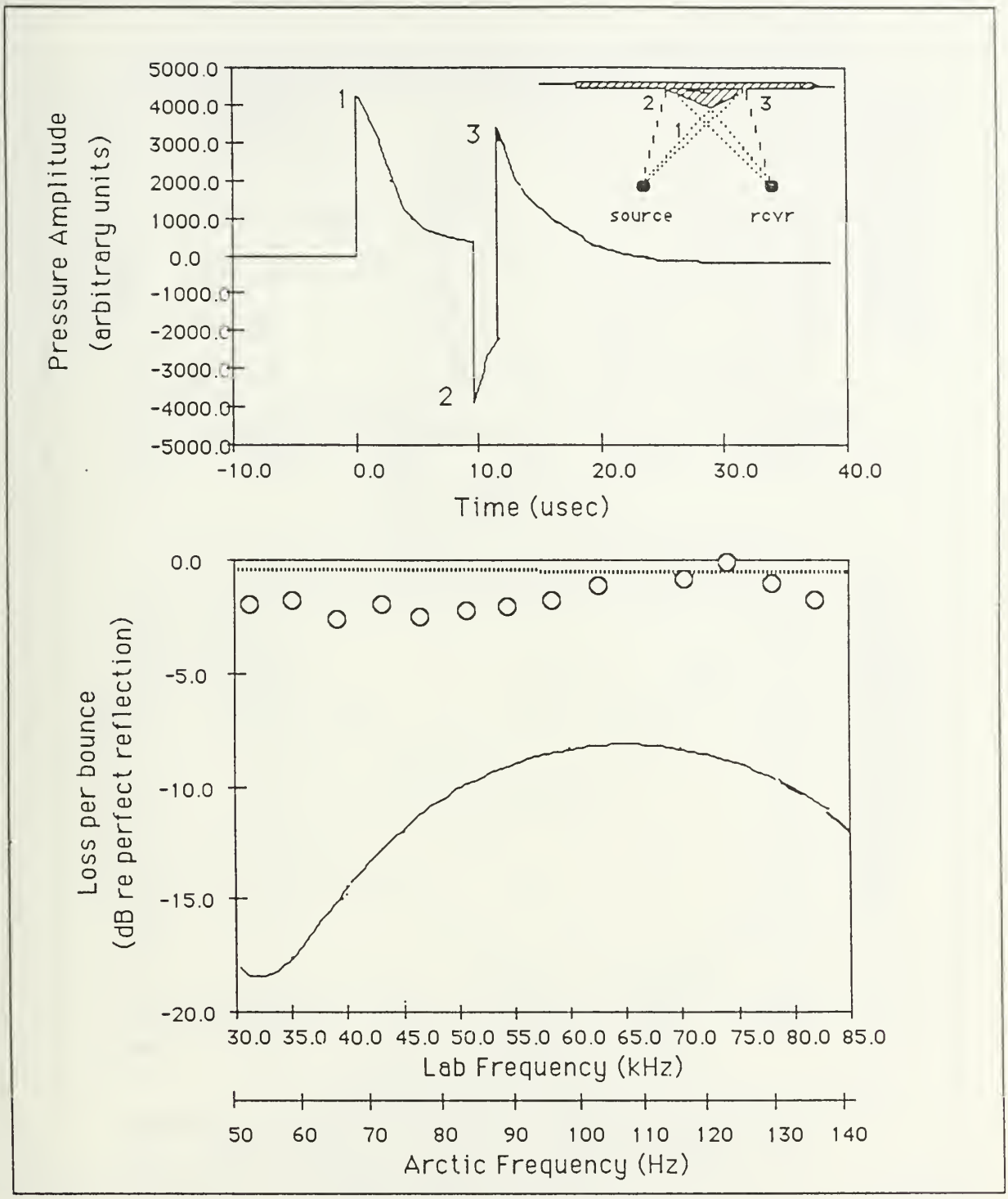

Figure 5.5, Temporal and spectral forward scatter from the laboratory wedge. Solid line is theoretical rigid wedge diffraction from the wedge keel. Dashed line is the theoretical combination of B-T diffraction and M&M reflection. Circles are experimental results. Grazing angle is 33 degrees.

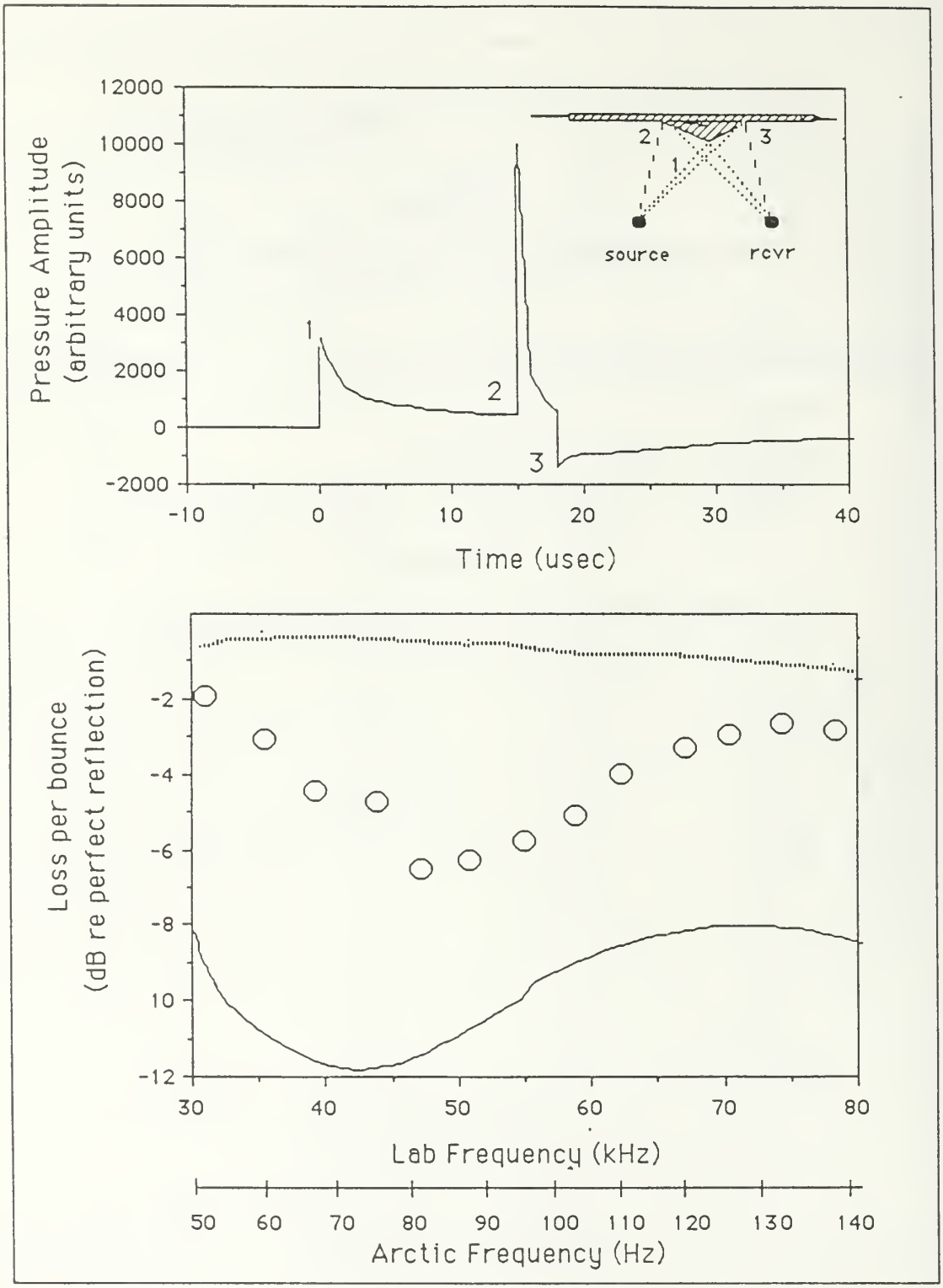

Figure 5.6. Temporal and spectral forward scatter from the laboratory wedge. Solid line is theoretical rigid wedge diffraction from the wedge keel. Dashed line is the theoretical combination of B-T diffraction and M&M reflection. Circles are experimental results. Grazing angle is 45 degrees.

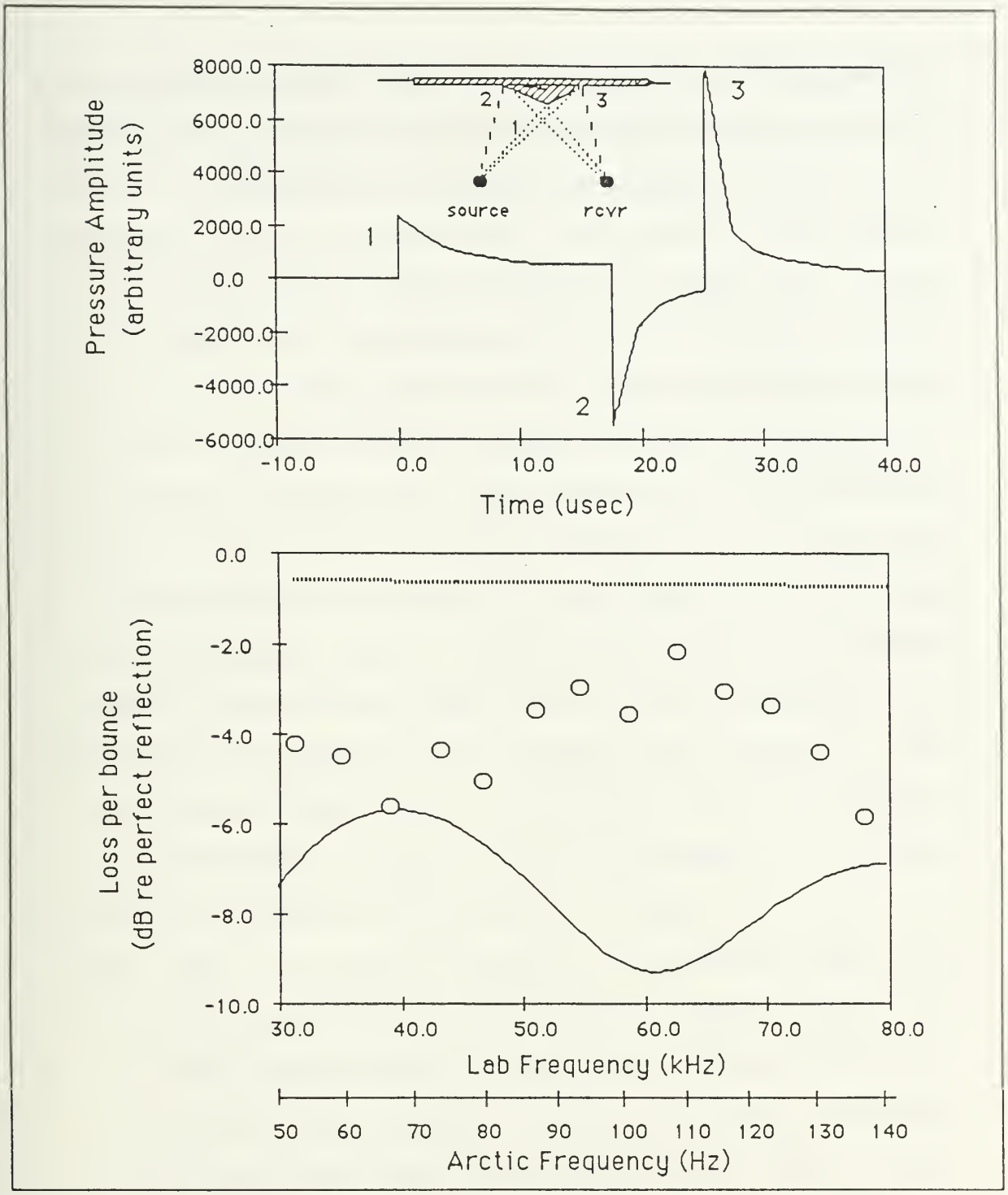

Figure 5.7. Temporal and spectral forward scatter from the laboratory wedge. Solid line is theoretical rigid wedge diffraction from the wedge keel. Dashed line is the theoretical combination of B-T diffraction and M&M reflection. Circles are experimental results. Grazing angle is 63 degrees.

considered here. The upper plot is a Biot-Tolstoy temporal description of the specularly scattered signal from a rigid wedge. The solid line on the lower plot shows the results of transforming the time data of the upper plot into the frequency domain. The dashed line near the top of the lower plot is a second theoretical curve which combines the Biot-Tolstoy predicted diffracted energy from the ridge keel and the McCammon and McDaniel predicted reflected energy off the ensonified area of the smooth plate, as explained in Chapter 4. The circles are our measured forward scattering results. These figures illustrate clearly that for this case of forward specular scatter from a single, finite wedge, the rigid wedge diffraction theory does not account for the total received acoustic energy. Also, a solution to the problem is not as simple as assuming the contribution of each component, i.e., the ridge keel and the smooth plate, depending on its percentage of ensonified area.

Analysis of Table V reveals that low frequency losses are only slightly dependent on frequency (within ± 1.7 dB). There is a steady decrease in attenuation as the grazing angle is decreased. The difference between diffraction theory and measured results narrows as the grazing angle increases, as expected, since the ridge keel fills a larger percentage of the ensonified area as the grazing angle increases.

One may summarize Figures 5.5 thru 5.7 by observing that the empirical results suggest that the loss per bounce at 50 to 140 Hz in the Arctic decreases from about 4 dB at larger

grazing angles to about 2 dB at a 33° grazing angle. Also, the Biot-Tolstoy rigid wedge theory combined with a weighted reflection coefficient does not explain the measured data.

VI. BACKSCATTER

A. PROCEDURE

Scattered acoustic energy that propagates in the opposite direction from the incident acoustic energy is termed backscatter. To measure backscatter requires both the source and receiver to lie along the line connecting the source, receiver, and scattering obstacle. An LC-10 transducer was used as the source to generate acoustic signals consisting of pulsed sinusoids. The propagating acoustic energy was scattered from one of the acrylic models described in Chapter III with the scattered acoustic energy measured by another LC-10 transducer located adjacent to the source transducer. Figure 6.1 shows the geometry used during the backscattering measurements. Typical measurements were made with the distance between the combination source/receiver and the scattering obstacle of 50 cm. However, at steep grazing angles (angles greater than 50°) interference from the surface reflected acoustic energy required increasing this distance to 1 m.

At the start of a new data run it was at times difficult to discern the backscattered signal from other scattering and reflections occurring in the tank. When this was the case, an aluminum sphere was positioned adjacent to the edge of interest and the resultant enlarged signal return was then used to isolate the signal of interest. Figure 6.2 is the time domain response from backscattering off the edge of an acrylic sheet.

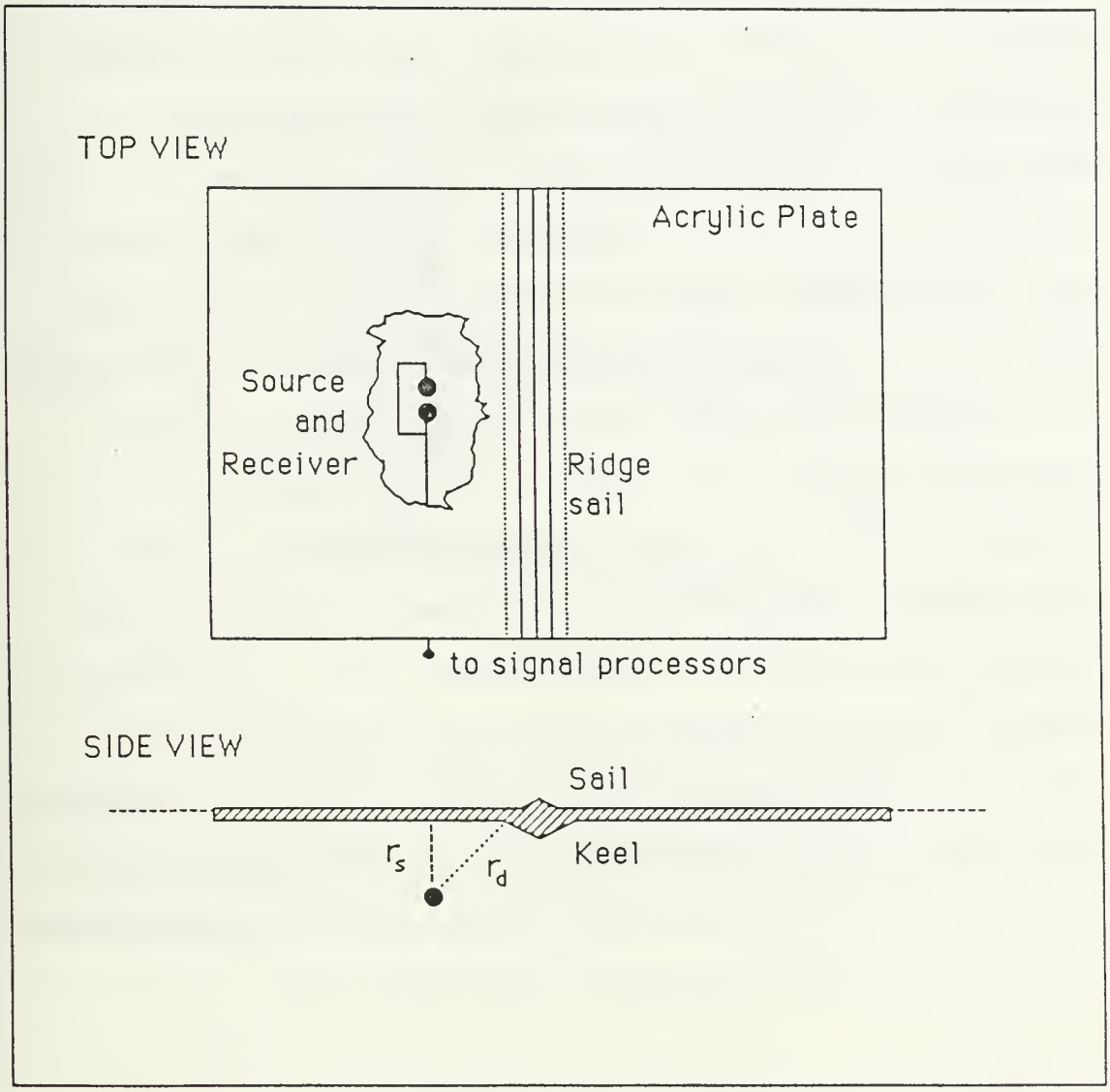

Figure 6.1: Location of source and receiver with respect to the acrylic plate and scattering surface for the backscatter measurements.

In the case of the open lead and ridge keel it was impossible to isolate the response from individual edges with the available equipment. In those cases the source pulse length was maintained at approximately 150 μs. This insured an 80 μs time window for the receiver in which the received signal was the sum of the diffracted signals from each of the individual edges. From this 80 μs window, 64 points were sampled at a frequency of 1 MHz and zero padded with 192 points to give sufficient frequency resolution after performing the discrete Fourier transform (DFT). The source frequencies selected in these measurements coincided with the bin frequencies from the DFT to minimize Gibb's effect (Clay and Medwin, 1977). The diffracted pressure from the sequence of edges was proportional to the magnitude of the response from the DFT. This was compared with the direct free field response over a fixed distance. For consistency, the same parameters were used for the backscatter measurements from the model of the rubble field.

B. RESULTS OF BACKSCATTER MEASUREMENTS

All backscattering results are reported in terms of the backscattering strength (BSS) as defined in Medwin and Novarini (1981, p. 111).

$$BSS = 10 \log_{10} [(I_{BS} R^{N+2})/(I_0 R_0{}^N A)] \qquad (6-1)$$

where N is the degree of geometrical divergence, $0 \leq N \leq 2$; I_{BS}

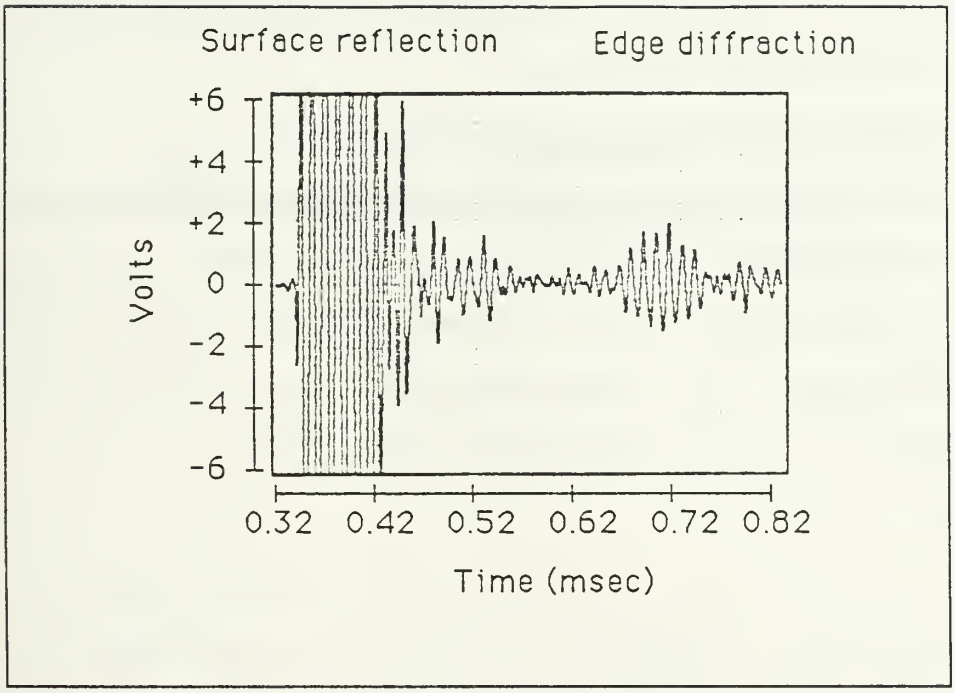

Figure 6.2: Time domain signal response for back-scattering off the lagging edge of an acrylic plate. Source and receiver are located 50 cm from the edge at a grazing angle of 30°.

is the acoustic intensity due to backscatter at the receiver; R is the distance between the scattering surface and the receiver, I_0 is the reference intensity at distance R_0; and A is the area from which the scattering is measured.

1. Spherical versus Cylindrical Divergence

Prior to calculating the BSS it was necessary to determine if the divergence of the acoustic energy from a particular feature occurred either spherically or cylindrically at the range of the BSS measurement. The result affects the value of the term, N, in Equation 6-1 and hence the value of the backscattering strength.

If the scattering occurs from a linear feature such as a lead or the keel of a pressure ridge, the divergence will be cylindrical if the pressure is measured close to the line scatterer and N will take on the value of 1. On the other hand, a randomly rough surface, containing individual point scatterers will result in spherical divergence, and N would take on the value of 2.

Measurements were taken using the ridge model as the scattering feature with the source and receiver positioned as shown in Figure 6.3. The position of the source and the scattering angle to the receiver were kept constant while the receiver was moved to vary the range from the scattering surface. Hence, the pressure response of the receiver depends only on the range from the scattering surface to the receiver, i.e.,

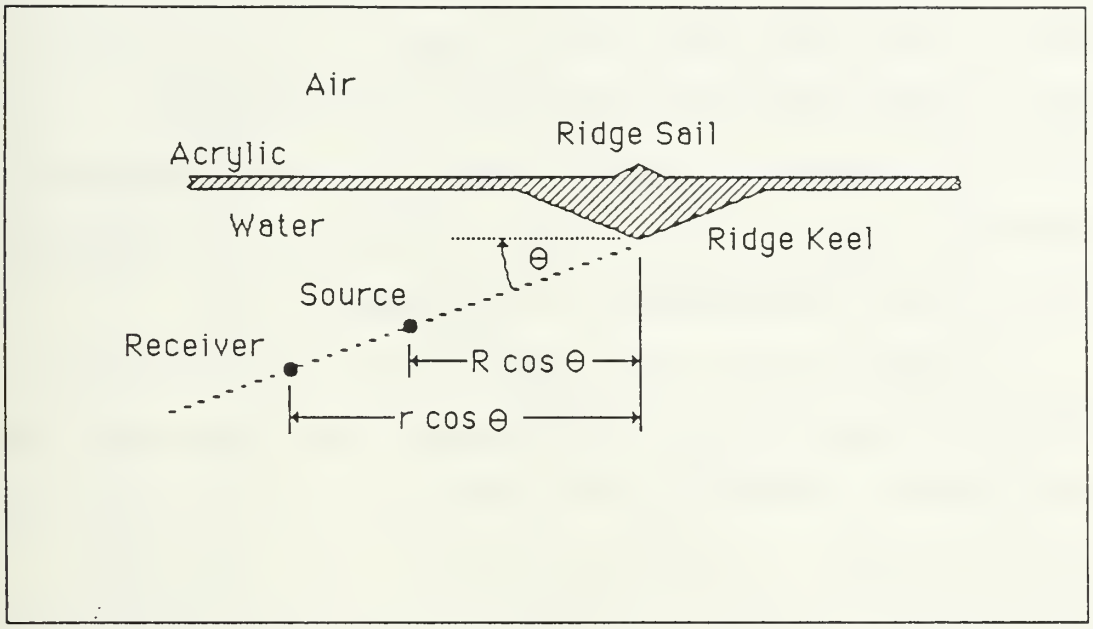

Figure 6.3: Geometry used in determining geometric divergence from a linear scattering element. R and θ were held constant at 0.5 m and 40° respectively, while r was varied. Dimensions of the ridge keel are as given in Figure 3.1.

$$P \propto \frac{1}{R} \frac{1}{r^n}$$

where R is the range from source to ridge, r is the range from ridge to receiver and n represents the type of divergence, i.e., n is 1 if the divergence is spherical and n is ½ if the divergence is cylindrical. Figure 6.4 shows a plot of log P vs log r with lines of slope ½ and 1 superimposed on the measured data.

This figure clearly shows that, at the ranges used in the backscatter measurements, the divergence due to scattering from linear features is spherical, vice cylindrical as would be expected at shorter ranges. As described in Section IV.A, the impulse diffraction from a wedge is maximum at the point at which the least time path intersects the wedge; the contribution to the diffracted energy from points along the wedge on either side of the least time point decreases exponentially with distance from the least time point. Therefore, only a finite portion of the wedge effectively contributes to the diffracted energy which reaches the receiver.

Using spherical divergence and converting intensities to pressures, Equation 6-1 becomes:

$$BSS = 20 \log_{10} [P_{BS} R^2 / \{P_o R_o (A)^{1/2}\}]. \qquad (6\text{-}2)$$

For the measured data, P_o was determined from the direct free field response of the receiver located at R_o = 1, or 2 m. The

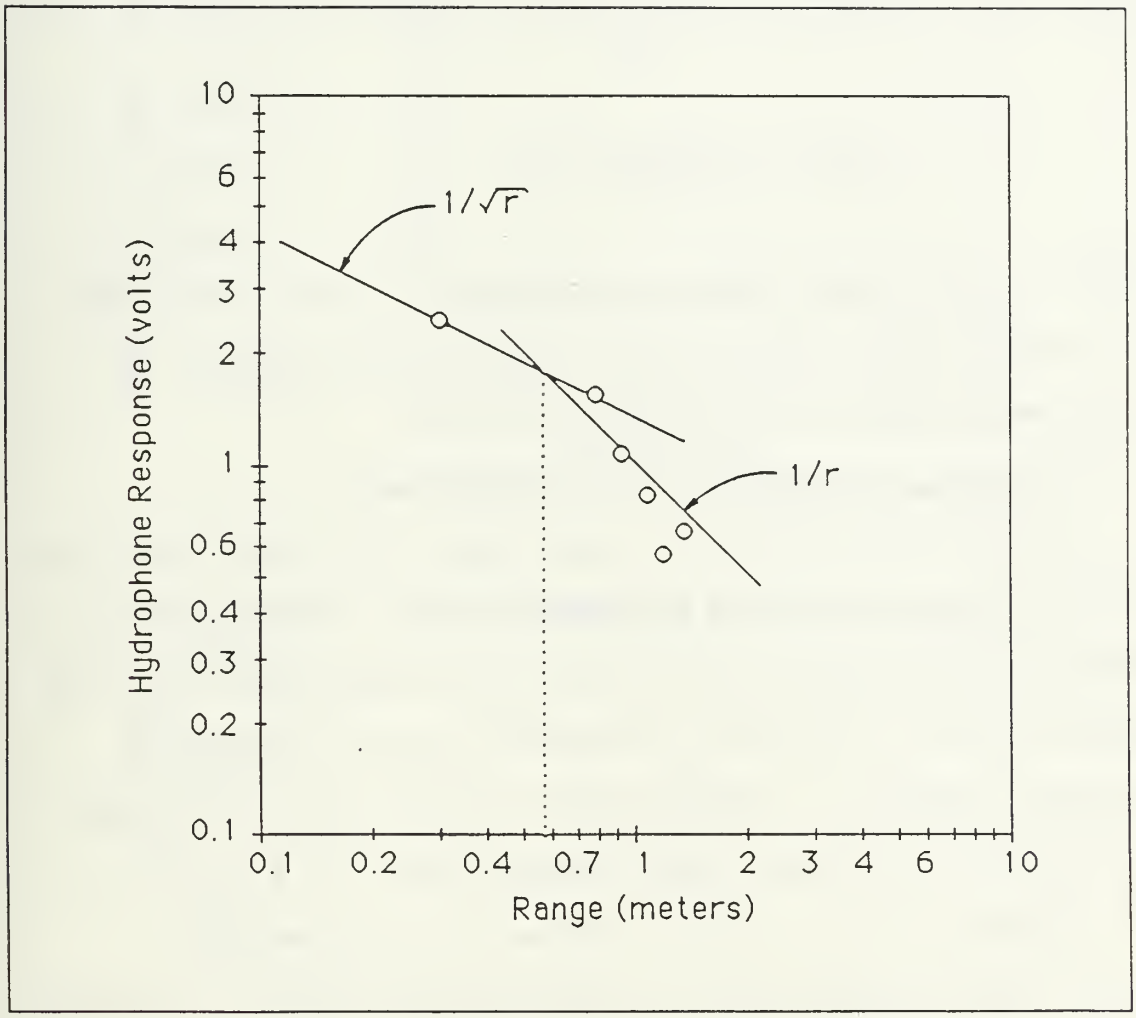

Figure 6.4: Results of the measurements using the geometry shown in Figure 6.3, where the range is r. Data indicates that the geometrical divergence is cylindrical ($\propto 1/\sqrt{r}$) at short range and spherical ($\propto 1/r$) at longer ranges.

term A was taken as the entire area ensonified during the 64 μs sampling period for the DFT. This was calcuated from information available in the averaged time domain response, that is

$$\sqrt{A} = \frac{c}{2}\sqrt{\pi T(2t_o + T)}$$

where c is the sound speed in the water, T is the record length for the DFT and t_o is the elapsed time between triggering the source and the start of sampling for the DFT.

2. Results of Backscatter from Simple Edges

Simple edges consist of a single edge of an acrylic plate and can be divided into leading and lagging edges. A leading edge is defined when the source and receiver are located away from the plate, and $90° \leq \theta \leq 180°$ as measured from the horizontal ice-water interface. A lagging edge is defined when the source and receiver are located under the plate, and $0 \leq \theta \leq 90°$.

Figures 6.5, 6.6, and 6.7 show the experimentally observed BSS plotted along with the theoretical BSS due to simple rigid wedge Biot-Tolstoy diffraction from the submerged leading edge. The time domain plot in these figures is the superposition of Equation 4-1 applied to diffraction from the submerged edge, diffraction from the submerged edge followed by reflection off the water-air interface, reflection off the water-air interface followed by diffraction from the edge, and reflection followed by diffraction followed by reflection. This gives three separate impulse

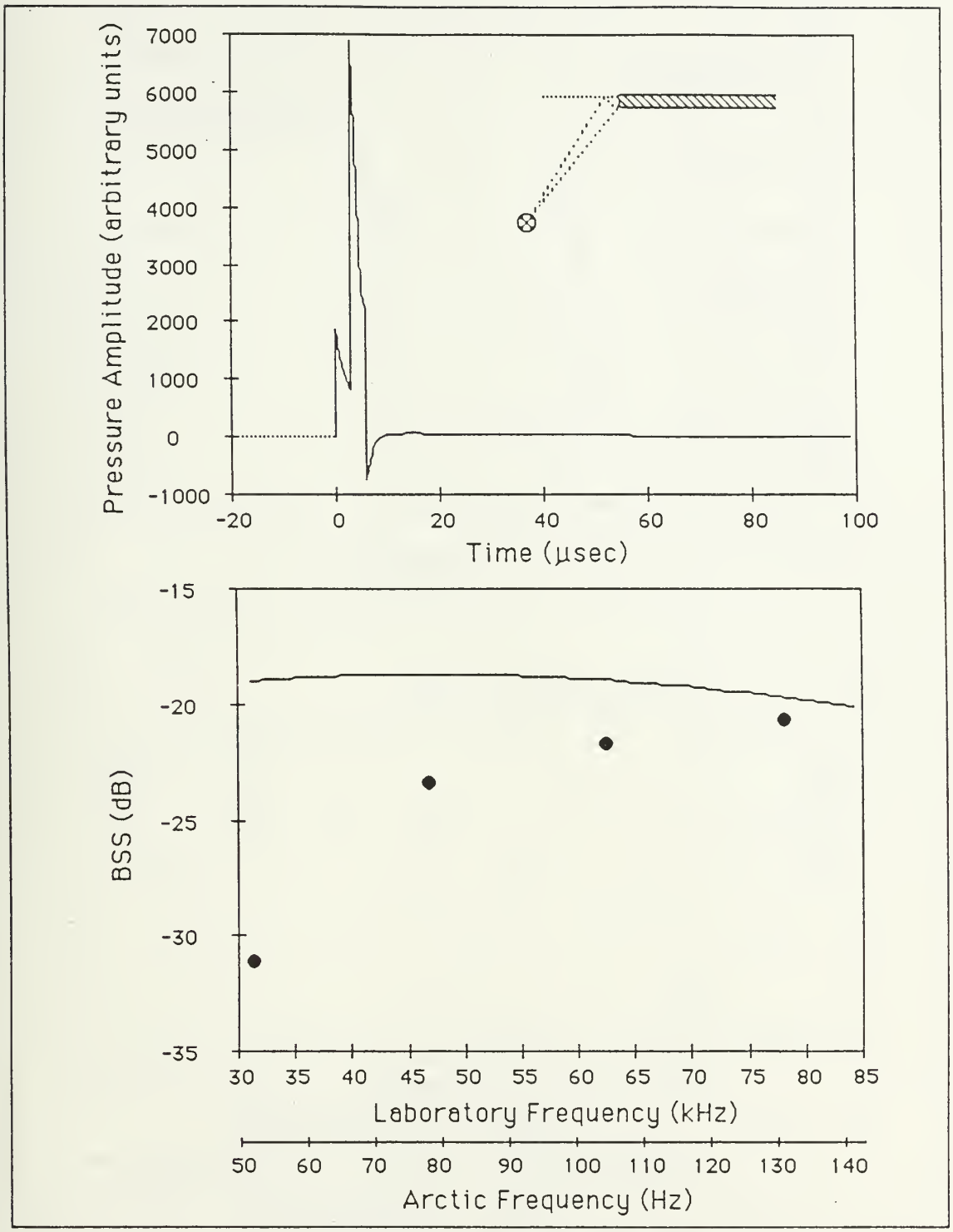

Figure 6.5: Temporal and spectral backscatter from the leading edge of the acrylic plate. Solid line is theoretical rigid wedge diffraction from the submerged edge and its surface reflection. The circles are the experimental data. Grazing angle is 30°.

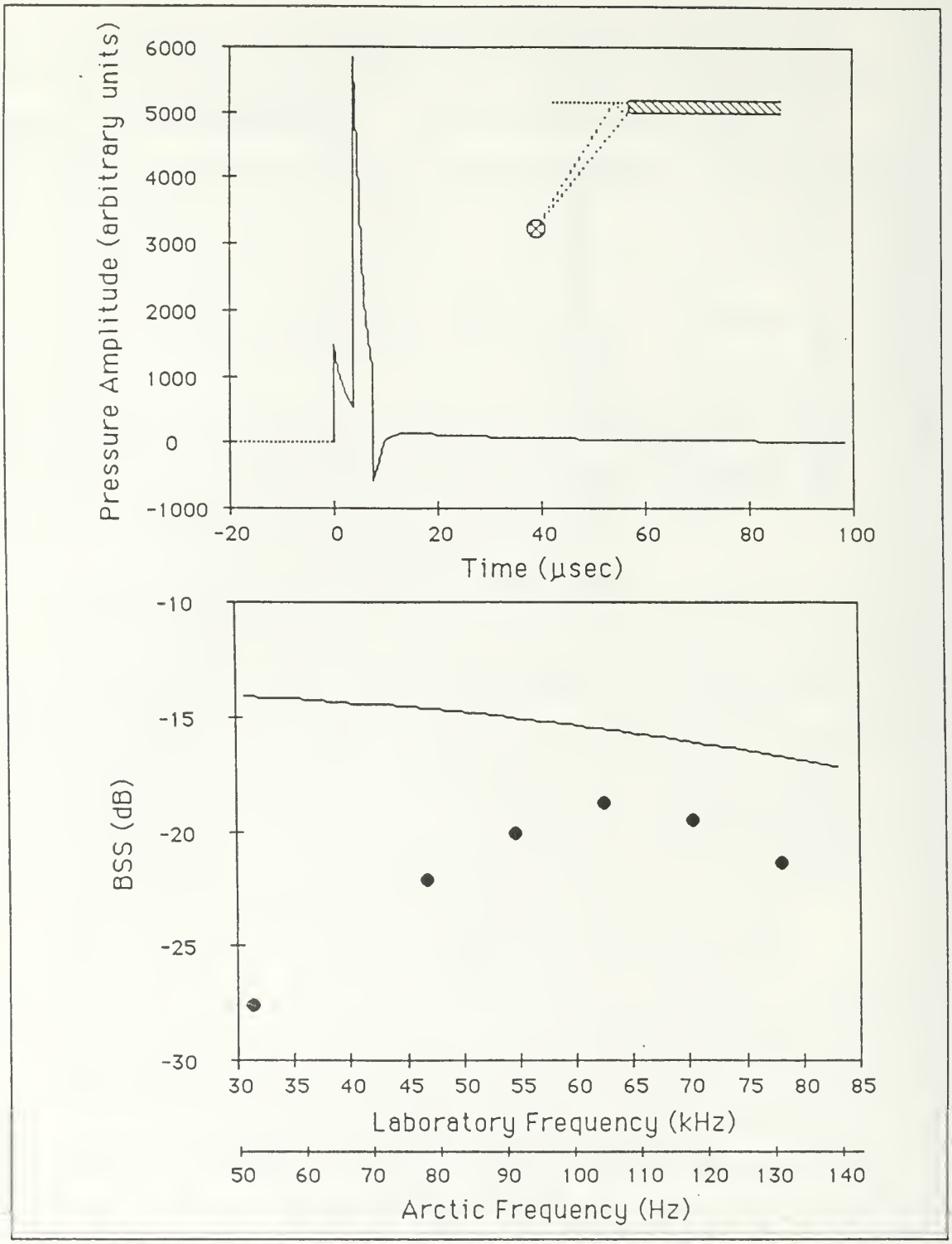

Figure 6.6 Temporal and spectral backscatter from the leading edge of the acrylic plate. Solid line is theoretical rigid wedge diffraction from the submerged edge and its surface reflection. The circles are the experimental data. Grazing angle is 45°.

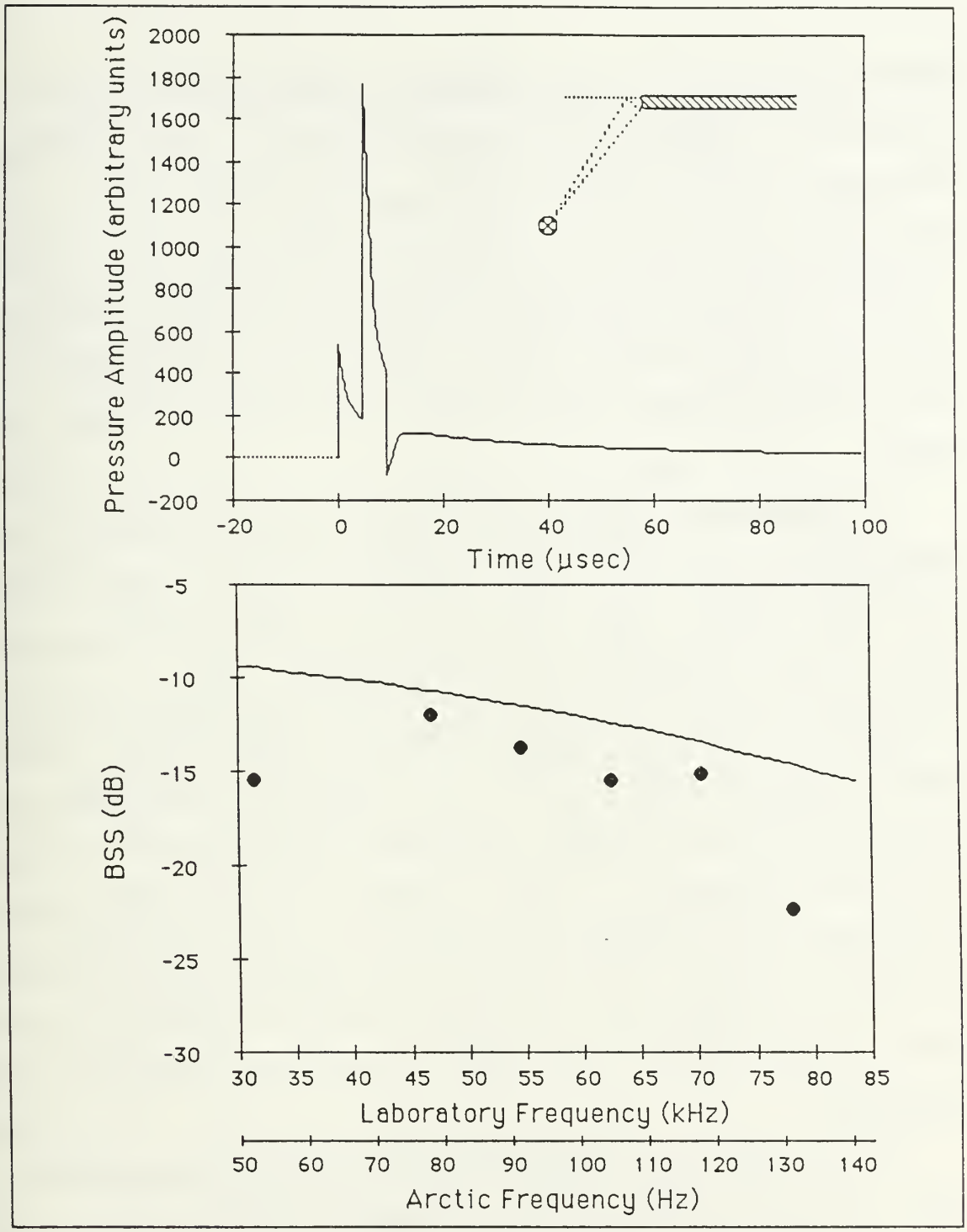

Figure 6.7: Temporal and spectral backscatter from the leading edge of the acrylic plate. Solid line is theoretical rigid wedge diffraction from the submerged edge and its surface reflection. The circles are the experimental data. Grazing angle is 60°.

responses instead of four since Equation 4-1 gives identical results for diffraction-reflection and reflection-diffraction. The frequency domain plot compares the information in the computed time domain plot transformed to the frequency domain (by DFT) with the measured BSS. The sampling period for the DFT was chosen to give an integral number of bins (where one sampling period is a bin) between the least time arrivals from multiple or image wedges.

For frequencies less than 50 kHz (83 Hz in the arctic) the overestimation of the BSS by Biot-Tolstoy diffraction is due to the finite size of the plate edge, which at 8 mm is less than one quarter of the wavelength of the incident wave. Any discrepencies between the measured and theoretical data at frequencies greater than 50 kHz can be accounted for by mode conversion in the acrylic plate. Specular reflection does not contribute to backscatter. That is, some of the energy that would have been diffracted if the plate were rigid is converted into shear or flexural waves in the plate or refracted into the plate as a compressional wave; that energy does not appear in backscatter.

In the case of the lagging edge, there will not be an image source. However, there will be some double diffraction, that is, diffraction around the edge with reflection from the water-air surface, followed by diffraction around the same edge in the direction of the receiver. This effect is expected to be small (Medwin et al, 1982) and will not be considered in this analysis.

Figure 6.8 shows the experimental backscatter from a lagging edge along with the predicted backscatter due to diffraction from the single visible edge. Only in the case of 15° grazing angle is there remote agreement between backscatter due to diffraction and the experimentally measured backscatter. At the other angles there is significant backscatter from the edge that is not accounted for by rigid wedge diffraction alone. Possible mechanisms for this additional backscatter could be: a) mode conversion of the incident acoustic energy into shear and flexural modes in the acrylic plate which are re-radiated into the water and b) compressional waves, internally refracting and reflecting in the acrylic plate and then re-radiating into the water. The discrepency is largest at grazing angles of 40 to 60° and is virtually non-existent at 15°. This behavior supports hypothesis b) above because the compressional wave in the acrylic plate approaches coincidence at the larger angles of incidence, while the shear and flexural modes in acrylic do not achieve coincidence with the waterborne compressional wave. Even though coincidence is not achieved for the flexural and shear modes, some energy will be lost to these modes in the plate due to evanescent mode formation. This would account for the observed values of BSS that are less than those calculated for rigid boundary diffraction at the 15° grazing angle.

3. Results from an Open Lead

Backscatter measurements were taken from a simulated open lead with three separation distances and two grazing angles.

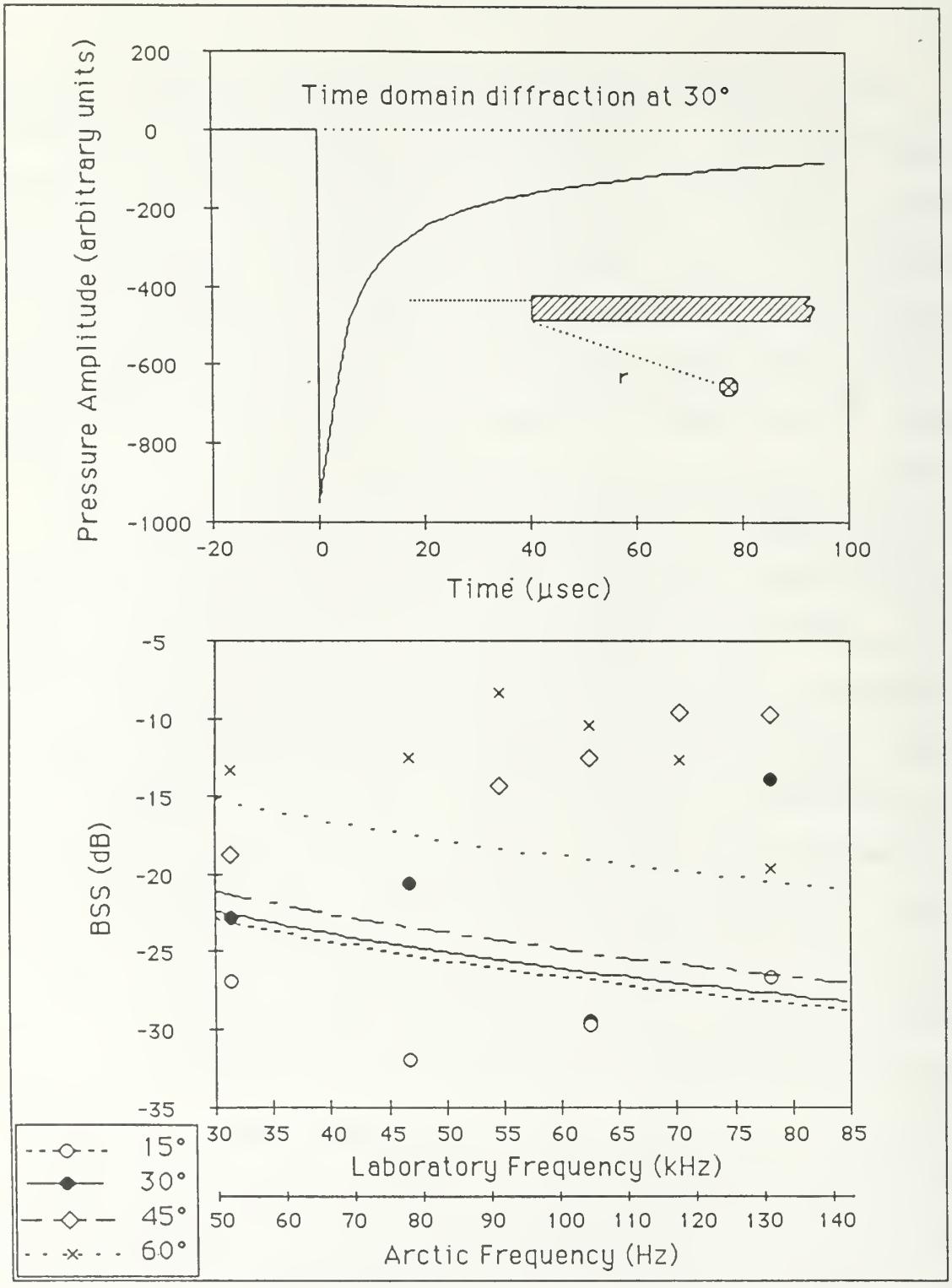

Figure 6.8: Temporal and spectral backscatter from a lagging edge of the acrylic plate. Lines are theoretical backscatter from a single edge at grazing angles of 15, 30, 45, and 60°. Points are the experimental data.

The lead was simulated by placing two acrylic sheets in the test tank and separating them by a fixed distance with the use of two balsa spacers. The separation distances used were 1, 2, and 3 cm which correspond to Arctic dimensions of 6, 12, and 18 m, respectively. The two angles selected were a shallow grazing angle of approximately 15° and a steeper grazing angle of approximately 40°. The results of the measurements are shown in Figures 6.9 thru 6.14.

Two fundamental concepts were used in evaluating this information: a) comparison with diffraction theory for diffraction from any visible edges and the water surface reflection of the diffracted energy, and b) comparison with diffraction theory plus the effect of multiple reflections in the water space between the plates. The effect of the multiple reflections was evaluated as diffraction of the incident impulse energy into the space between the plates where it is multiply reflected between the plates. To estimate the magnitude of this contribution, 50 percent of the remaining energy between the plates was assumed to be re-radiated back into the water to the receiver at discrete time intervals corresponding to the width of the plate separation. These were incorporated into the theoretical time domain response for diffraction as finite impulses whose magnitude included the effect of the initial diffraction and the effect of 50 percent leakage from the lead.

The effect of diffraction from rigid edges alone is shown in the figures as the solid curves. The dashed curves include the

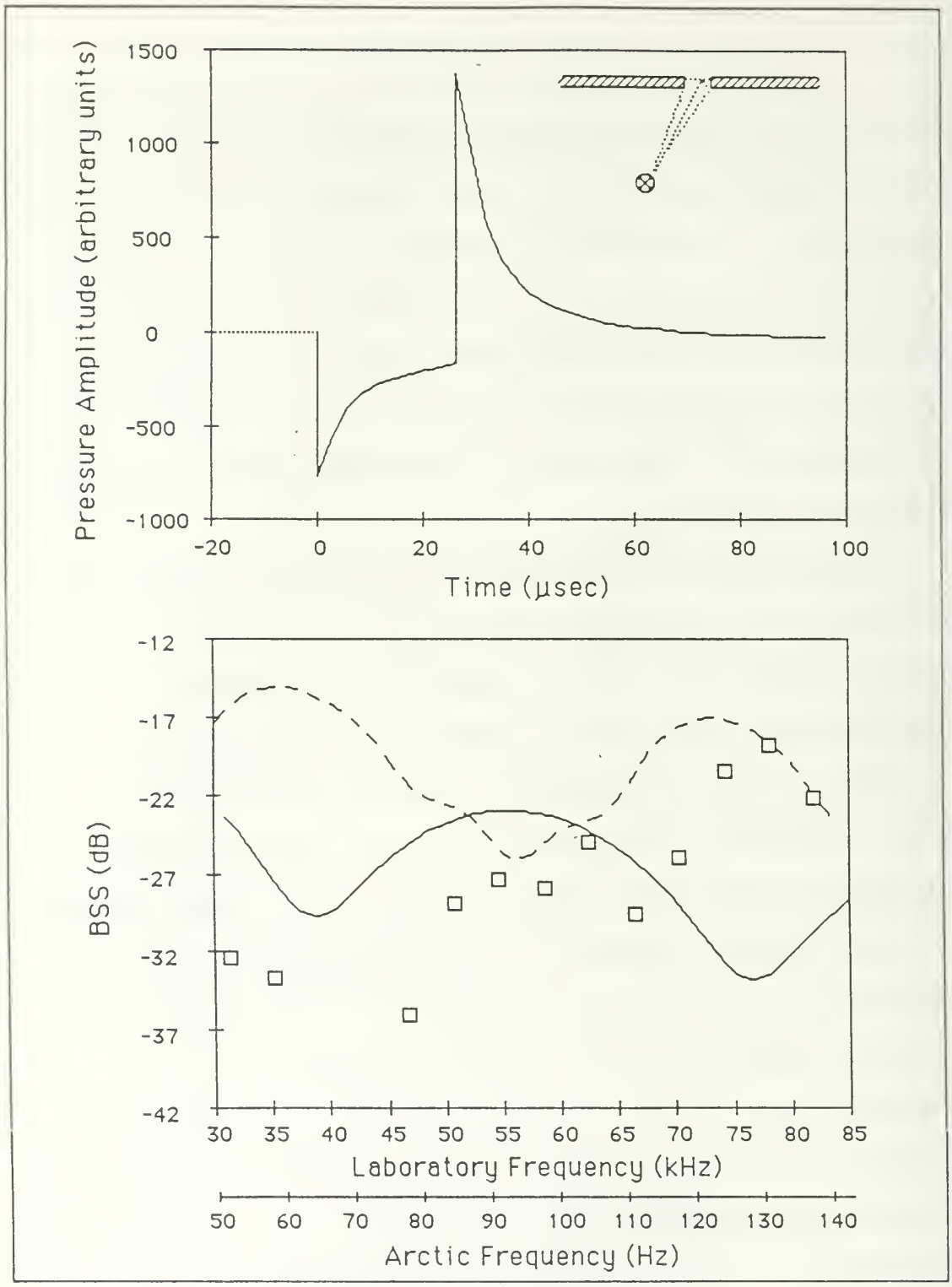

Figure 6.9: Temporal and spectral backscatter from an open lead with width 2 cm (12 m in the Arctic). Solid line from diffraction theory for two visible edges and one surface reflection. Dashed line is diffraction theory plus the effect of multiple reflections in the lead. Points are measured values. Grazing angle is 15°.

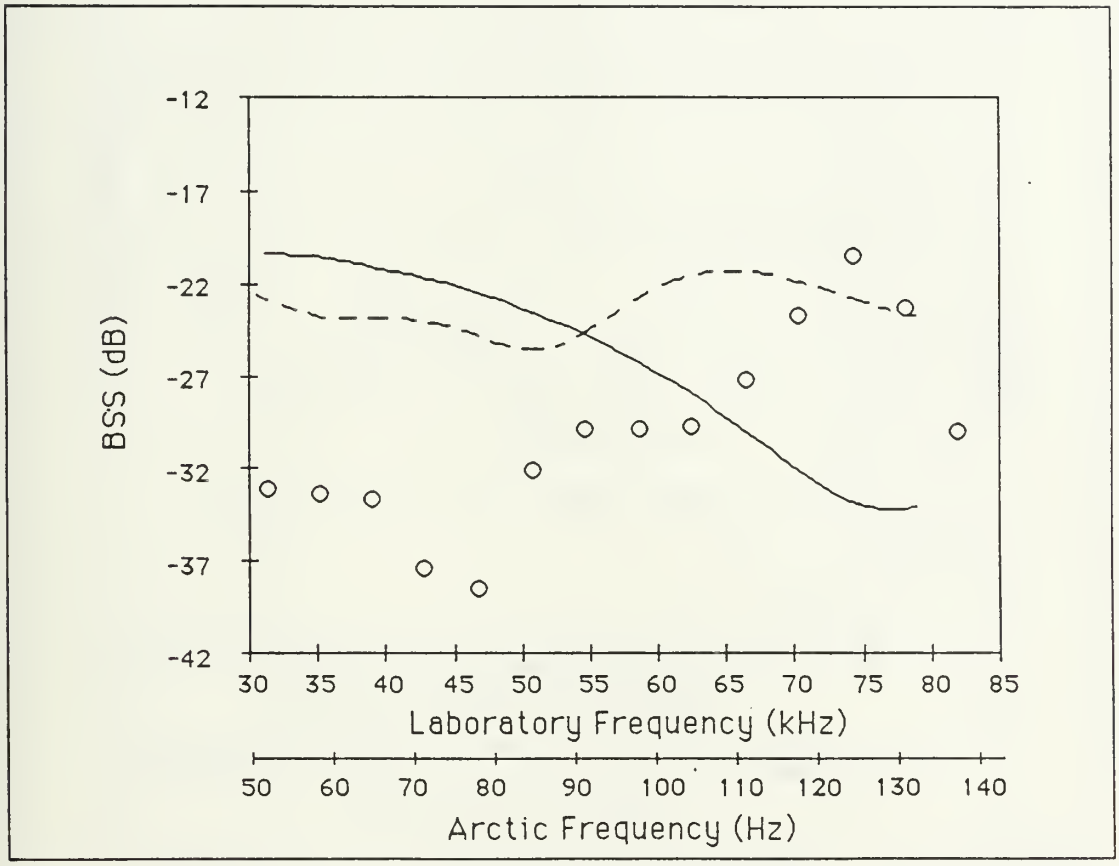

Figure 6.10: Spectral backscatter from an open lead with width 1 cm (6 m in the Arctic). Solid line from diffraction theory for two visible edges and one surface reflection. Dashed line is diffraction theory plus the effect of multiple reflections in the lead. Points are measured values. Grazing angle is 15°.

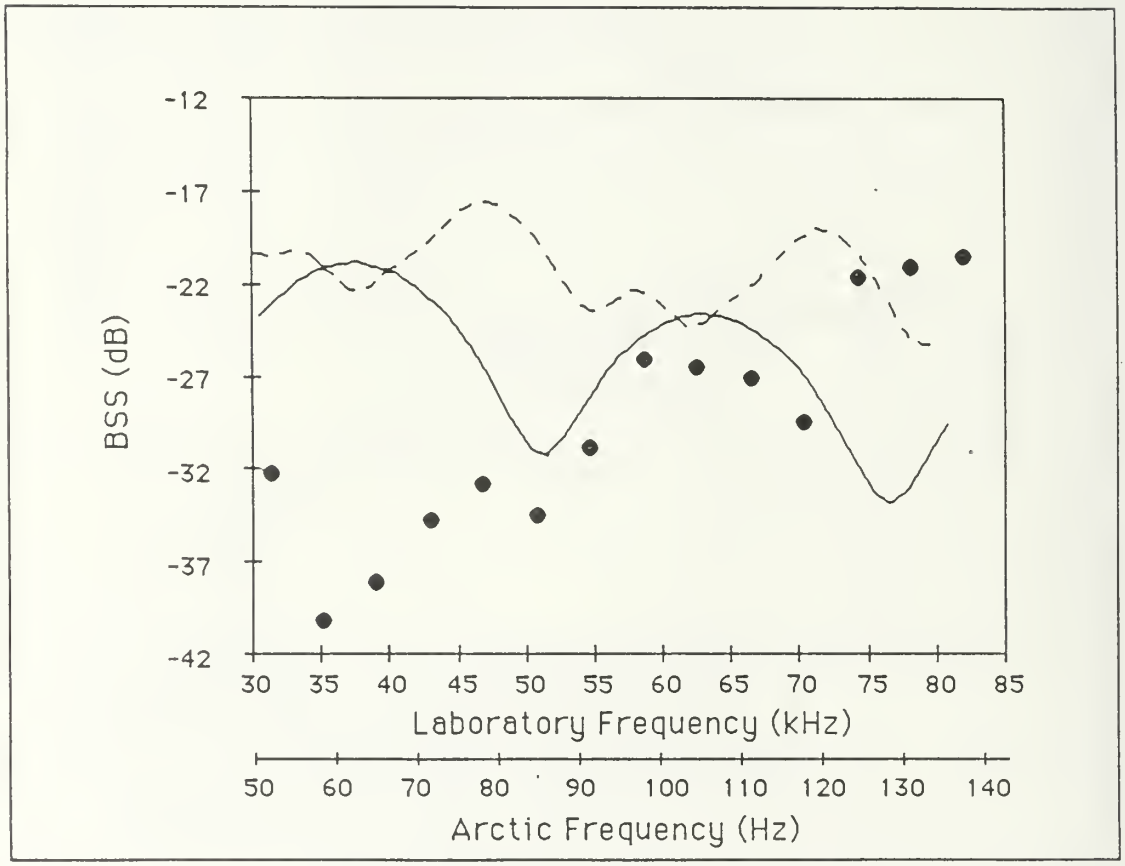

Figure 6.11: Spectral backscatter from an open lead with width 3 cm (18 m in the Arctic). Solid line from diffraction theory for two visible edges and the surface reflection. Dashed line is diffraction theory plus the effect of multiple reflections in the lead. Points are measured values. Grazing angle is 15°.

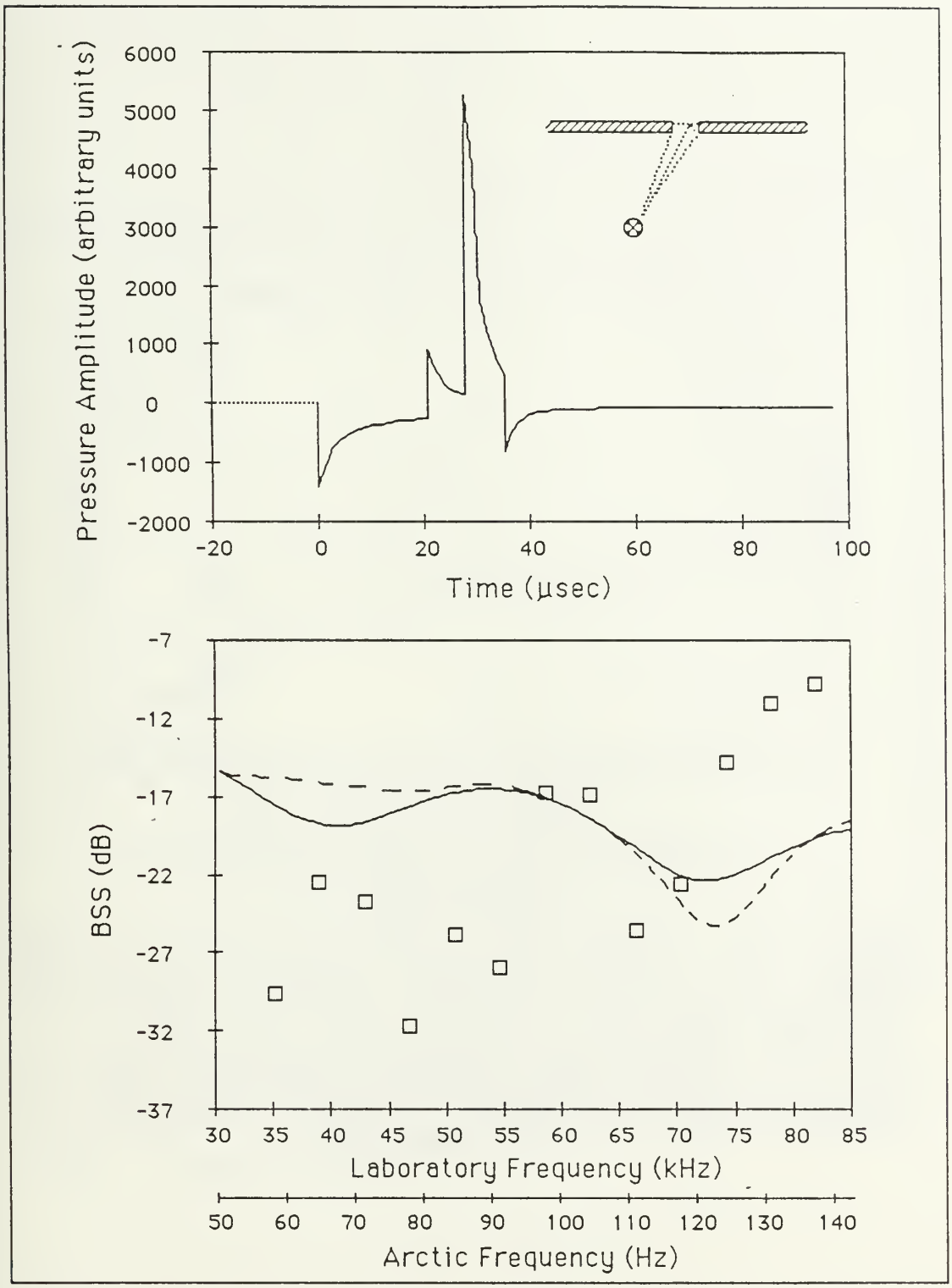

Figure 6.12: Temporal and spectral backscatter from an open lead with width 2 cm (12 m in the Arctic). Solid line from diffraction theory for two visible edges and surface reflection. Dashed line is diffraction theory plus the effect of multiple reflections in the lead. Points are measured values. Grazing angle is 41°.

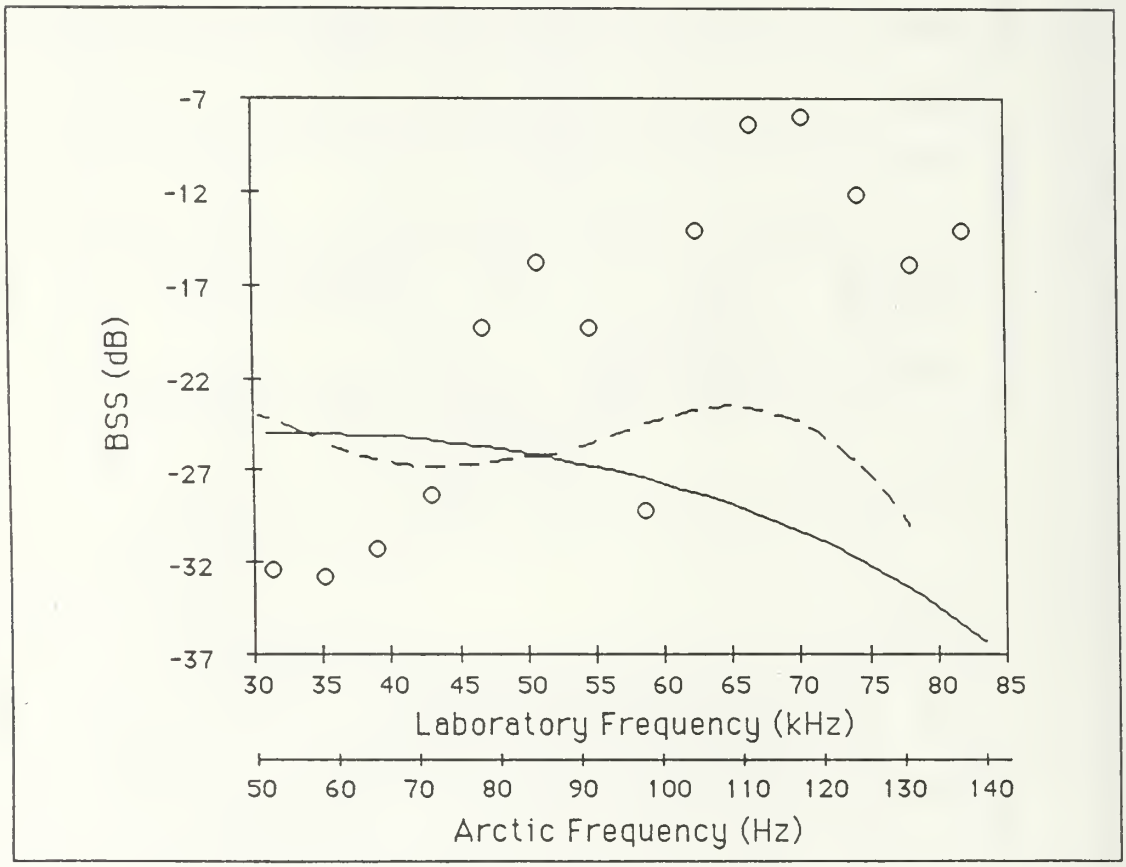

Figure 6.13: Spectral backscatter from an open lead with width 1 cm (6 m in the Arctic). Solid line is from diffraction theory for two visible edges and surface reflection. Dashed line is diffraction theory plus the effect of multiple reflections in the lead. Points are measured values. Grazing angle is 41°.

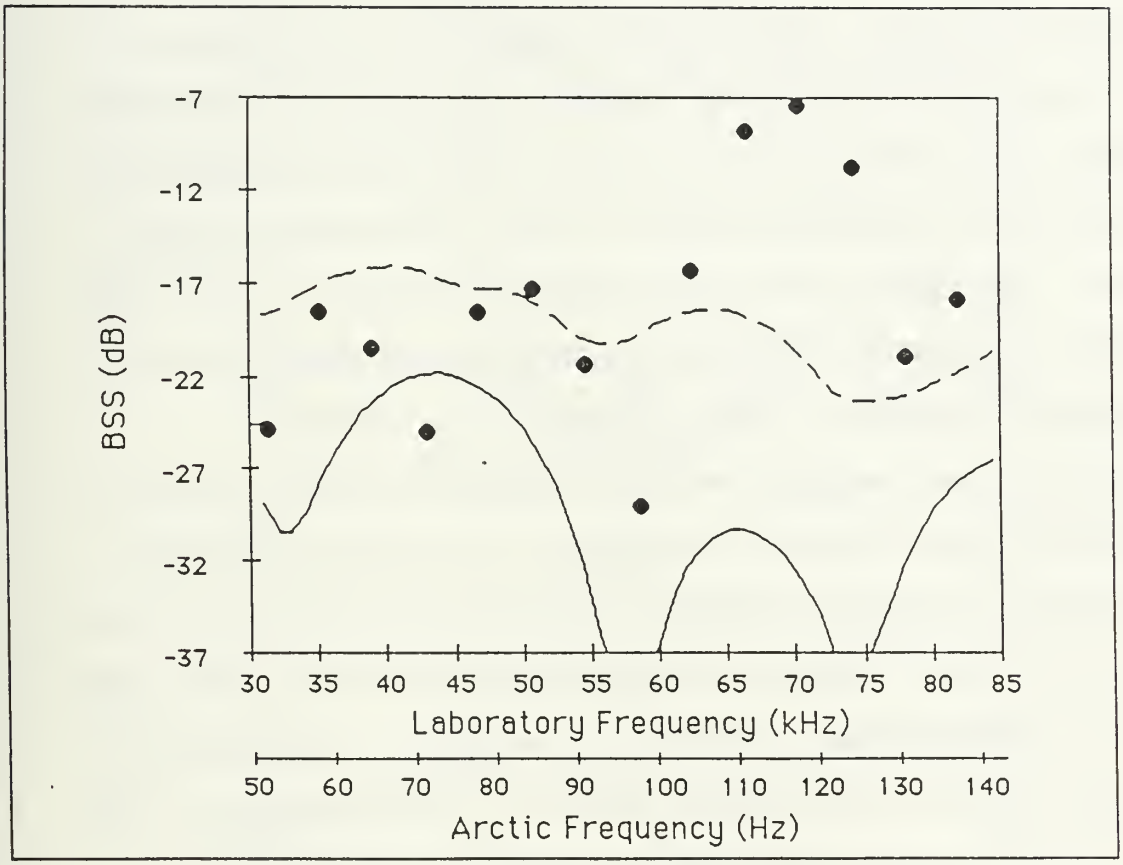

Figure 6.14: Spectral backscatter from an open lead with width 3 cm (18 m in the Arctic). Solid line is from diffraction theory for two visible edges and surface reflection. Dashed line is diffraction theory plus the effect of multiple reflections in the lead. Points are measured values. Grazing angle is 41°.

effect of multiple reflections in addition to diffraction. In computing the dashed curves a total of six reflections were considered. These results are consistent with those observed for the simple edges. Extending the results from simple edges at 15° grazing angle it is expected that BSS from both the leading and lagging edges that make up the lead will be predominantly from diffraction of the exposed edges. Due to the shallow grazing angle, coincidence with plate compressional modes which could result in enhanced BSS (from refraction and reflection) is not expected. However, mode conversion to evanescent compressional, flexural, and shear modes will occur resulting in reduced values of BSS. In addition, at the lower frequencies (<50 kHz) the observed BSS will be attenuated due to the finite size of the plate edge as discussed in the section on simple edges. At 41° grazing angle, conversion of waterborne compressional waves to plate compressional modes for the lagging edge of the lead with resulting refraction and reflection dominates the observed values of BSS.

4. Results from a Ridge Keel

Measurements of backscattering strength from a ridge keel were conducted in the same manner as those for the open lead. The same frequencies and approximate grazing angles were used so that a comparison between backscatter from the open lead and the ridge keel could be made. The results of the laboratory measurements and the analysis of the theoretical diffraction from a rigid wedge are given in Figures 6.15 through 6.18.

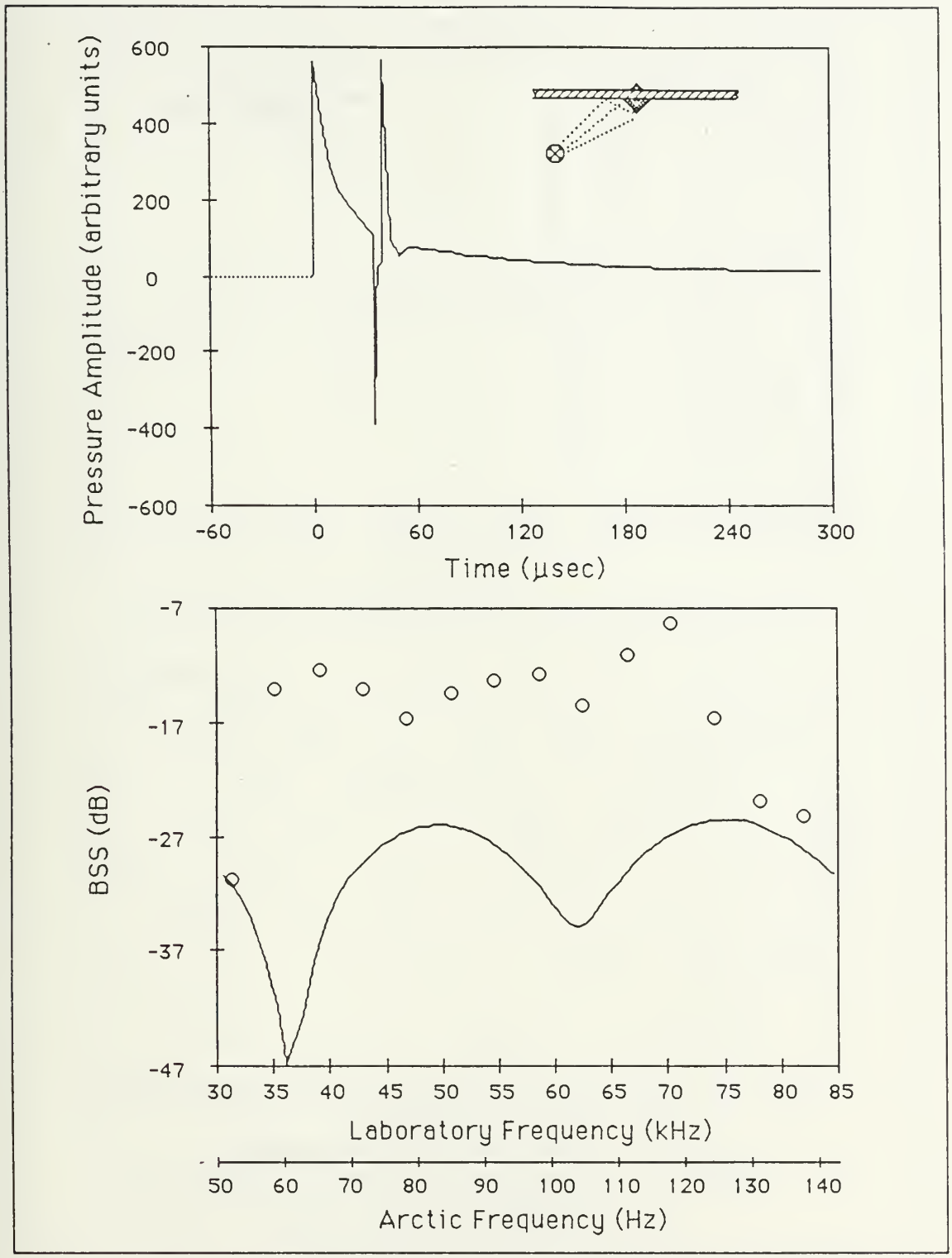

Figure 6.15: Temporal and spectral backscatter from the model of the ridge keel. The circles are measured backscattering strength, lines are the calculated BSS using Biot-Tolstoy diffraction theory. The grazing angle is 15°.

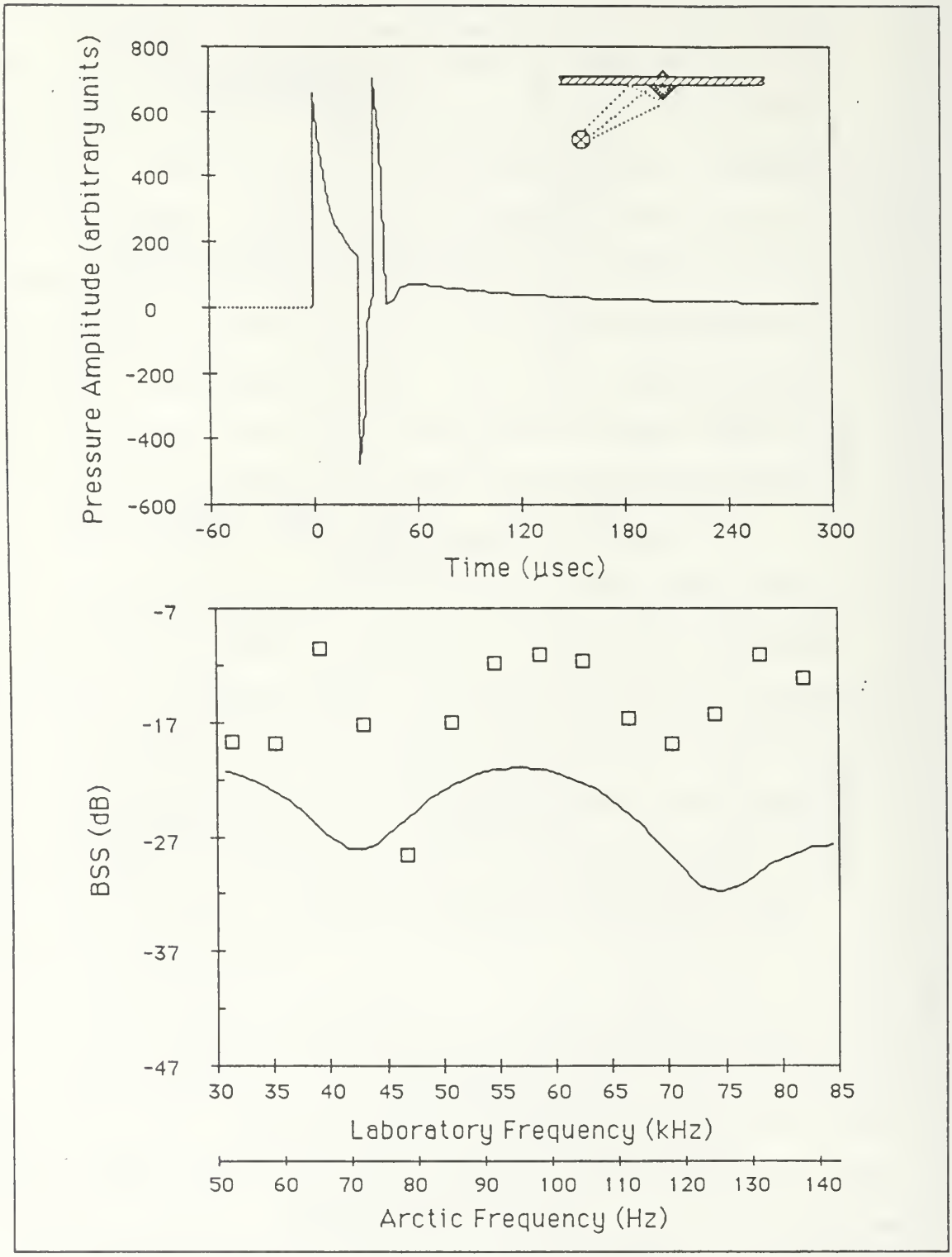

Figure 6.16: Temporal and spectral backscatter from the model of a ridge keel. The squares are measured backscattering strength, lines are the calculated BSS using Biot-Tolstoy diffraction theory. The grazing angle is 29°.

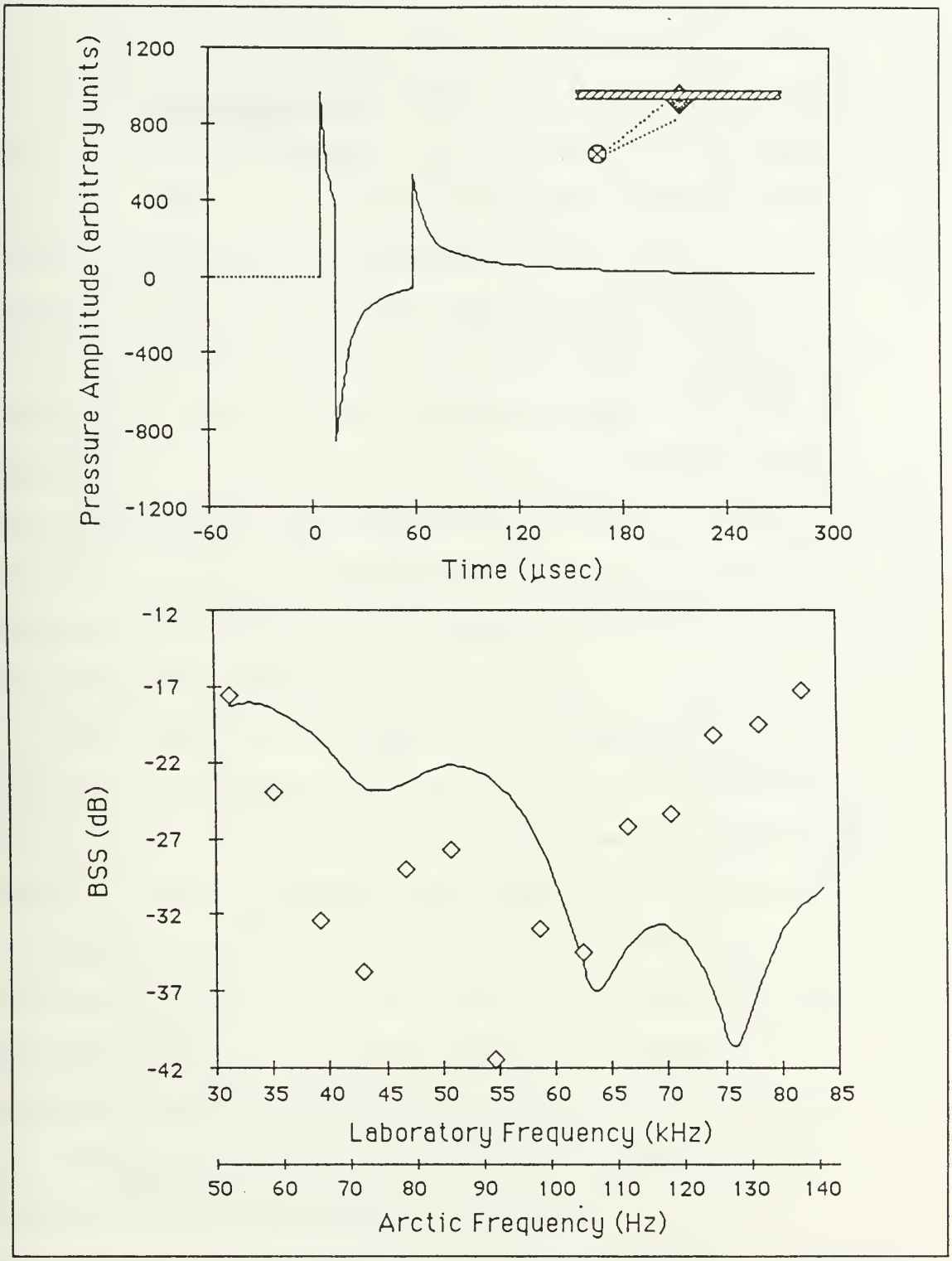

Figure 6.17: Temporal and spectral backscatter from the model of a ridge keel. The diamonds are measured backscattering strength, lines are the calculated BSS using Biot-Tolstoy diffraction theory. The grazing angle is 47°.

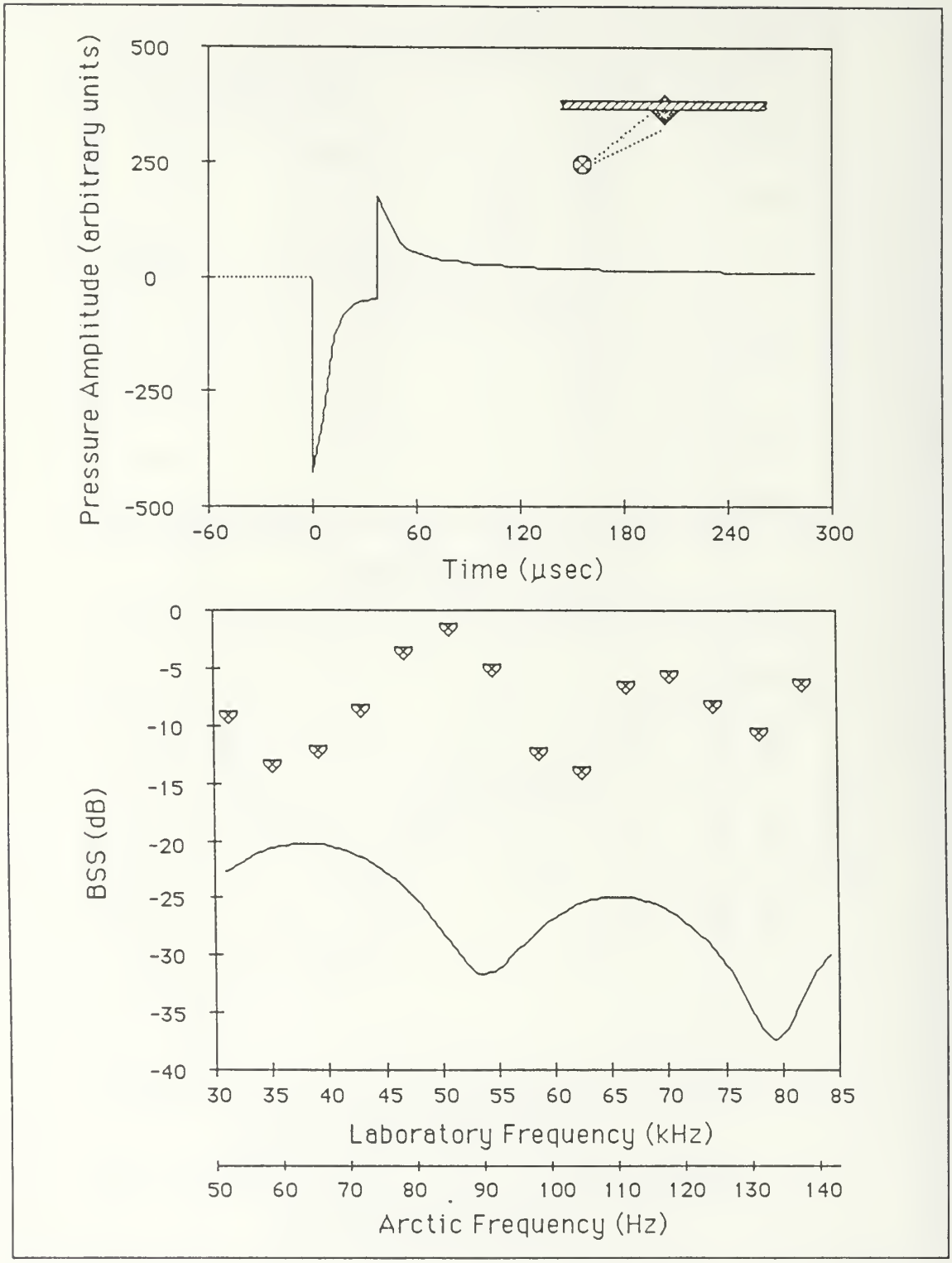

Figure 6.18: Temporal and spectral backscatter from the model of a ridge keel. The symbols are measured backscattering strength, lines are the calculated BSS using Biot-Tolstoy diffraction theory. The grazing angle is 63°.

At the shallow grazing angle of 15°, there is significantly more (10 dB more) BSS than can be accounted for by diffraction from rigid wedges. Due to the shape of the ridge keel, incident acoustic energy at the front edge of the ridge will be at a grazing angle of 42° (15° + 27°), which is approaching coincidence for compressional waves in the acrylic with respect to compressional waves in the water. These compressional waves can then be reflected and diffracted in the acrylic and re-radiated into the water resulting in the large BSS values observed. This same explanation also can account for the difference between theory and observation at 29° grazing angle (i.e. 56° grazing angle along front edge of the ridge keel).

The results at 47° grazing angle appear inconsistent with the results so far discussed. That is, if the observed BSS is dominated by compressional mode coincidence, then this should be the case for all frequencies since compressional waves are non-dispersive. Another effect that has not been discussed is for resonances to appear in the ridge keel. The dimensions of the ridge keel model are such that, depending on boundary conditions, the first resonance can occur at frequencies around 10 kHz. Therefore the observed BSS can be affected by the resonances in the ridge keel and this can account for the fluctuations in the observed BSS. The appearance of resonances in the ridge keel model requires that the compressional wave energy be converted to compressional modes in the acrylic, since re-radiated flexural and shear modes are evanescent.

TABLE VI

BACKSCATTER FROM THE ACRYLIC RUBBLE FIELD

	Grazing Angle (degrees)			
	20	40	60	90
Freq (kHz)	Backscattering Strength (dB)			
31.3	-18.6	-20.4	-10.0	1.5
35.2	-22.3	-19.8	-15.2	-3.4
39.1	-12.1	-21.2	-7.9	-2.0
43.0	-14.5	-13.6	-19.0	-3.6
46.9	-3.6	-12.1	-9.8	-8.5
50.8	-5.7	-19.3	-9.7	-10.0
54.7	-8.3	-9.0	-13.8	-5.6
58.6	-18.7	-12.3	-16.4	-3.4
62.5	-5.7	-14.8	-12.1	-4.4
66.4	-7.7	-5.7	-11.8	-4.3
70.3	-10.1	-13.8	-16.3	-3.2
74.2	-3.9	-5.2	-9.4	-4.7
78.1	-10.2	-3.9	-10.5	-4.3
82.0	-8.6	-4.7	-13.4	-5.1

At the 63° grazing angle, the face of the ridge keel is normal to the incident acoustic energy, therefore there will be reflected energy in addition to diffraction, refraction, and re-radiation. Comparing these results with those at 47°, gives the contribution for reflection to BSS as approximately 15 dB.

Figure 6.19 compares the observed BSS for the open lead and the ridge keel at shallow (15°) and moderate (41 to 47°) grazing angles. At shallow grazing angles the ridge keel contributes significantly more (15 dB) to BSS than the open lead. As discussed above, this is due to coincidence of compressional waves along the leading face of the ridge keel. This coincidence does not exist at 15° grazing angle for the smooth plate next to the open lead. At the moderate grazing angle, both the open lead and the ridge keel display comparable BSS. In this case, coincidence of compressional waves is present in both features.

5. Results from the Rubble Field

BSS measurements were made with the rubble field model and compared with actual Arctic BSS measurements. The measured BSS from the model of the rubble field for different grazing angles and frequencies is given in Table VI. In calculating the BSS, the area term in Equation 6-2 was taken to be just the area of the randomly rough surface that was ensonified, that is, the ensonified area of the smooth plate outside the rough area was not included. This differed from the calculations made for the open lead and ridge keel in which the area term included the smooth plate. This is justified since

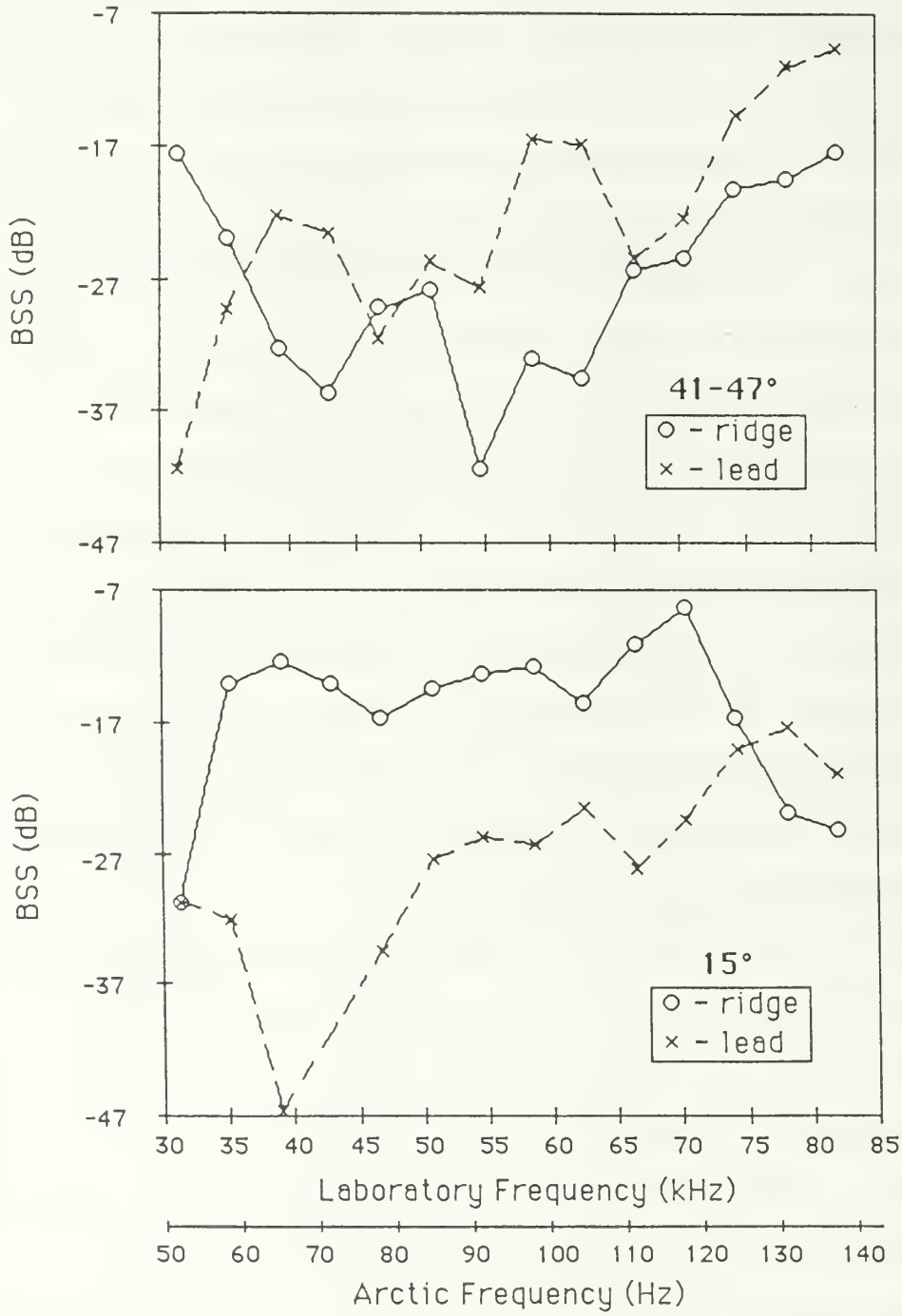

Figure 6.19: Comparison of the measured BSS from the acrylic models of the open lead and ridge keel at shallow and moderate grazing angles.

smooth ice is an integral part of ridges and leads and its effect will be included in actual arctic measurements, whereas backscatter from a large rubble area will not include smooth ice.

The BSS was averaged over the laboratory frequencies of 31 to 82 kHz (52 to 137 Hz scaled to the Arctic) for each grazing angle and plotted in Figure 6.20 along with data from actual Arctic measurements. The shallow grazing angle data are from Milne (1964) for frequencies of 25 to 100 Hz. These data were taken in a region of broken one year pack ice and therefore can be considered as being entirely from rough ice. The other set of data from Brown and Milne (1967) was taken in an area that contained 10 to 15% pressure ridges separated by rough ice. The low BSS at shallow grazing angles under these conditions can be attributed to shadowing by the ridge keels. Overall, these data show the acrylic randomly rough surface to be a good model of an Arctic rubble field for low frequency acoustic backscatter.

6. Composite BSS vs. Arctic Measurements

The composite BSS for the acrylic model was calculated by converting the observed BSS for each feature (open lead, ridge keel, and rubble ice field) to backscattered pressure, weighting these pressures in accordance with the spatial occurrence of the ice features and converting the composite pressures to BSS.

$$BSS_c = 20 \log \sum_{i=1}^{3} \xi_i 10^{BSS_i/20}$$

where BSS_c is the composite BSS, BSS_i is the BSS for the ith

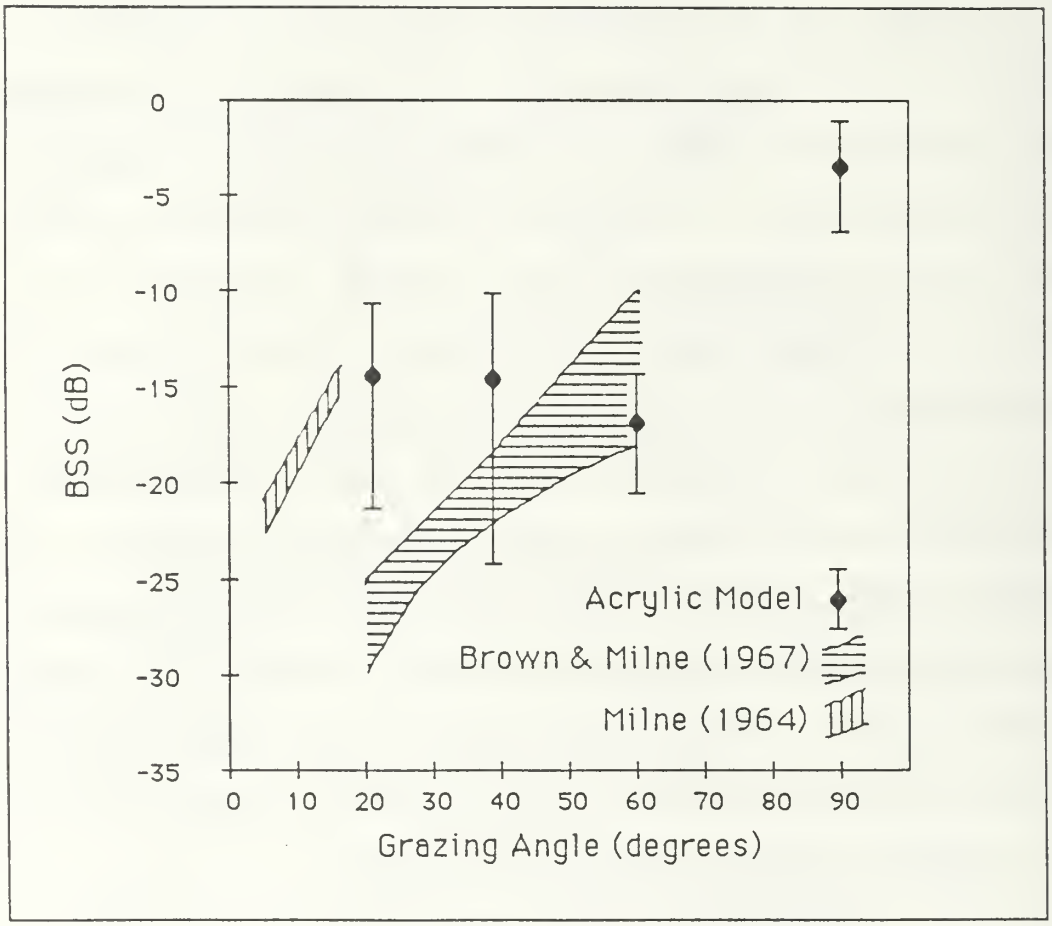

Figure 6.20: Backscattering strength as a function of grazing angle for the acrylic model of a rubble field compared with actual Arctic backscatter from rough ice.

feature, and ξ_i is the spatial weighting factor. The values of ξ used were: 0.05 for open leads, 0.125 for ridge keels, and 0.125 for rubble ice fields. In this analysis, the BSS due to the smooth acrylic plate is taken to be zero.

The composite BSS, scaled to five Arctic frequencies, calculated for a grazing angle of .15° is plotted in Figure 6.21 along with BSS measured in the Arctic (Mellen and DiNapoli, 1986) near 10° grazing angles. The plot shows excellent agreement between backscatter measurements made with the acrylic model and actual measurements made in the Arctic. The solid line included in Figure 6.21 is from a recent computer model for backscattering from the Arctic ice (Green and Stokes, 1985) based on diffractive scattering from small scale roughness on the flanks of randomly oriented triangular ridge keels. This model does not take mode conversion into account, which from the present work appears to be a significant contributor to backscatter from the Arctic ice.

C. SUMMARY

Based on the results of the backscatter measurements and the previous discussion, the following significant results are reported: (1) Mode conversion (predominantly refraction of compressional waves) significantly affects backscatter and can add or detract from backscatter due to rigid boundary diffraction by wedges and edges. (2) Backscatter from ridge keels at low frequencies and shallow grazing angles is more significant than backscatter from

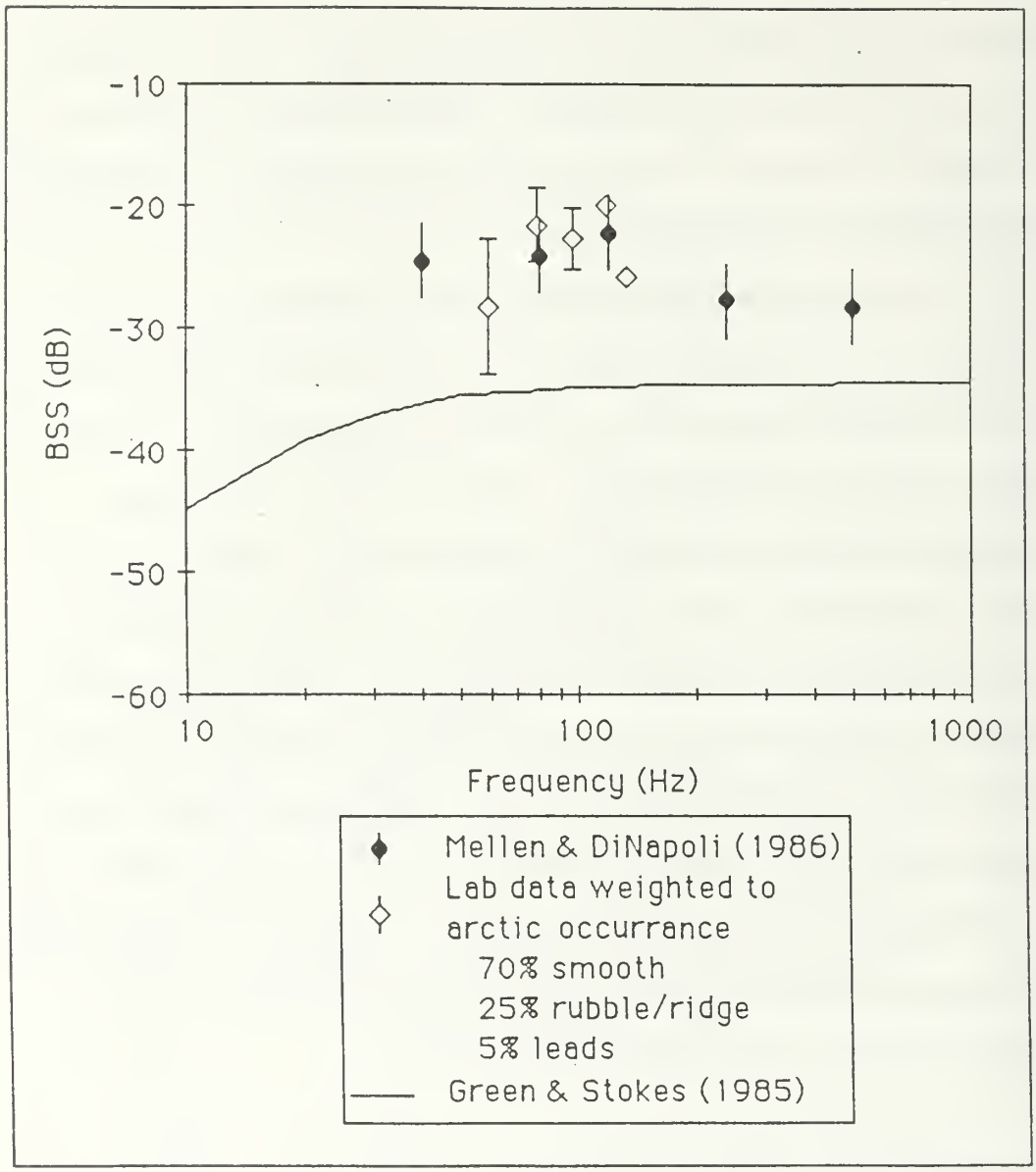

Figure 6.21: Composite BSS computed for the acrylic model of the Arctic ice scaled to arctic frequencies plotted along with Arctic measurements of BSS. Curve is from a computer model of arctic backscatter which does not consider mode conversion.

open leads. The difference is attributed to coincidence between compressional waves in the water and compressional waves in the acrylic model along the relatively steep sloped ridge keel. At moderate grazing angles when coincidence of compressional modes is likely in both models, the observed backscattering results are comparable. (3) Laboratory backscatter data obtained from acrylic models, when weighted to account for statistical occurrence of smooth, ridged, open leads, and rubble ice yields backscattering strengths in good agreement with Arctic measurements.

VII. SMOOTH PLATE FLEXURAL WAVES

The transfer of acoustic energy from the waterborne compressional wave to the ice medium in the form of ice plate flexural waves is studied to determine the significance of the energy loss of the incident waterborne compressional wave and the reradiation of flexural wave energy into the water boundary layer below the ice plate. For these measurements the smooth acrylic plate level ice model was used. The equipment set-up and signal processing was the same as for the previous experiments with the exception of the source and receiver as described below.

A. PROCEDURE FOR THE MEASUREMENT OF THE SMOOTH PLATE FLEXURAL WAVE

1. Measurement of Flexural Wave Speed

The flexural wave speed was measured both with the plate suspended in air and floating in the water tank. In air the plate was laid on top of three 10 cm by 10 cm by 1.5 m wooden beams and measurements were collected in the area between the beams to minimize mass loading effects. For both measurements the plate was driven by an LC-32 transducer at 25 volts. The transducer was held lengthwise in contact with the plate by resting a small bag of lead beads on top of the transducer. The purpose of this was to improve the driver system efficiency and prevent the transducer from just

vibrating without putting energy into the plate. The receiver was an accelerometer. The accelerometer was screwed into a 2.5 cm by 2.5 cm by 1 cm piece of plexiglass. Tackiwax® was used to stick the block of plexiglass to the plate. The signal was pulsed at three cycles per pulse with 100 msec pulse separation. Arrival times at 5 kHz intervals for a frequency range of 20 to 80 kHz were collected for source to receiver separations of 30, 45, and 60 cm. All data were stored on magnetic disk.

2. Measurement of the Boundary Wave

The smooth acrylic plate was floating in water for these measurements. The source was an LC-10 hydrophone positioned in the water below the plate. The receiver was an LC-10 positioned below the plate in the water at a horizontal range of 0.5 m from the source. The source and receiver length axes were parallel to the plate. The receiver was mounted using a 3 mm stainless steel rod to a device that was able to adjust the depth at 1 mm increments. The initial measurement was taken with the source and receiver in contact with the plate from below. Once the flexural wave was identified, then the source and/or receiver were lowered at depth increments until the signal-to-noise ratio was too low for accurate measurements. Data were stored on magnetic disk.

3. Measurement of Flexural Wave Attenuation

These measurements were made with the plate floating in the water tank. The accelerometer could no longer be used as a receiver since the plate-to-receiver efficiency depended

heavily on the bond, and the previous method of using tackiwax for sticking the accelerometer to the plate could not be duplicated from range to range with a measurable precision. Therefore, measurements were made using a Bruel and Kjaer ½ in condenser microphone. This limited the frequency range since microphone frequency response roll-off occurred above 20 kHz. The microphone, suspended from a metal rod spanning the plate, was slid across the plate at a height of 2 mm. Three data runs were conducted, one each at 10, 15 and 20 kHz. For the 10 and 15 kHz data runs five data points, at 10 cm spacing, were collected between 1 - 1.5 m interval spacing. Below 1 m the time of arrival of the airborne sound wave generated by the source (travelling at 350 m/s) interfered with the plate flexural wave (travelling at speeds less that 650 m/s) at frequencies below 15 kHz. At 20 kHz the attenuation was too great for measurements to begin at 1 m; but due to the faster flexural wave speed (750 m/s) at 20 kHz, there was sufficient signal separation to collect data between 0.5 - 1.0 m. Since these measurements were collected in air in a noisy environment it was necessary to collect the data at night when ambient noise conditions were much lower. An HP-3561A Dynamic Signal Analyzer was used to collect and process the data. RMS averaging of 1000 samples points was used to compute the received signal level. Attenuation measurements and analysis were conducted by LT. Michael Browne, USN.

B. FLEXURAL WAVE MEASUREMENT RESULTS

The condition necessary to achieve efficient mode conversion between compressional waves in the water and flexural waves in the plate is to match the horizontal component of the wavenumber in the plate. For both our acrylic plate and for Arctic ice, plate flexural speed is less than water compressional speed at all frequencies, therefore, the condition for efficient mode conversion is never satisfied. We were, however, able to generate flexural waves in the acrylic plate.

1. Results of Flexural Wave Speed Measurements

Once the flexural wave was identified the measurement of its speed was relatively easy. Identification required making several data runs while varying only the frequency and comparing the received pressure amplitude time plots. Due to the dispersive nature of flexural waves the received signal due to the flexural wave would arrive earlier as frequency was increased since flexural speed increased with increased frequency. Figure 7.1 is a plot of the acrylic plate flexural wave group speeds measured with the plate in air and floating on water. As expected, the speeds in water were slower than those in air due to the increased mass loading of the water on the plate. The frequency dependence of the flexural wave speed illustrates that for our frequency range of interest we are operating in the 'low frequency' regime. The flexural wave speeds of the rough surface acrylic plate were not measured but

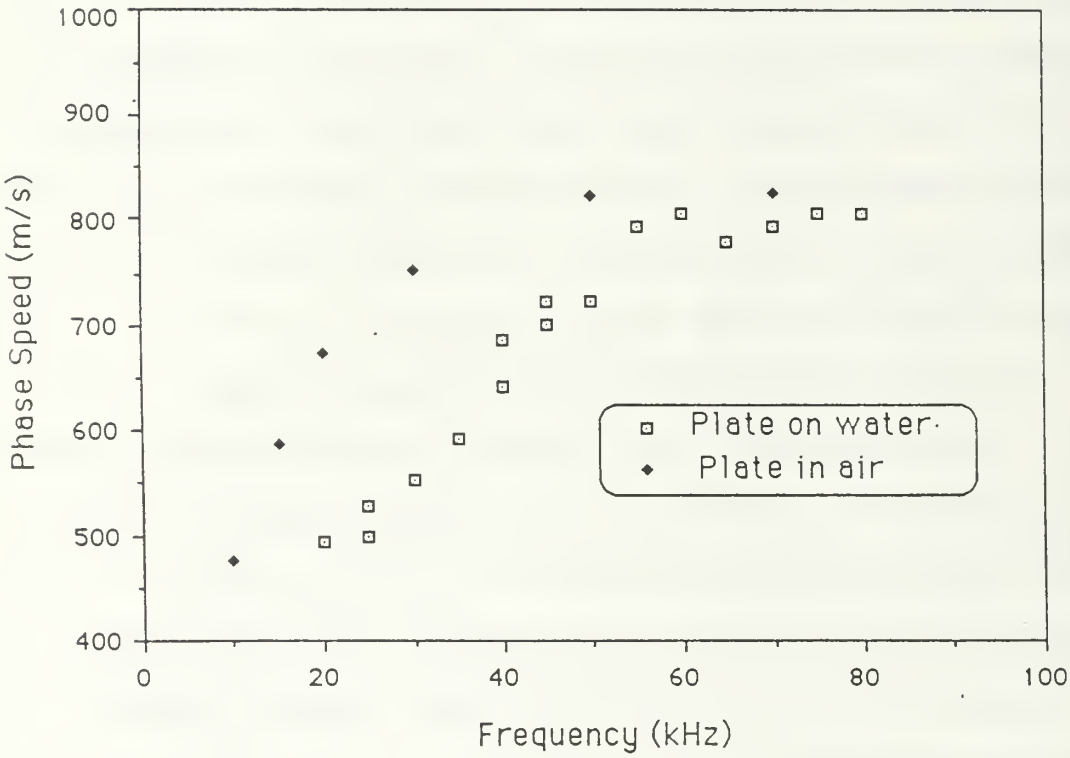

Figure 7.1. Flexural wave phase speed as a function of frequency for a 3 mm thick smooth acrylic plate. Data was collected for the plate in air and floating on water.

speeds slower than those measured for a smooth plate would be expected due again to the effect of mass loading.

Figure 7.2 illustrates clearly that the acrylic plate accurately models arctic ice for the study of flexural wave propagation. The two lines marked 'Ice' are the theoretical flexural wave phase speeds plotted by substituting the reported physical constants of arctic ice listed in Table 3.1 into Equation 4.17, the low frequency approximation, and assuming a 1.5 m ice plate thickness. The solid line marked 'Acrylic' is a similar theoretical plot for an assumed 1.5 m thick acrylic plate. The dots are laboratory measurements of flexural wave phase speed for the 3 mm thick acrylic plate in which the frequencies have been scaled by the appropriate thickness/wavelength ratio.

2. Results of Boundary Wave Measurements

As discussed in Chapter IV, any modes re-radiated into the water from a subsonic flexural wave in a plate will be evanescent, that is, the energy will decay exponentially with distance from the plate instead of propagating as a harmonic wave. Figure 7.3 is a plot of the measured boundary wave pressure relative to the pressure of the direct, spherically diverging waterborne compressional wave plotted as a function of the ratio of the depth of the receiver below the plate to the wavelength of the waterborne compressional wave. The upper dashed line on the plot is the predicted level for the condition of the source in contact with the plate. The lower solid line is for the source at a depth of 6 mm. The circles and dark blocks

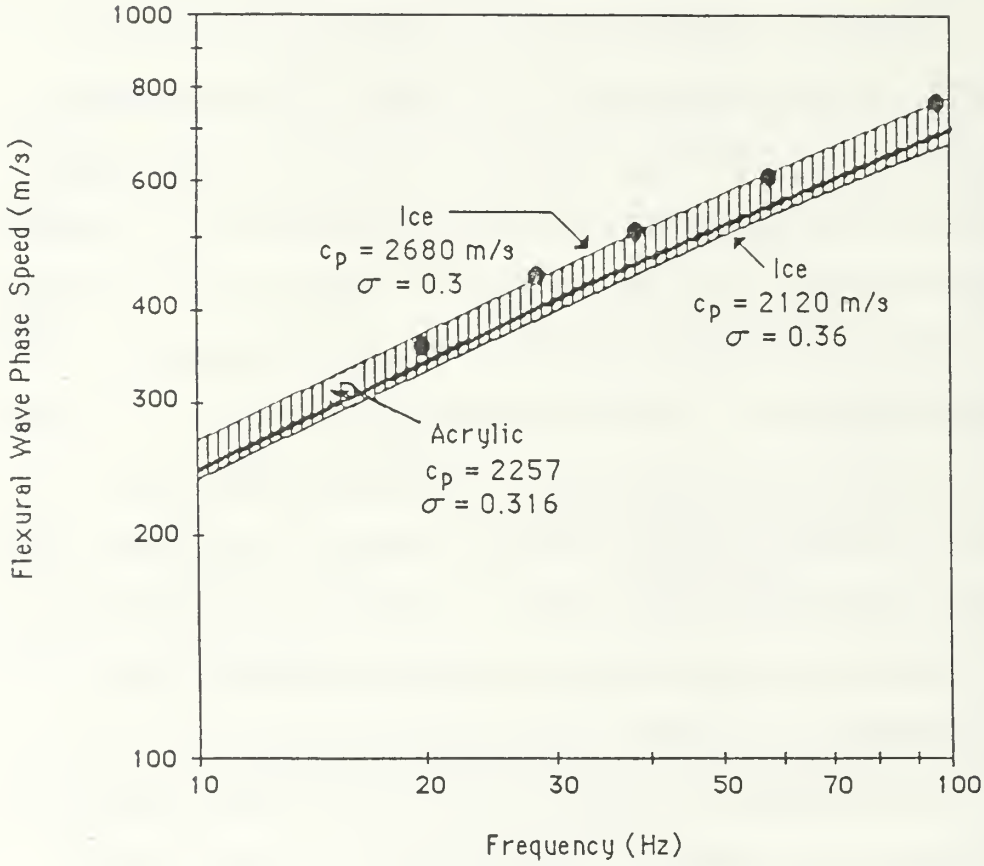

Figure 7.2. Theoretical flexural phase speed for an infinite flat plate of 1.5 m thickness. Ice and acrylic curves are calculated using values listed in Table 3.1. Dark circles are measurements collected on a 3 mm thick acrylic plate and scaled to 1.5 m thickness. The area between the ice curves represents the range of theoretical arctic ice flexural phase speeds. Arctic ice to acrylic frequency and thickness ratio is 1:600.

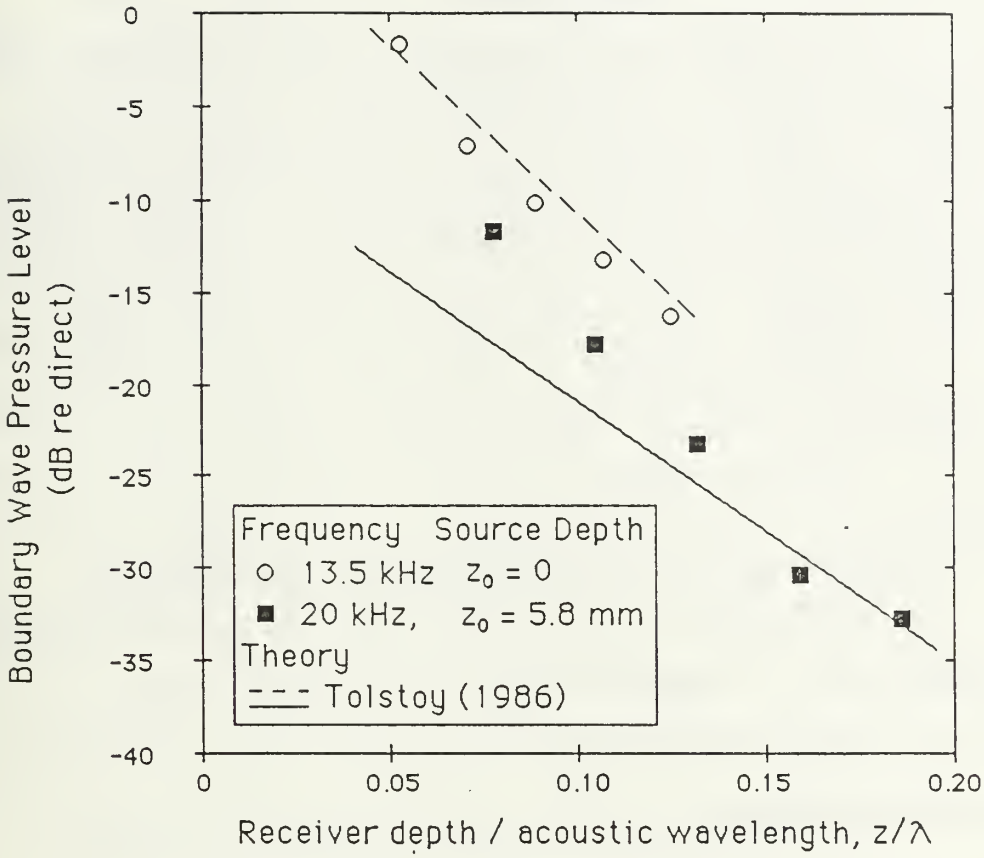

Fig. 7.3. Measured boundary wave pressure relative to the pressure of the direct water wave plotted as a function of the ratio of the depth of the receiver below the plate to the wavelength of the waterborne compressional wave. The upper dashed line is the predicted level for the condition of the source in contact with the plate. The lower solid line is for the source at a depth of 6 mm. The circles and dark blocks are experimental results.

are experimental results. For both cases, the experimental results are in excellent agreement with the Tolstoy (1986) theory. If these results were extended to Arctic conditions, this graph suggests that for a 50 Hz signal from a source 3.5 m below the ice, the strength of the boundary wave at a receiver 6 m beneath the ice and at a horizontal range of 300 m would be down no greater than 35 dB relative to the direct path signal. The term 'no greater' is used because plate flexural wave attenuation in ice is expected to be less than that measured in acrylic, which is the topic of the next section.

3. Results of Acrylic Plate Attenuation Measurements

The attenuation of the flexural wave in the acrylic plate was measured as 1.5 dB/m times the frequency in kHz. A value for Arctic ice flexural wave attenuation was not found in the available literature.

VIII. CONCLUSIONS

The results of these experiments provide insight into what contribution specific physical Arctic ice features make toward the gross underice "reflection coefficient" at low frequencies. It has been demonstrated that acrylic "ice sheets" can acoustically model these ice features in the low frequency regime. This therefore permits one to conduct detailed studies of scattering from the Arctic ice canopy under controlled laboratory conditions. This is a major advantage over field measurements due to the highly variable nature of the ice floes and the difficultly in measuring the profiles of the under side of sea ice.

A summary of the results of these experiments are:

1. For a smooth acrylic plate, the pressure reflection coefficient is approximately 0.95 except near the coincidence frequency, where it may drop to 0.7.

2. For a smooth acrylic plate, an evanescent flexural boundary wave exists, agrees with Tolstoy theory (1986), and is significant.

3. For a pressure ridge keel, low frequency forward scatter losses are nearly independent of frequency, and decrease as grazing angle decreases.

4. For a rubble field, a prediction of coherent specular scatter can be approximated by assuming a Gaussian probability density function (PDF) of ice bottom roughness rather that using the actual pdf of the rough bottom. Losses up to 7 dB per bounce can be expected for large roughness.

5. Mode conversion significantly affects backscatter and can add or detract from backscatter due to diffraction by ridge keels and ice edges.

6. Backscatter from ridge keels at low frequencies and shallow grazing angles is more significant than backscatter from open leads.

7. Backscatter from the acrylic rubble field is in excellent agreement with scaled Arctic measurements from rough ice at shallow and moderate grazing angles.

8. Laboratory backscatter data obtained from the acrylic models, when weighted to account for statistical occurrence of smooth, ridged, and rubble ice, and the presence of open leads yields backscattering strengths in good agreement with overall Arctic measurements of backscatter.

LIST OF REFERENCES

Ackley, S. F., Cold Regions Research and Engineering Laboratory Report 76-18, *Thickness And Roughness Variations Of Arctic Multiyear Sea Ice*, Table II, p. 9, June 1976.

Biot, M. A. and Tolstoy, I., "Formulation Of Wave Propagation In Infinite Media By Normal Coordinates With An Application To Diffraction", *J. Acoust. Soc. Am.*, **29**, 381-391, 1957.

Bourke, R. H., Dept. of Oceanography, Naval Postgraduate School, Monterey, California (personal communication).

Brigham, E. O., *The Fast Fourier Transform*, Prentice-Hall, Inc., Englewood Cliffs, New Jersey, 1974.

Brown, J. R. and Milne, A. R., "Reverberation Under Arctic Sea-Ice", *J. Acoust. Soc. Am.*, **42**, 78-82, 1967.

Clay, C. S. and Medwin, H., *Acoustical Oceanography: Principles And Applications*, John Wiley & Sons, Inc., New York, New York, 1977.

Diachok, O. I., Naval Oceanographic Office Technical Note No. 6130-4-74, *Effects of Sea Ice Ridge Characteristics on Under-Ice Reflection Loss in Arctic/Subarctic Waters,* p. 11, August 1974.

Eckart, C., "The Scattering Of Sound From The Sea Surface", *J. Acoust. Soc. Am.*, **25**, 566-570, 1953.

Green, R. R. and Stokes, A. P., "A Model Of Acoustic Backscatter From Arctic Sea Ice", *J. Acoust. Soc. Am.*, **78**, 1699-1701, 1985.

Hibler, W. D. III, and Ackley, S. F., "A Sea Ice Terrain Model And Its Application To Surface Vehicle Trafficability", *J. Terramechanics*, **12**, 171-190, 1975.

Hibler, W. D. III, Mock, S. J. and Tucker, W. B. III, "Classification And Variation Of Sea Ice Ridging In The Western Arctic Basin", *J. Geophys. Res.*, **79**, 2735-2743, 1974.

Hibler, W. D. III, Weeks, W. F. and Mock, S. J., "Statistical Aspects Of Sea-Ice Ridge Distributions", *J. Geophys. Res.*, **77**, 5954-5970, 1972.

Hunkins, K., "Seismic Studies Of Sea Ice", *J. Geophys. Res.*, **65**, 3459-3472, 1960.

Kasputis, S. R. and Hill, P. D., *Measurement Of Mode Interaction Due To Waveguide Surface Roughness*, M.S. Thesis, Naval Postgraduate School, Monterey, California, December 1984.

Kinsler, L. E., Frey, A. R., Coppens, A. B., and Sanders, J.V., *Fundamentals Of Acoustics*, 3d ed., John Wiley & Sons, Inc., 1982.

Kovacs, A., Weeks, W. F., Ackley, S. and Hibler, W.D., "Structure Of A Multi-Year Pressure Ridge", *ARCTIC*, **26**, 22-31, 1973.

McCammon, D. F. and McDaniel, S. T., "The Influence Of The Physical Properties Of Ice On Reflectivity", *J. Acoust. Soc. Am.*, **77**, 499-507, 1985.

Medwin, H., "Shadowing By Finite Noise Barriers", *J. Acoust. Soc. Am.*, **69**, 1060-1064, 1981.

Medwin, H., Childs, E. and Jebsen, G. M., "Impulse Studies Of Double Diffraction: A Discrete Huygens Interpretation", *J. Acoust. Soc. Am.*, **72**, 1005-1013, 1982.

Medwin, H. and Novarini, J. C., "Backscattering Strength And The Range Dependence Of Sound Scattered From The Ocean Surface", *J. Acoust. Soc. Am.*, **69**, 108-111, 1981.

Medwin, H. et al, "Sound Scatter And Shadowing At A Seamount: Hybrid Physical Solutions In Two And Three Dimensions", *J. Acoust. Soc. Am.*, **75**, 1478-1490, 1984.

Mellen, R. H. and DiNapoli, F. R., *Acoustic Scattering In The Arctic Ocean*, paper presented at the Naval Symposium on Underwater Acoustics, 36th, San Diego, California, 3 April 1986.

Myers, J. J., Holme, C. H., and McAllister, R. F., eds., Handbook Of Ocean And Underwater Engineering, pp. 1-8, McGraw-Hill Book Co., 1969.

Milne, A. R., "Underwater Backscattering Strengths of Arctic Pack Ice", *J. Acoust. Soc. Am.*, **36**, 1551-1556, 1964.

Novarini, J.C. and Medwin, H., "Computer Modeling Of Resonant Sound Scattering From A Periodic Assemblage Of Wedges: Comparision With Theories Of Diffraction Gratings", *J. Acoust. Soc. Am.*, 77, 1754-1759, 1985.

Ross, D., *Mechanis Of Underwater Noise*, Pergamon Press, New York, New York, 1976.

Tolstoy, I., "Effect Of Roughness On Subsonic Flexural Waves In A Thin Plate Overlying A Compressible Fluid", *J. Acoust. Soc. Am.*, **79**, 666-672, 1986.

Urick, R. J., *Principles Of Underwater Sound*, 3d ed., McGraw-Hill Book Co., New York, New York, 1983.

Wadhams, P. and Horne, R. J., "An Analysis Of Ice Profiles Obtained By Submarine Sonar In The Beaufort Sea", *J. Glaciology*, **25**, 401-424, 1980.

Wadhams, P., McLaren, A.S. and Weintraub, R., "Ice Thickness Distribution In Davis Strait In February From Submarine Sonar Profiles", *J. Geophys. Res.*, **90**, 1069-1077, 1985.

Weeks, W. F., Kovacs, A. and Hibler, W. D. III, "Pressure Ridge Characteristics In The Arctic Coastal Environment", *Proceedings from the First International Conference on Port and Ocean Engineering under Arctic Conditions*, **I**, 152-183, 1971.

Wright, B. D., Knatiuk, J. and Kovacs, A., *Sea ice pressure ridges in the Beaufort Sea*, United States Army Cold Regions Research and Engineering Laboratory, Hanover, N. H., Report # MP-1132, 19 p., 1978.

INITIAL DISTRIBUTION LIST

		No. Copies
1.	Defense Technical Information Center Cameron Station Alexandria, Virginia 22304-6145	2
2.	Library, Code 0142 Naval Postgraduate School Monterey, California 93943-5002	2
3.	Professor H. Medwin, Code 61Md Department of Physics Naval Postgraduate School Monterey, California 93943	5
4.	Dr. R. Fitzgerald Code 4250A Office of Naval Research 800 N. Quincy Arlington, Virginia 22217	1
5.	Lcdr. Patrick L. Denny 1109 Five Point Road Virginia Beach, Virginia 23454	2
6.	Lt. Kevin R. Johnson Submarine Officer Advanced Course Code 7851 800 Box 700 Groton, Connecticutt 06349-5700	2

TITLE NUMBER _____ CUSTOMER NUMBER _____

LIBRARY: Dudley Knox Library, Naval Postgraduate School
~~Monterey, CA 93943~~

ROSWELL BOOKBINDING
LIBRARY DIVISION
2614 NORTH 29th AVENUE
PHOENIX, ARIZONA 85009
PHONE (602) 272-9338

Binding in Everything ☐

	F	B	NP
CONTENTS			
INDEX			
Bind without Index			

ISSUE CONTENTS

Discard	☐
Bind in Place	☐
Gather at Front	☐

	IN	OUT
Advertisements		
Front Covers		
Back Covers		
1st only		
Accents		
Imprints		

Special Instructions

PATRICK LEO DENNY

~~D365~~

Thesis D365

Buck Color	598
Print Color	~~Gold~~
Trim Height	
Ht. Inches	
Over Thick	
For Title	
Extra Lines	
Extra Coll.	
Hand Sew	
Slit	
Rules	
1st Slot No	
Vol. Slot No	
Year Slot No	
Call # Slot	
Imp Slot No	
Type Face	
Price	
Mending	
Map Pockets	
2 Vols in 1	

ACTUAL TRIM	DATE
SPINE	JOB
BOARD DIM	LOT
CLOTH DIM	ROUTE
CLOTH BIN	SEQ NO

17603/7

thesD365
Underwater acoustic scatter from a model
3 2768 000 75858 5
DUDLEY KNOX LIBRARY